Novel Concepts for RF Surface Coils with Integrated Receivers

by

Sonam Tobgay

A Thesis
Submitted to the Faculty
of the

WORCESTER POLYTECHNIC INSTITUTE

in partial fulfillment of the requirements for the
Degree of Master of Science
in

Electrical Engineering

by

_____

April 2004

Approved:

_____   _____

Professor Reinhold Ludwig   Professor William Michalson
Thesis Advisor   Thesis Committee
ECE Department   ECE Department

_____   _____

Dr. Gene Bogdanov   Professor Fred Looft
Thesis Committee   Department Head
ECE Department   ECE Department

Novel Concepts for RF Surface Coils with Integrated Receivers

by

Sonam Tobgay

A Thesis
Submitted to the Faculty
of the

WORCESTER POLYTECHNIC INSTITUTE

in partial fulfillment of the requirements for the
Degree of Master of Science
in

Electrical Engineering

by

_____
April 2004

Approved:

_____
Professor Reinhold Ludwig
Thesis Advisor
ECE Department

_____
Professor William Michalson
Thesis Committee
ECE Department

_____
Dr. Gene Bogdanov
Thesis Committee
ECE Department

_____
Professor Fred Looft
Department Head
ECE Department

Abstract

Magnetic Resonance Imaging (MRI) is a powerful non-invasive reconstruction tool used primarily in the medical community to produce high quality images of the human anatomy. Surface coils are Radio Frequency (RF) systems typically deployed for receiving the MR signals. Multiple surface coils, or an array of coils, are employed to obtain a localized improvement in the signal-to-noise ratio without limiting the field of view.

In this research, a novel modeling and design method for decoupling RF surface coils in a phased array is investigated. This method employs an impedance transformation interface circuit along with a high input reflection coefficient preamplifier to decouple the coil. In this research report both the theory and design methodology are discussed in detail.

Acknowledgments

I would like to express my sincere appreciation to my advisor Professor Reinhold Ludwig. I would not have been able to complete this thesis without his guidance, encouragement and patience.

I am grateful to Dr. Gene Bogdanov and Professor William Michalson. Their advice, insights and inputs were extremely valuable throughout the project. I would also like to thank them for serving on my thesis committee.

Many thanks to my fellow students, Souheil Benzerrouk, Tim Fisher, Rostislav Lemdiasov, and Aghogho Obi in the RF laboratory for all their support and also for making it a wonderful work place.

Special thanks to Mark Sipos, Rebecca Killigrew, Richard Cheng, and others at Tepin Information LLC for their support when I started my M.Sc. program.

I would also like to thank Mr. and Mrs. Schwartz and family for the kindness they showed toward me for all these years.

Words cannot express my gratitude to Madelyn B. Connolly and my family for their kindness, support and encouragement throughout my M.Sc. program.

Table of Contents

1 Introduction

1.1 *Problem Statement*

Radio Frequency (RF) coils are key components of a Magnetic Resonance Imaging (MRI) system and are used to transmit and receive high frequency electric signals needed to construct an image of the biological entity. They are categorized into volume coils and surface coils. Volume coils have excellent radial field homogeneity and are used to produce a uniform magnetic field in the region of interest. Surface coils can be either single or multiple loop coils. They need to have good signal-to-noise ratio and are primarily used as receive coils. However, surface coils cover a small area that results in a small field of view. Therefore, in an effort to enhance the field of view multiple surface coils, or an array of coils, are employed to obtain a localized improvement in the signal-to-noise ratio (SNR). Unfortunately, these phased array coils have the disadvantage of noise coupling between the coil elements. This research attempts to address this problem by proposing a new coil interface and a novel preamplifier unit that enables decoupling.

1.2 Objective

The objective of this research is to examine a novel modeling and design methodology employed for decoupling RF surface coils in a phased array configuration. The intent is to utilize this method and develop a RF coil interface and a preamplifier unit that can be used to decouple multiple coils in a phased array. Our approach is to research and design circuit schematics for both the coil and the preamplifier, followed by the simulation and performance analyses of the designs. Finally, to demonstrate the feasibility of the developed design approach, several coils and amplifiers were constructed.

1.3 Thesis Outline

This thesis is organized as follows: Chapter 2 presents the basic concepts of Magnetic Resonance Imaging (MRI). An introductory overview of SNR in MRI is briefly discussed in Chapter 3, while Chapter 4 develops the concepts and principles of microwave and RF theory needed to design the circuits. Chapter 5 presents details of the interface circuit design and its underlying theory. Chapter 6 describes the steps carried out for coil fabrication and testing. The developmental procedure for the preamplifier is discussed in Chapter 7. Finally, conclusions of this research are drawn in Chapter 8.

2 NMR Basic Principles

Introduction

Magnetic Resonance Imaging (MRI) is a powerful non-invasive tool used primarily in the medical community to produce high quality images of the human anatomy. It has gained this reputation because of its flexibility and sensitivity to a broad range of tissue properties [1]. Since it does not require the exposure of the subject to ionizing radiation, it is generally regarded as safer than other imaging techniques such as X-ray computed tomography (CT). The applications of MRI continue to expand rapidly and advancements made in imaging techniques and acquisition speeds continue to further enhance and improve MRI.

2.1 Nuclear Magnetic Resonance

MRI is based on the principles of nuclear magnetic resonance phenomena. Nuclear Magnetic Resonance (NMR) is related to nuclear spin; this occurs when the nuclei of certain atoms are immersed in a static magnetic field and exposed to a second oscillating magnetic field. The principle of NMR is based on the quantum mechanical interaction between the atomic nuclei and the magnetic field [1]. However, NMR phenomena can also be explained in the context of classical physics, as discussed below.

2.1.1 Spin

Spin just like charge and mass is a fundamental property of nature. Protons, electrons, and neutrons possess this property in atomic nuclei. The dominant nucleus in MRI is the proton in hydrogen, and for this reason one may look primarily at the characteristics and the interaction of a proton.

Classical theory views a proton as a small sphere of distributed positive charge. A proton has mass and it rotates about its axis (see Figure 1) due to spin. This rotation generates an angular momentum, which in turn generates current due to the motion of a net charge. As a result, the loop current produces a small magnetic field.
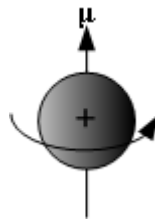
Figure 1. The charge of a spinning proton generates a nuclear magnetic moment $\boldsymbol{\mu}$.

The relationship between angular momentum, $\mathbf{J}$, and the magnetic moment, $\boldsymbol{\mu}$, is given by [1]

$$\boldsymbol{\mu} = \gamma \mathbf{J} \tag{1}$$

where γ is the gyromagnetic ratio. The hydrogen proton of water has a γ of $267.5\,\mathrm{MHz/T}$ [5].

If one considers a nucleus consisting of two protons as an isolated system, the angular momentum of each proton assume opposite spin states to avoid creating degeneracy, as stated by the Pauli exclusion principle. Thus, only nuclei with an odd number of

protons or neutrons produce angular momentum, and as such are said to possess a net nuclear spin.

2.1.2 Effect of Magnetic Field

Nuclei with nuclear spin assume a state of higher energy level or a state of lower energy level when placed in a static magnetic field. The energy difference, ΔE, between these two states is linearly proportional to the strength of the magnetic field. This is known as the Zeeman effect. Under the condition of thermal equilibrium, the number of nuclei in the higher energy state is fewer than the number of nuclei in the lower energy state. A photon with energy equal to the energy difference of the two states is emitted by a nucleus, when it falls from a higher energy state to a lower energy state, or is absorbed by a nucleus when it jumps from a lower energy state to the higher energy state. A typical energy state diagram is shown in Figure 2.
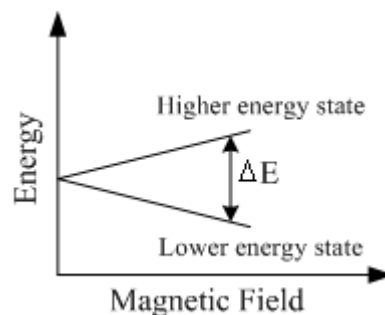
Figure 2. Splitting of energy level.

2.1.3 Magnetization

When an external uniform magnetic field, $\mathbf{B_0}$, is applied, individual magnetic moments align themselves with the external magnetic field. When the magnetic moment aligns with the magnetic field, it is known as a parallel state or it is known as an anti-parallel state if it aligns against the magnetic field. A lower energy level is associated with the parallel state.

If an electromagnetic pulse is applied, the nucleus becomes excited and its rotational axis is tilted away from the axis of the uniform magnetic field B_0 and starts precessing. This frequency of precession is known as the Larmor Frequency.
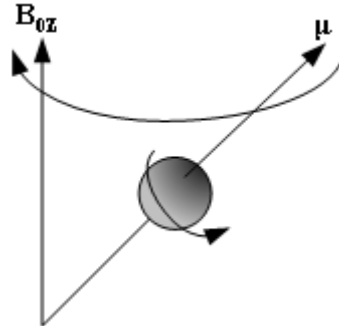
Figure 3. A proton precessing about the axis of a static magnetic field.

The nuclei in a sample material in zero magnetic field are randomly oriented and have zero net magnetic moment. Once a magnetic field is applied, each individual magnetic moment aligns itself with the external magnetic field. Individual nuclei start to precess and align with the applied magnetic field, B_{0Z} as shown in Figure 3. This produces magnetization in the direction of B_0. An increase in B_0 strength increases the positively inclined nuclei, an indication that a stronger signal is measurable in a system with higher B_0 field.

The excited nuclei eventually stop their precession around the B_0 field: they lose their orientation and return to an equilibrium state. This is known as relaxation. There are two types of relaxation, T_1 and T_2.

T_1 is the relaxation time at which the longitudinal magnetization, M_Z, returns to its equilibrium state, M_{0Z} (shown in Figure 4). T_1 relaxation is caused by the nuclei flipping randomly between the parallel and the anti-parallel states. It is different for different materials.
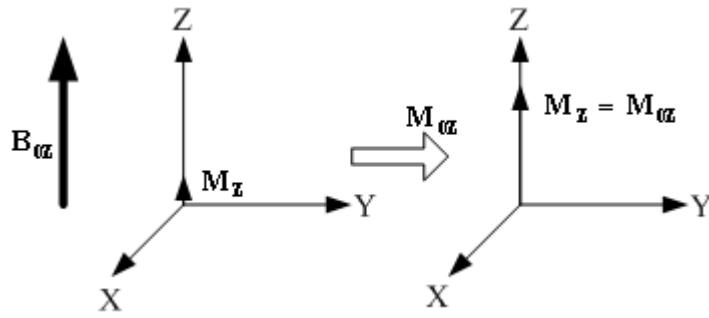
Figure 4. T_1 relaxation.

The T_2 relaxation time is shown in Figure 5 and it is the time at which the transverse magnetization, $\mathbf{M}_{XY}$, decays to zero due to the nuclei loosing synchronization in their precession.
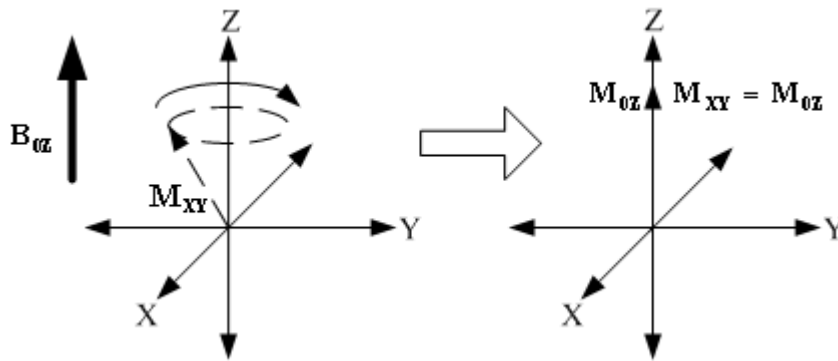
Figure 5. T_2 relaxation.

Transverse relaxation is caused by several biological factors. Non-uniformity of the magnetic field, $\mathbf{B_0}$, also causes transverse relaxation, since the nuclei in different regions of the magnetic field precess at different rates. The combination of these two factors is what actually results in the decay of transverse magnetization. The combined relaxation time is termed T^*_2.

Relaxation time, proton density and other factors all affect the image intensity of an MRI system. There are many methods of obtaining an MRI image and a detailed discussion is beyond the scope of this research. However, the basic principle is a RF signal (current) that is induced in a receiver that is perpendicular to the axis of the transverse magnetization rotation, see Figure 6. This signal from the coil is in

conjunction with spatial gradient fields processed in an imaging system and ultimately transformed into an image.
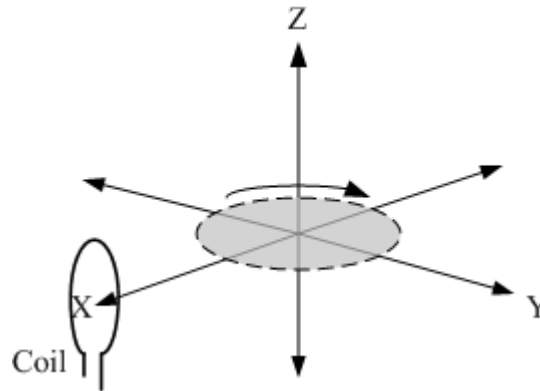
Figure 6. Signal induced on coil by transverse magnetization.

2.2 Magnetic Resonance Imaging Hardware

A MRI system consists of several components that perform different functions. Figure 7 is a generic illustration of an MRI system.

Figure 7. Block diagram of an MRI system [1].

The individual blocks and functional units are explained in more detail below.

2.2.1 Main Magnet

The main magnet is needed to generate a strong magnetic field, B_0, that is uniform over the volume of interest. It is always desirable to have a strong magnetic field since it provides better SNR and better resolution in both frequency and spatial domains. When magnets are 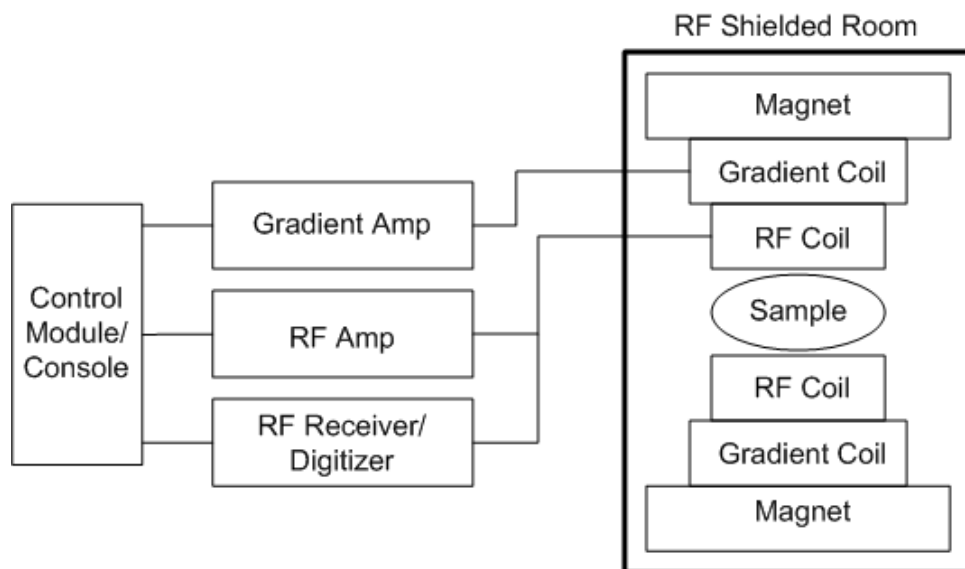unable to provide the desired B_0 field uniformity for high-resolution spectroscopy, shim coils are employed to improve the field uniformity. Clinical imaging systems typically have field strengths no stronger than 3T. However, some experimental systems reportedly have 4T or 7T main magnets.

2.2.2 The Gradient Coils

The gradient coils are used to encode spatially the positions of the nuclear spins in the MRI system by varying the value of the local magnetic field causing precessional frequencies to vary as a function of their positions [1]. A gradient coil set is made up of 3 coils that produce the x, y and z-gradients. The field produced by the gradient coil is required to be linear over the imaging volume. Gradient coils are turned on and off rapidly for imaging applications. Some desirable performance criteria for gradient coils are: low inductance, high current to gradient ratio, minimal resistance, and good gradient field uniformity.

2.2.3 The RF Transmit and RF Receive Coils

The RF coils in MRI that excite the magnetization are referred to as transmit coils. Separate receiver coils receive the signals from the relaxing nuclei spins. A single coil can be used to transmit and receive signals, but separate coils are often employed to improve the SNR. The use of separate coils depends on properties that are desirable for each mode of operation. Transmit coils are required to produce a uniform B_1 field over the region of interest, while receive coils are required to insure

uniformity of the received signal over the volume being imaged. The design of receiver coils is the subject of this thesis.

3 Signal to Noise Ratio

3.1 Signal-to-Noise Ratio

This chapter derives general expressions for the SNR of the surface coil. This will enable us to obtain both an analytical and an intuitive understanding of the performance of a surface coil.

In an MRI system, the changing magnetic field induces a current in the coil whose output signal is amplified, processed, and ultimately displayed as an image. The signal is always corrupted by noise caused by the random fluctuating currents in the surface coil and the object being imaged [5]. The quality of the image depends on the SNR of the signal received by the surface coil. Unfortunately, SNR in MRI depends on a number of factors including the strength of the static magnetic field, the type and characteristics of the RF coils, and imaging parameters such as image resolution and bandwidth [2]. Figure 8 shows a generic voxel emitting an electromagnetic field that induces a current in a coil. A voxel is an abbreviation for volume element, a three dimensional rectangular section of the biological sample being imaged.
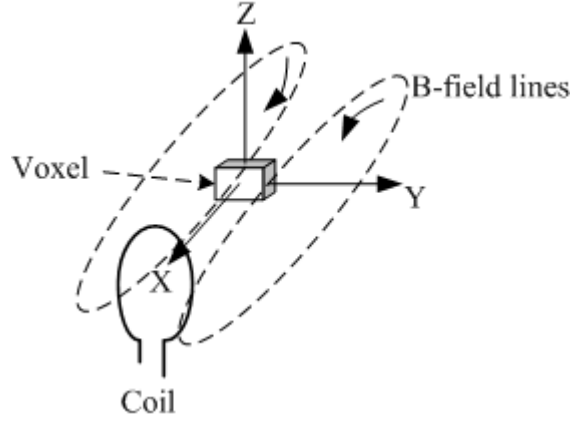
Figure 8. Changing magnetic field emanating from an individual voxel, inducing a current in a receiver coil.

The SNR is generically defined as

$$SNR = 10 \cdot \log\left(\frac{P_{av}}{P_n}\right) \tag{2}$$

where P_{av} is the average power generated by the coil, and P_n is the noise power generated by the coil. The time-averaged power P_{av} is defined as

$$P_{av} = \xi^2 / 8R_L \tag{3}$$

where ξ is the emf and R_L is the coil resistance.

3.2 The SNR of a Single Coil

In a single coil, the noise produced is generally dominated by thermal noise, P_{th}, which can be defined as

$$P_{th} = kTB_W \tag{4}$$

Here the parameters are as follows:

$k = 1.380 \times 10^{-23} \, JK^{-1}$: Boltzmann's constant,

T : temperature in Kelvin, and

B_W : bandwidth in Hz of the receiver.

16

Using equations (3) and (4) in equation (2), we obtain the following general expression for the SNR in a single coil

$$SNR = 10 \cdot \log\left(\frac{\xi^2}{8R_L kTB_W}\right) \qquad (5)$$

This will be the basis for the subsequent SNR computations.

3.3 *Single Coil SNR Example*

To become more familiar with the concept of SNR, let us consider an example and solve for the SNR of a coil with a 1 cm diameter loop. To calculate P_{av} we are first required to find the emf induced by the coil. Specifically, the emf > of a coil produced by a magnetization vector, **M₀**, at an angular frequency T_0 from a voxel of volume V with a magnetic field **B₁** is given by [14]:

$$\xi = \omega_0 B_1 M_0 V \qquad (6)$$

The magnitude of the magnetic field **B₁** for a circular loop along its axis [39] is given as:

$$B_1 = \frac{\mu_0 I a^2}{2\left(a^2 + d^2\right)^{3/2}} \qquad (7)$$

Here, a is the radius of the coil, $\cdot_0$ is the absolute permeability, and d is the distance from the coil to the voxel.

The magnitude of the magnetization vector **M₀** is given by:

$$M_0 = \frac{Nf_0^2 h^2 I(I+1)}{3kTB} \qquad (8)$$

where: f_0: Larmor frequency,

                        I: nuclear spin,

                        $h = 6.626 \times 10^{-34}\, Js$: Planck's constant,

$$N = 10^3 \eta : \text{number of spins per unit volume, and}$$

$$\eta = 6.023 \times 10^{23} \, mol^{-1} : \text{Avogadro's number}$$

Since water makes up about 90% of all biological tissues, let us consider a kilogram of water at 300°K for this example. Consequently, the magnetization is:

$$M_0 = \frac{2 \times \left(\dfrac{10^6 \dfrac{gm}{m^3}}{18\dfrac{gm}{mol}}\right) \times 6.023 \times 10^{23} \, mol^{-1} \times \left(200 \times 10^6 \, Hz\right)^2 \times \left(6.626 \times 10^{-34} \, Js\right)^2 \times \dfrac{1}{2}\left(\dfrac{1}{2}+1\right)}{3 \times 1.380 \times 10^{-23} \dfrac{J}{K} \times 300° \, K \times 4.7T} \tag{9}$$

$$= 7.5 \times 10^3 \frac{A}{m}$$

The magnetic field for a single loop coil with a 1cm diameter in the xy plane is:

$$B_1 = \frac{4\pi \times 10^{-7} \dfrac{H}{m} \times 1A}{0.01m} = 12.566 \times 10^{-3} T \tag{10}$$

Therefore, the emf induced in the coil from a voxel of volume $V = 0.25m^3$ is:

$$\xi = 2\pi \times 200 \times 10^6 \frac{rads}{s} \times 1.2566 \times 10^{-4} T \times 0.0075 \frac{A}{m} \times \left(0.25 \times 10^{-3} m\right)^3 \tag{11}$$

$$= 18.628 \, nV$$

The average power generated by the coil of 1Σ resistance is therefore:

$$P_{av} = 10 \cdot \log \frac{\left(18.628 \times 10^{-9} V\right)^2}{2 \times 1\Omega \times 1000} \approx -187 \, dBm \tag{12}$$

Finally, the noise generated by the coil for a 100KHz bandwidth is

$$P_{th} = 10 \cdot \log \left(\frac{1.380 \times 10^{-23} \, JK^{-1} \times 300° \, K \times 100 \times 10^3/256}{1000}\right) \tag{13}$$

$$\approx -207 \, dBm$$

As a result, the SNR is:

$$SNR = -187dBm + 207dBm \approx 20\,dB \tag{14}$$

The SNR result in equation (14) gives us a rough estimate of the SNR of a simple surface coil in an MRI system. It would be incorrect to attach a precise meaning and state that this is a general applicable result since the SNR of MRI systems typically depends on the experiment that is being conducted.

3.4 The SNR of an Array of Coils

If we have an array of coils (shown in Figure 9) individual coils in the array, in addition to the internal thermal noise, also experience noise from neighboring coils due to coupling. Coupling in this context is the transfer of signal from one coil to another as a result of mutual inductance between the coils. Therefore, the noise produced by a coil in an array configuration is the sum of the thermal noise and the noise that is coupled from the neighboring coils.
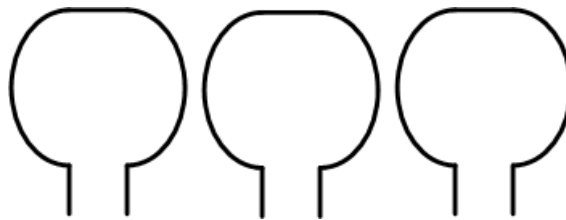
Figure 9. A linear array of three coils.

To understand coupling noise in an array of coils, let us consider the circuit depicted in Figure 10. The figure represents two coils modeled by their inductance, capacitance, and resistance. Capacitor C_C cancels the coil inductance during resonance. Resonance in general terms is a condition in which inductive and capacitive reactances cancel each other. The result is a real impedance. For the rest of this section we will assume that

19

resonance exists (more about the surface coil models and resonance will be discussed in the later chapters).
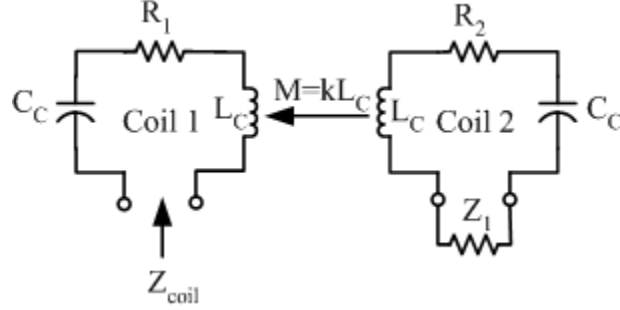
Figure 10. Inductive coupling between coils.

If we view Coil 1 in Figure 10, the impedance Z_{coil} under resonance is equal to R_1 if Coil 2 does not exist. This is because in a single coil the inductance L_C and the capacitance C_C cancel each other under the condition of resonance. Therefore, Z_{coil} is equal to R_1. When we consider the coupling effect of Coil 2 on Coil 1, Z_{coil} is equal to [41]:

$$Z_{coil} = R_1 + \frac{\omega^2 L_C^2 k^2}{R_2 + Z_1} \tag{15}$$

where k is the mutual inductive coupling constant and Z_1 is the impedance seen by Coil 2. The SNR for Coil 1 with noise coupled from Coil 2 is:

$$SNR = \frac{1}{8} \frac{\xi^2}{Z_{coil} kTB_W}$$

$$= \frac{1}{8} \frac{\xi^2}{R_1 kTB_W + kTB_W \left(\dfrac{\omega^2 L_C^2 k^2}{R_2 + Z_1} \right)} \tag{16}$$

The second term in the denominator of equation (16), represents the noise power coupled between the coils. This term approaches zero if Z_1 (the impedance seen by Coil 2) is made very large. When this happens, the SNR of the two coils approaches the SNR of a single coil.

20

In terms of the current in the coil, an increase in Z_1 causes a decrease of current in Coil 2, therefore reducing its coupling effect on Coil 1 and in turn enhancing the performance of the later. However, it is important to note that reducing the current in Coil 2 does not improve its own performance: in this case it is desirable to reduce the current in Coil 1, since this would decrease the coupling effect of Coil 1 on Coil 2.

Using equation (16) as a reference, let us plot P_{av}, P_{th} and the coupled noise power P_{cp} as a function of Z_1 to graphically display how Z_1 affects the coupling between the coils. Based on the estimated parameters $L_C = 10nH$, resistances $R_1 = R_2 = 1\Sigma$, $B_w = 100KHz$ and an emf equal to $18.628 \times 10^{-9} V$ (calculated in equation (11)), we obtain $P_{av} = -194dBm$ and $P_{th} = -208dBm$. P_{cp} is defined as:

$$P_{cp} = kTB_W \left(\frac{\omega^2 L_C^2 k^2}{R_2 + Z_1} \right) \qquad (17)$$
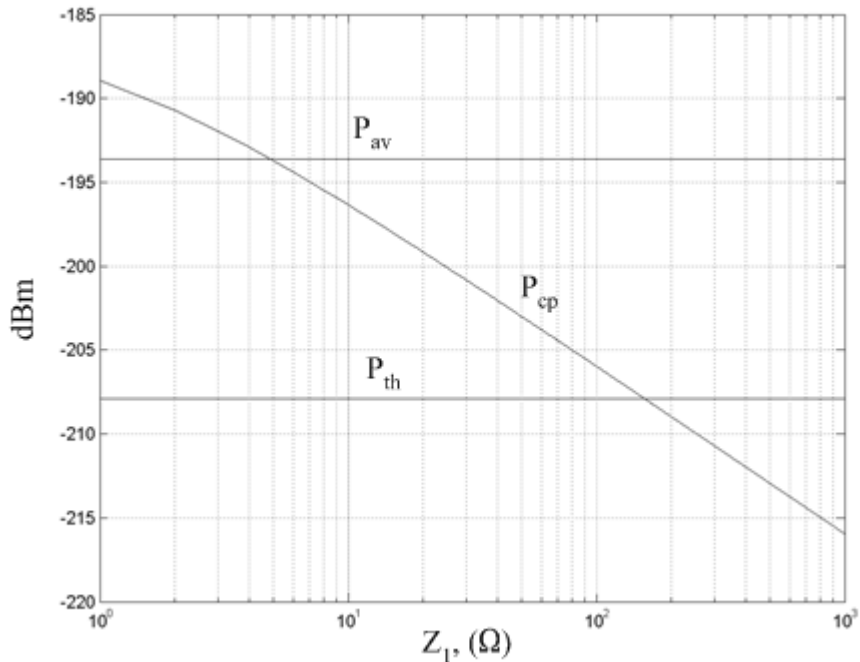
Figure 11. P_{av}, P_{th} and coupling noise power as a function of Z_1.

21

In Figure 11 we can see that P_{av} and P_{th} are constant since they do not depend on Z_1. However, we can observe how the P_{cp} decreases as Z_1 increases. This is because an increase in Z_1 helps in reducing coupling between the coils. One has to note that this analysis is only an example to show the decrease in P_{cp} when we increase Z_1. For future simulations, we would be using different parameter values based on our experiences in our laboratory.

3.5 *Gain, Coupled Gain and Noise Figure*

The discussion so far has focused on how impedance Z_1 (shown in Figure 11) can affect the coupling between coils and how we can reduce this coupling by increasing the impedance. To generalize our analysis, let us consider a system more complicated than the one shown in Figure 10. This system is comprised of two coils that receive high frequency signals and they are attached to separate preamplifiers (with input impedances $Z_{preamp1}$ and $Z_{preamp2}$) via an impedance transformation network (with input impedances Z_{high1} and Z_{high2}) as shown in Figure 12. Furthermore Coil 1 is identified as port 1 with the Preamp 1 output identified as port 2. Similarly, Coil 2 is port 3 and the output of Preamp 2 is port 4.
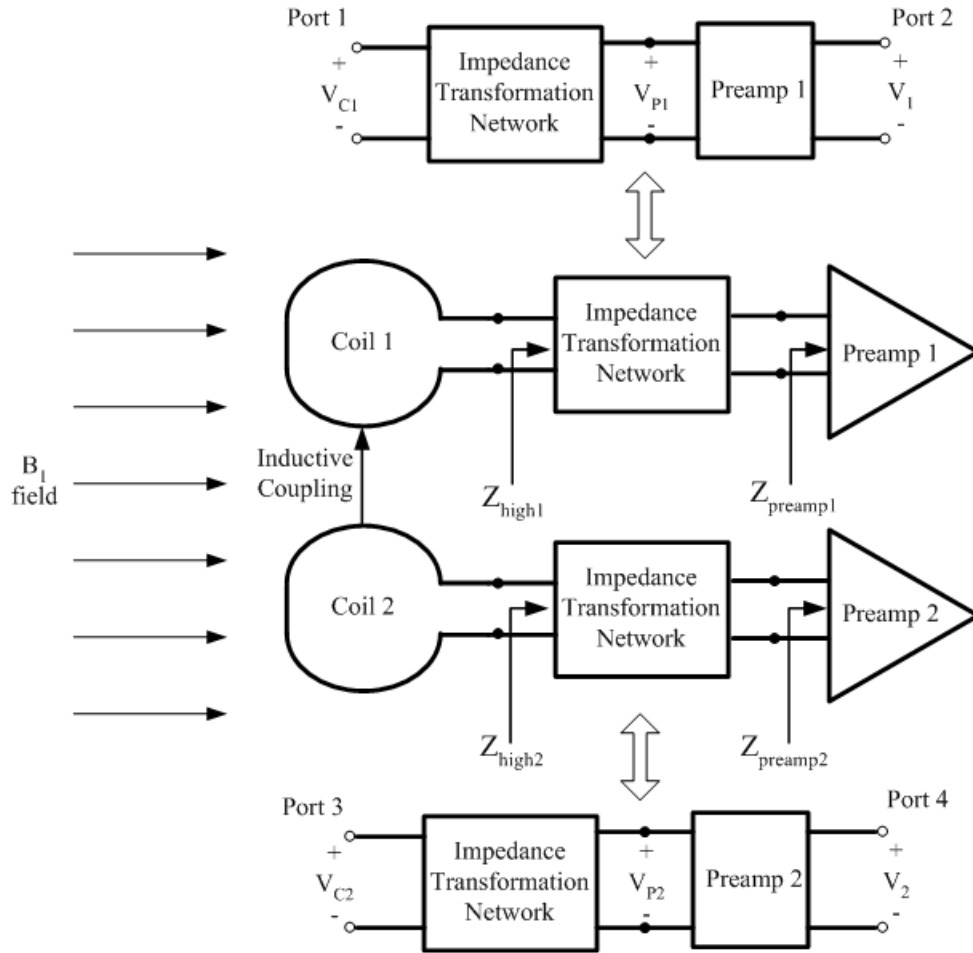
Figure 12. System diagram of two coils attached to two separate preamplifiers.

In an ideal system we would like Coil 1 to receive the B_1 signal only and not the coupled

signal. But this does not happen since Coil 1 also receives the coupled signal from Coil

2. In the previous section we attempted to isolate the coils by limiting the current flow in

one coil.   This is done by increasing the impedance and consequently reducing its

coupling effect on the other coil.   Using the same principle, we could limit the current

flow in Coil 2 by increasing Z_{high2}.   This would result in reducing its effect on Coil 1.

Similarly, we would reduce the effect of Coil 1 on Coil 2 by limiting the current flow in

Coil 1 by increasing Z_{high1}.

In this system, let us assume that impedance Z_{high1} or Z_{high2} depends on $Z_{preamp1}$ or $Z_{preamp2}$, respectively. Let us further assume they are inversely proportional to each other.

$$Z_{high1} \propto \frac{1}{Z_{preamp1}}$$
$$Z_{high2} \propto \frac{1}{Z_{preamp2}} \tag{18}$$

This can be accomplished by an impedance transformation network. The specifics of the impedance transformation network will be discussed in detail in later chapters.

Thus, according to equation (18), impedance Z_{high1} (or Z_{high2}) is made large by decreasing $Z_{preamp1}$ (or $Z_{preamp2}$). We can limit the current in the respective coil by making impedance Z_{high1} or Z_{high2} sufficiently large, which would result in minimized coupling between the coils. To make things clearer and easier to understand, let us first focus on Coil 1 in Figure 12. If Coil 1 is used to receive signals there would be a certain gain required by Preamplifier 1. Let us call this gain G_1. It is defined in terms of its input and output voltages V_{C1} and V_1 (illustrated in Figure 12) as:

$$G_1[dB] = 20 \cdot \log\left(\frac{V_1}{V_{C1}}\right) \tag{19}$$

The input and output relations can also be expressed in terms of scattering parameters (S-parameters). S-parameters are power wave descriptors that define the input-output relations of a network in terms of incident and reflected power waves. More details about on S-parameters will be discussed in Chapter 4, but for the moment G_1 in terms of S-parameters is defined as S_{21}. S_{21} can be defined as the forward voltage gain; it measures the amount of power transmitted from Coil 1 (port 1) to the Preamp 1 output (port 2). Therefore, G_1 in terms of S_{21} is:

$$G_1[dB] = 20 \cdot \log |S_{21}| \tag{20}$$

Unfortunately the coil also receives the undesired signal from Coil 2 due to inductive coupling. Eventually this coupled signal is also amplified. For our discussion we call this the coupled gain G_C and define it as.

$$G_C[dB] = 20 \cdot \log \left(\frac{V_1}{MV_{C2}} \right) \tag{21}$$

Here M is the mutual inductance coefficient between the two coils. In terms of S-parameters G_C is defined as S_{23}. It is a measure of the amount of power transmitted from Coil 2 (port 3) to the Preamp 1 output (port 2):

$$G_C[dB] = 20 \cdot \log |S_{23}| \tag{22}$$

In addition, the system also has internal noise associated with it that can be defined in terms of a noise figure. Noise figure, NF, is a measure of degradation in the SNR between the input and the output of the network and is defined in terms of the ratio of signal to noise power at the input and output ports as [10]:

$$NF[dB] = 10 \cdot \log \left(\frac{P_1/P_{n1}}{P_2/P_{n2}} \right) \tag{23}$$

where P_1 is the input power at port 1, P_{n1} is the noise power at port 1, P_2 is the output power at port 2, and P_{n2} is the output noise power at port 2 in a two-port network. Increasing Z_{high2} can reduce the undesired coupled signal from Coil 2. Similarly increasing Z_{high1} would reduce the coupled signal in Coil 2 as a result of Coil 1. But there has to be a limit on how large we can make Z_{high1}. A very large Z_{high1} would provide very little signal flow and a very small Z_{high1} would fail to adequately reduce signal coupling to Coil 2. An identical argument applies for Coil 2. To resolve this problem, a trade off is necessary for optimal operation.

If we think in terms of gain and noise figure, we would want the system to have a high gain and a low noise figure, while simultaneously minimizing the coupled gain. The overall quality of the system can be improved by minimizing the coupled gain. Again from the perspective of Coil 1, limiting the current in Coil 2 reduces the coupled gain because of reduced signal coupling due to increasing Z_{high2}. Therefore, to design a system as shown in Figure 12, there will be a tradeoff between gain, coupled gain, and noise figure. The system shown in Figure 12 was simulated at a frequency of 500MHz to analyze the trade offs. For this simulation, we use a coil with an inductance of 42nH and 2Σ series resistance. These values were selected since they are typical of the coils used by our laboratory. Also for the simulation, we used the parameters of a preamplifier designed in our laboratory with a gain of 32dB and a noise figure of 0.3dB. The result of this simulation from the perspective of Coil 1 is shown in Figure 13.
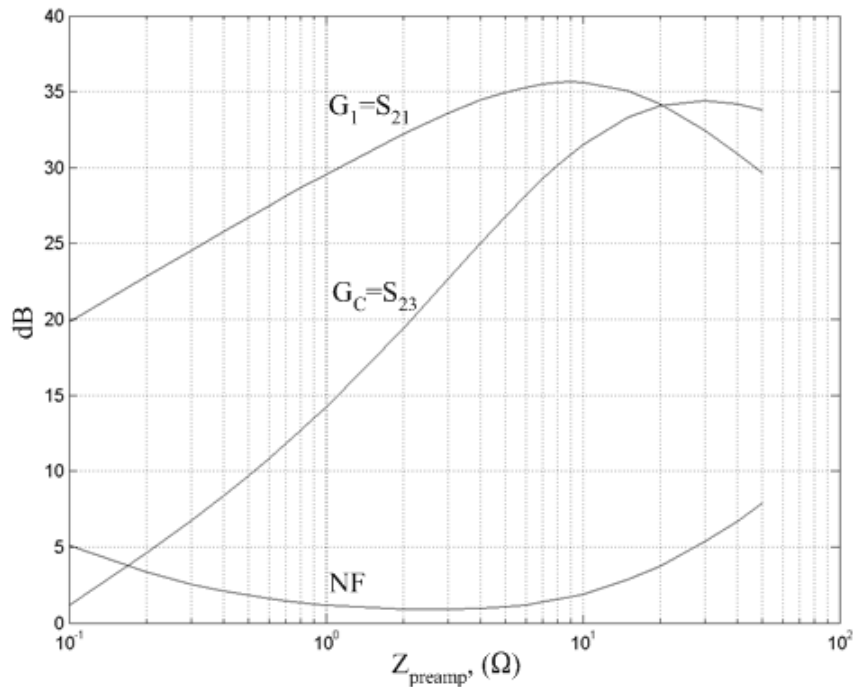

Figure 13. Gain, coupled gain and noise figure response as a function of Z_{preamp}.

In Figure 13 G_1, G_C, and NF are plotted as a function of Z_{preamp} where

$$Z_{preamp} = Z_{preamp1} = Z_{preamp2} \qquad (24)$$

In general the properties of the two coils and the preamplifier systems are identical (they constitute a phased array system).

In Figure 13, we can see that the noise figure is low at about $Z_{preamp}=1\Sigma$. We can also see that the parasitic gain increases as Z_{preamp} increases. This is expected since Z_{high2} decreases as $Z_{preamp2}$ increases, which causes the current to increase in the coil. The operating point, based on Figure 13, could be set at $Z_{preamp}=1\Sigma$. At this value we have a very low NF, a reasonably high gain, and a relatively good difference between G_1 and G_C. We would not set Z_{preamp} to values greater than 1Σ since the difference between G_1 and G_C decreases. Equally, we would not set Z_{preamp} to values lower than 1Σ, since it is difficult to design an impedance transformation network that would transform Z_{high} to impedances lower than 1Σ.

The purpose of this section is to show the effects of coupling and the parameters that need to be considered. The results in Figure 13 show that $Z_{preamp}=1\Sigma$ is a good compromise. However, these results would be different for different systems. Nevertheless, the principle for decoupling holds true and will be used in this work.

4 RF and Microwave Fundamentals

4.1 Resonance

Most RF coils are designed around the concept of resonance. Imaging coils are composed of inductive and capacitive elements. These elements determine the frequency at which the coil resonates. Since the magnetic field is directly proportional to the magnitude of the current, RF coils operating at resonant frequency produce maximum magnetic field strength at a relatively low input voltage. The relation between angular resonance frequency, inductor and capacitor values is given by the Thompson formula:

$$\omega = \frac{1}{\sqrt{LC}} \tag{25}$$

Another important parameter of a resonant circuit is its quality factor Q. It is a measure of the loss of a resonant circuit, and is affected by parameters such as the strength of the $\mathbf{B_1}$ field, the SNR of the image, and the sensitivity of the RF coil. The quality factor of a coil is defined as [11]:

$$Q = 2\pi \frac{\text{maximum energy stored}}{\text{total energy dissipated per cycle}} \tag{26}$$

4.2 *Matching*

Matching is an important criterion when designing RF circuits. When a load impedance differs from the source impedance, a matching network is required to enable the delivery of maximum power from the source to the load. The condition for maximum power transfer is given by the conjugate matching theorem, which states that maximum power is transferred from the signal source to the load if and only if the impedance of the signal source is equal to the complex conjugate of the load impedance.

Matching networks can be designed using various methods. The analytical approach yields precise results and is suitable for computer synthesis. However, this approach becomes very complicated and computationally intensive as the component count increases. A more convenient approach is to use the Smith Chart. In this approach the design complexity remains almost independent of the number of components used in the network. It furthermore gives a feel of how the impedance matching is influenced by the changes in circuit elements and topology. The effect of connecting a reactive element to a complex load can be summarized by the following rules:

- The addition of a reactance connected in series with a complex impedance results in motion along a constant-resistance circle in the combined ZY Smith Chart [10].

- A shunt connection produces motion along a constant-conductance circle.

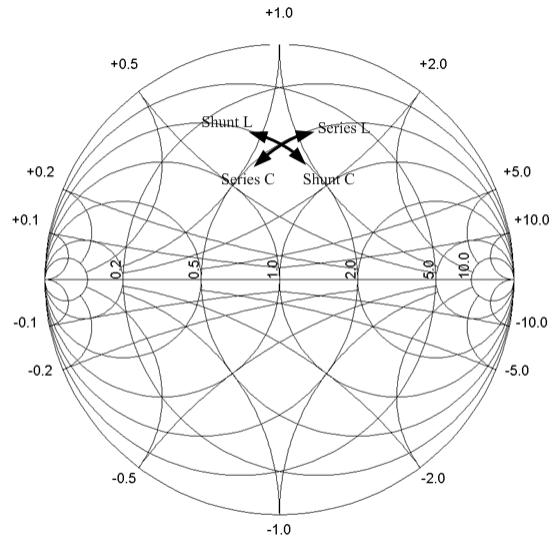Both motions are shown in Figure 14 for the combined ZY Smith Chart.

Figure 14. Effect of series and shunt connections of L and C in the complex impedance plane.

4.3 Scattering Parameters

It is difficult to perform conventional circuit analysis using parameters such as the h-parameters and Z-parameters in high frequency systems. Short circuit and open circuit conditions in high frequencies do not exhibit the same behavior as in low frequencies. Specifically, a short circuit can depend on the inductive behavior of the wire and likewise, an open circuit exhibits a capacitive behavior, potentially lowering the impedance to a small value at high frequencies. Under high frequency operation these shortcomings are avoided by the use of scattering parameters or S-parameters.

S-parameters are descriptors that permit us to define input and output relations in terms of incident and reflected normalized power waves [10]. They describe the behavior of the circuit at high frequencies. The incident normalized power wave, a_n, and the reflected normalized power wave, b_n, are given by:

30

$$a_n = \frac{1}{2\sqrt{Z_0}}\left(V_n + Z_0 I_n\right) \qquad (27)$$

$$b_n = \frac{1}{2\sqrt{Z_0}}\left(V_n - Z_0 I_n\right) \qquad (28)$$

Here index $n=1,2$ refers to the port number and Z_0 is the characteristic impedance of the connecting lines on the input and output side of the network. The port voltage and current, V_n and I_n, are defined as:

$$V_n = \sqrt{Z_0}\left(a_n + b_n\right) \qquad (29)$$

$$I_n = \frac{1}{\sqrt{Z_0}}\left(a_n + b_n\right) \qquad (30)$$

Figure 15 depicts the convention used to define S-parameters for a two-port network.
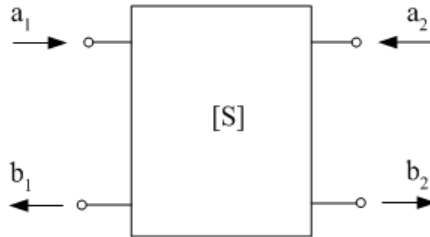

Figure 15. Convention used to define S-parameters for a two-port network.

Based on the convention depicted in Figure 15 and equations (27) and (28), the S-parameters for a two port network are defined as:

$$\begin{pmatrix} b_1 \\ b_2 \end{pmatrix} = \begin{pmatrix} S_{11} & S_{12} \\ S_{21} & S_{22} \end{pmatrix}\begin{pmatrix} a_1 \\ a_2 \end{pmatrix} \qquad (31)$$

4.4 RF Coils

4.4.1 Volume Coils and Surface Coils

RF coils are a key component in a magnetic resonance imaging system. RF transmit coils generate pulses at Larmor frequency and excite the nuclei in the object to be imaged. The RF receiver coils pick up the signals emitted by the nuclei at the Larmor frequency. Designing RF coils has for the most part been a compromise between generating a uniform magnetic field and obtaining a good SNR. A large coil will generate a more uniform magnetic field when compared to a smaller one. However, a smaller coil possesses a better SNR than a bigger coil. Consequently, RF coils are therefore designed according to their use. There are many different kinds of RF coils that have been developed [1] and they can be generally categorized into two main groups: volume coils and surface coils.

Volume coils are used to produce a uniform magnetic field in the region of interest. The object to be imaged is usually enclosed by this type of coil. Volume coils can both be used as a transmitter and a receiver. Examples of a volume coil and a surface coil are depicted in Figure 16.
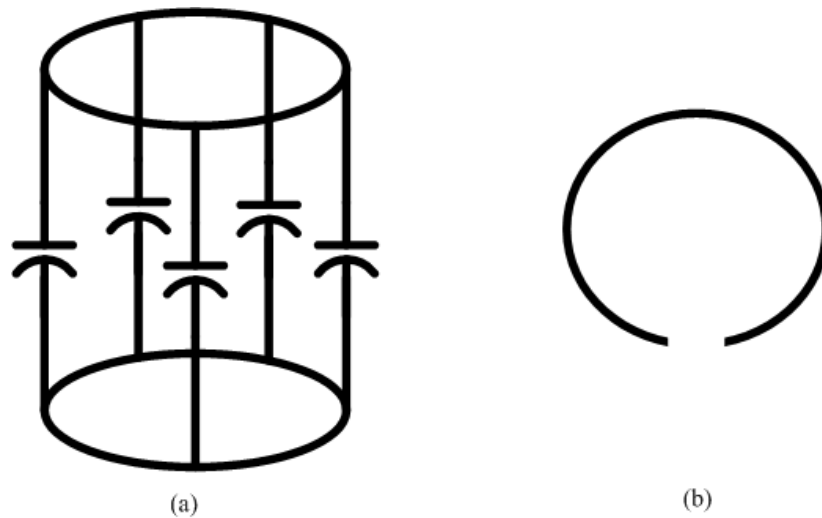
Figure 16. (a) Bird cage volume coil [1], (b) circular loop surface coil.

Surface coils are single loop or multiple loop coils. They are circular or rectangular in shape and are placed over the region of interest. Since they are typically smaller than volume coils, they sacrifice image uniformity for high SNR. In general, they are mostly used as receiving only coils.

4.5 Surface Coil Model

Surface coils are usually made up of conducting wires and capacitors. There are several numerical and analytical methods available for modeling surface coils. Each method offers a variety of capabilities with various degrees of accuracy. The lumped element circuit model is one of the traditional ways of modeling an RF coil [1] and is shown in Figure 17. The basic principle of this method is to treat of all inductive and capacitive contributions as lumped elements. In this regard, coils are treated as lumped inductors and likewise capacitive elements are treated as lumped capacitors. The circuit can then be analyzed using basic circuit analysis rules based on Kirchoff's theory. This makes it very practical: it is used for most MRI RF coil modeling and analyses. However, it is

important to note that this method yields reasonably accurate results at low frequency and moderately high frequencies. The model becomes inaccurate when the size of the coil approaches the wavelength at the circuit's operating frequency [9].
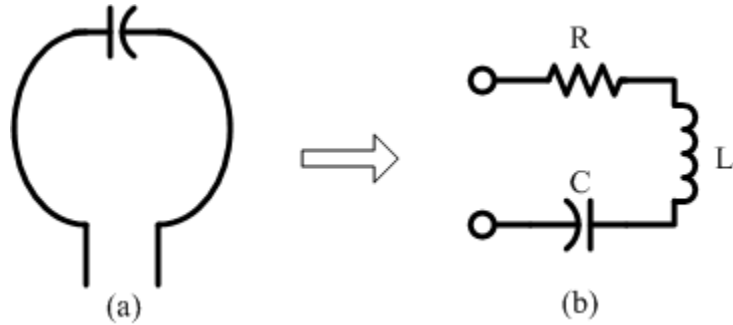
Figure 17. Equivalent model - (a) RF coil, (b) lumped element representation.

4.6 **Phased Array Coils**

A phased array system is essentially composed of multiple receiver coils as shown in Figure 18. In a phased array coil, individual coil signals are generally combined to obtain a uniform image. Each coil is connected to an independent preamplifier attached to a receiver channel. The signal outputs of the receiver channels are digitized, stored in memory, and then phase shifted and combined depending on the point in space from which the signal originates [22]. In this configuration, a larger imaging region (Region of Imaging or ROI) is covered while maintaining a high SNR.
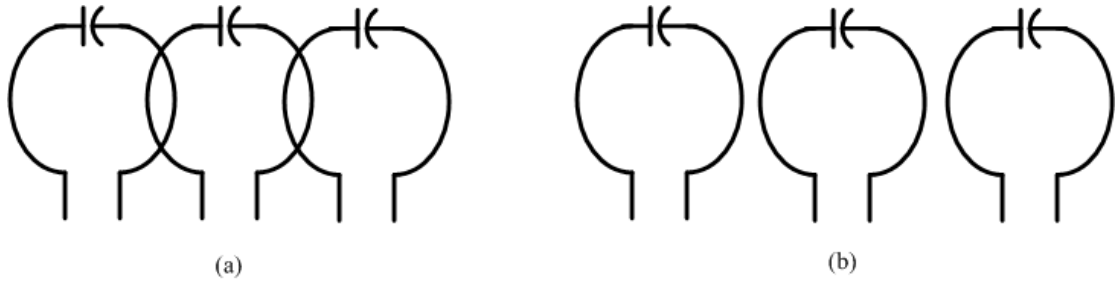
Figure 18. Phased array coil configuration (a) overlapped and (b) separate coil.

In order to obtain a high SNR, it is necessary to ensure that signal coupling is reduced between the coils.

4.6.1 Switched and Parallel Acquisition Arrays

The system by which a phased array system acquires a signal can be categorized into two classes: switchable coil arrays and parallel acquisition coil arrays [26].   The block diagram for these two classes is shown in Figure 19.
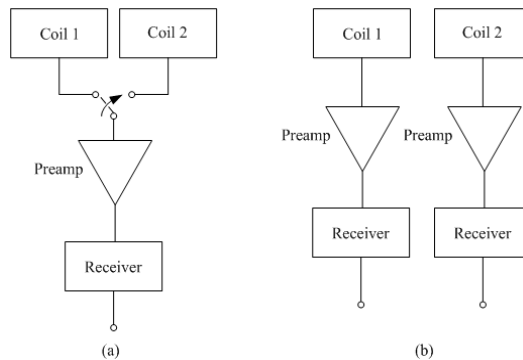
Figure 19. RF coil block diagrams: (a) switched arrays, (b) parallel acquisition arrays.

Switchable coil arrays can be operated as a single reconfigurable receiver system. The user selects the optimal coil configuration and a single data set is collected for the coil array. This type of array is generally simple and inexpensive to implement.

In parallel acquisition arrays the coils are operated simultaneously and independently. Signals obtained using this system can be combined in an effort to improve the SNR. The method is more expensive due to the cost of additional receiver channels. It also

poses the technical challenge of reducing the coupling between the coils. However this method is more flexible and offers an improvement in SNR while maintaining the same imaging time. This research effort is based on this technique.

4.6.2 Decoupling of phased array coils

When resonant loops, which are tuned to the same resonant frequency, are placed together or near one another, mutual inductance between the coils causes the resonances to split. The splitting results in a loss of sensitivity at the resonant frequency [21]. As a result, it is desirable to decouple the coils by reducing the mutual inductance between the coils.

In the classical MRI phased-array design, adjacent coils are overlapped as shown in Figure 18(a) to force the mutual inductance to equal to zero. When two coils are overlapped as shown in Figure 20, and if Coil 1 is producing a magnetic flux, there is a certain position of overlap at which the total magnetic flux passing through Coil 2 is zero. This is because the flux density through the overlapped part of Coil 2 is larger and cancels the flux density thorough the un-overlapped part of the Coil 2 (un-overlapped part of the coils is larger in area). In this case, the EMF in the second coil is zero and it indicates that the mutual inductance between these coils is zero at this position based on Faradays law given in equation (32), where **E** is the electric field and **B** is the magnetic flux density.
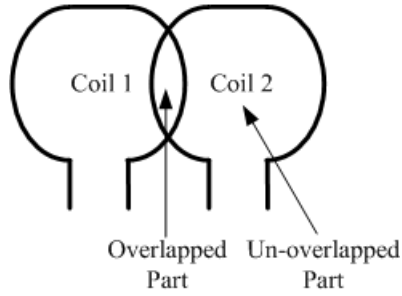
Figure 20. Overlapped coils cancel mutual inductance.

$$\oint_C \mathbf{E} \cdot d\mathbf{l} = -\int_S \frac{\partial \mathbf{B}}{\partial t} . d\mathbf{s} \qquad (32)$$

Here C is the contour of the coil along which the electric field is integrated (dl is the line element) and S is the associated coil area.

However, the use of overlapping coils to cancel mutual inductance is not a complete solution because it cannot in general work for an array with more than three elements [24]. In another technique, low noise preamplifiers are used to isolate the coupling between the coils. This helps in eliminating inductive coupling between the coils. A block diagram illustrating this technique is given in Figure 21.

Figure 21. Block diagram of coil, interface, and preamplifier [1].

To illustrate decoupling using preamplifiers by generically considering the gain and the coupling gain, we consider the example below. Figure 22 shows two surface coils

connected to their respective preamplifiers. The interface network has been removed to simplify the analysis.
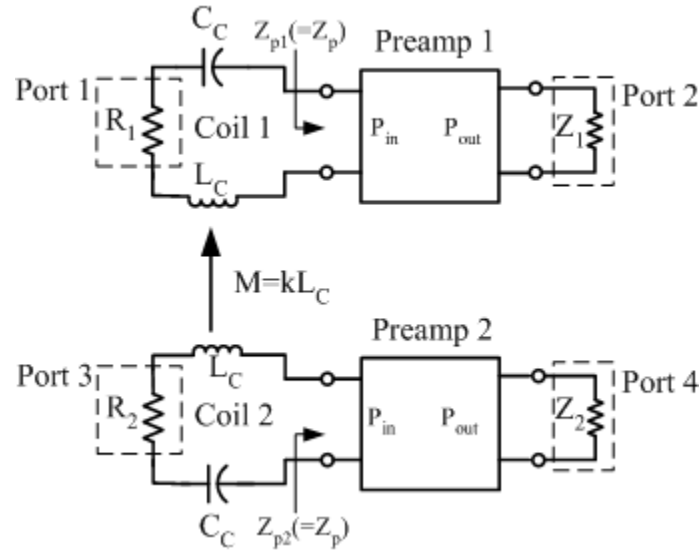
Figure 22. Decoupling with preamplifier.

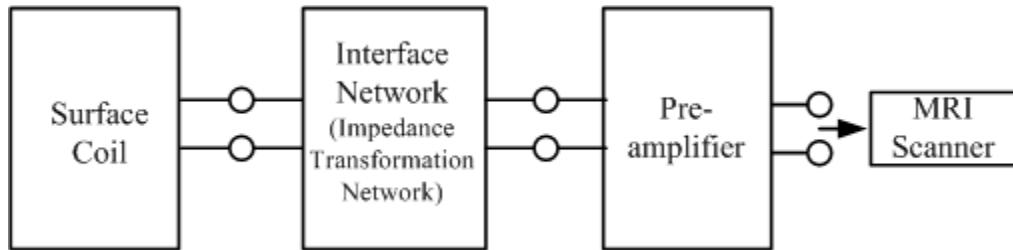In this example, the coils are a part of a phased array system. In a single coil system, there are primarily two kinds of signals received by the coil, one is the signal from the sample and the other signal is the thermal noise generated by the coil and the sample being imaged. When two or more coils are placed closed to each other, signals are also coupled from one coil to another due to inductive coupling. The performance of the coils can be improved by limiting inductive coupling between the coils. Increasing the preamplifier impedance limits the current flow in the coils.

The circuits in Figure 22 were simulated to demonstrate signal decoupling by limiting the current flow in the coil (i.e. increasing the preamplifier impedance as seen by the coil). Here it is important to note that limiting the current in Coil 2 improves the performance of Coil 1 and vice–versa as explained in Section 3.5. The simulations were conducted at 500MHz resonant frequency with an inductance of 42nH and 2Σ series resistance (same

as in Section 3.5). The preamplifier was modeled by its S-parameters for the simulation. The preamplifiers were set to have a gain with magnitude equal to 1 and the characteristic impedance of the preamplifiers was set to 2Σ to match the coil resistance. This was done to set the gain equal to 1 regardless of the preamplifier input impedance for a single coils system. The preamplifier output characteristic impedances were set to 50Σ.

In order to explain the transfer of signals in terms of S-parameters, let us assume that R_1 is the impedance looking into port 1 and that Z_1 is the impedance looking into port 2 for Coil 1. Let us also assume that R_2 and Z_2 are the impedances looking into port 3 and port 4 for Coil 2. With reference to Coil 1, under ideal conditions we would want to see S_{21} equal to a magnitude of 1 (or 0dB) and a low S_{23} (S_{21} is the signal transferred from Coil 1 to the output of Preamp 1, and S_{23} is the coupling signal transferred from Coil 2 to the output of Preamp 1). Let us now examine how the signal transfer is affected when we change the impedance Z_{p2} by referring to the simulation results presented in Figure 23. In the figure we can see that S_{21} increases and S_{23} decreases as Z_{p2} increases (in the figures Z_p is equal to Z_{p1} and Z_{p2}, since the two coils are a part of phased array and possess identical properties). This behavior happens because we are reducing the inductive coupling of signal from Coil 2 to Coil 1. Although the coupling coefficient is about 0.1 in a realistic system, we exaggerate the variation in S_{21} and S_{23} by setting k is set to 0.01. The simulation result is shown Figure 23.

The performance of the coil starts to decrease as we increase the coupling coefficient. To show this, additional simulations were conducted with different values of k. These results are shown in the figures below. The coupling coefficient k is set to a realistic value of 0.1 for the result shown in Figure 25. In Figure 24 and Figure 26 k is set to 0.05 and 0.2 to exaggerate the variation in S_{21} and S_{23}.
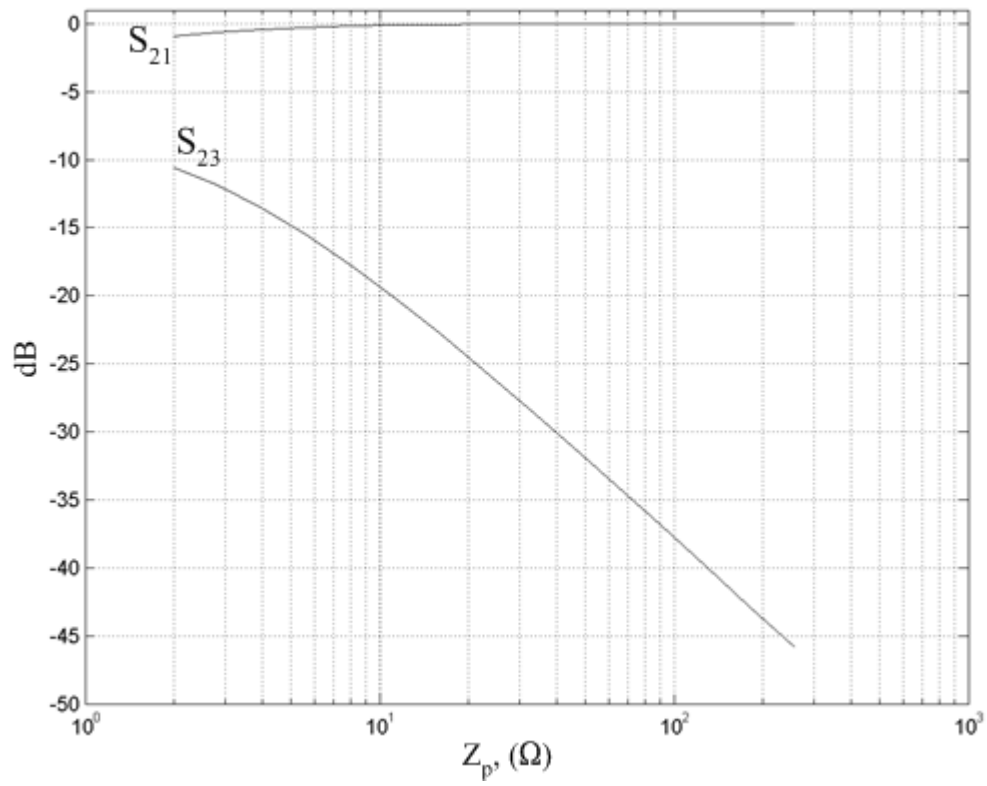
Figure 23. Simulation results with k=0.01.
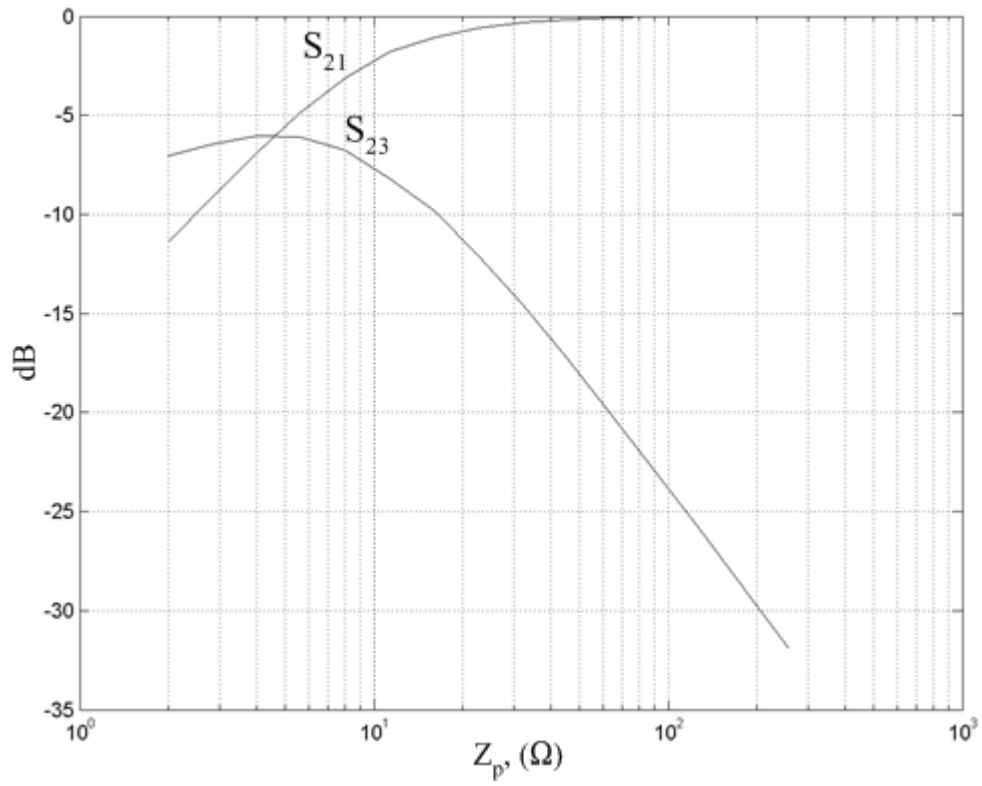
Figure 24. Simulation results with k=0.05.
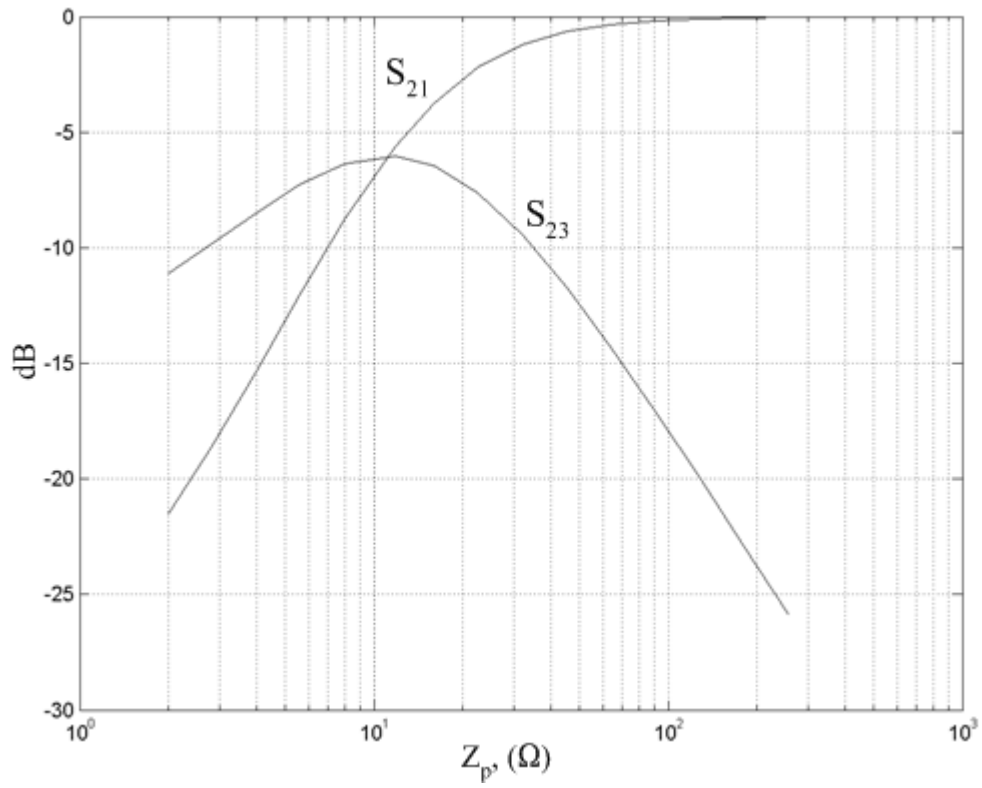
Figure 25. Simulation result with k=0.1.
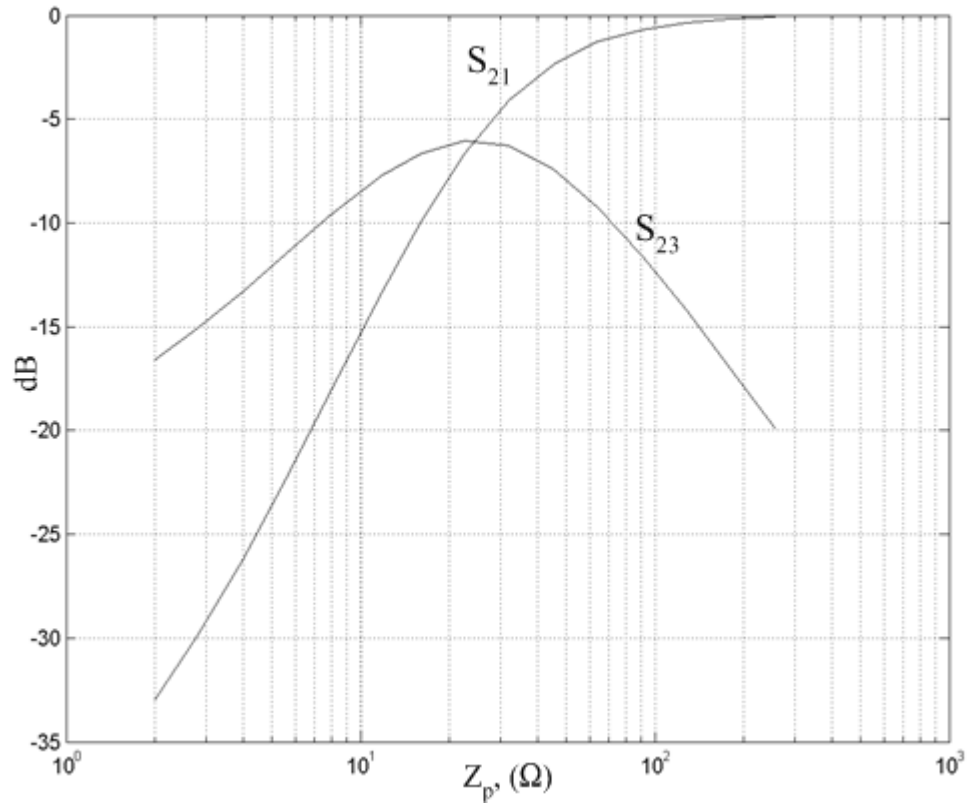
Figure 26. Simulation result with k=0.2.

With these simulation results we have demonstrated that we can indeed reduce undesired signal coupling by increasing the preamplifier impedance. As a result, with this understanding we can proceed to design the surface coil and the preamplifier unit.

5 Surface Coil - Interface Design and Simulation

5.1 Interface Network Circuit

In the previous chapter we have discussed the use of preamplifiers to decouple coils as part of a phased array system. The preamplifier is connected to the coil by an interface network as shown in Figure 27.
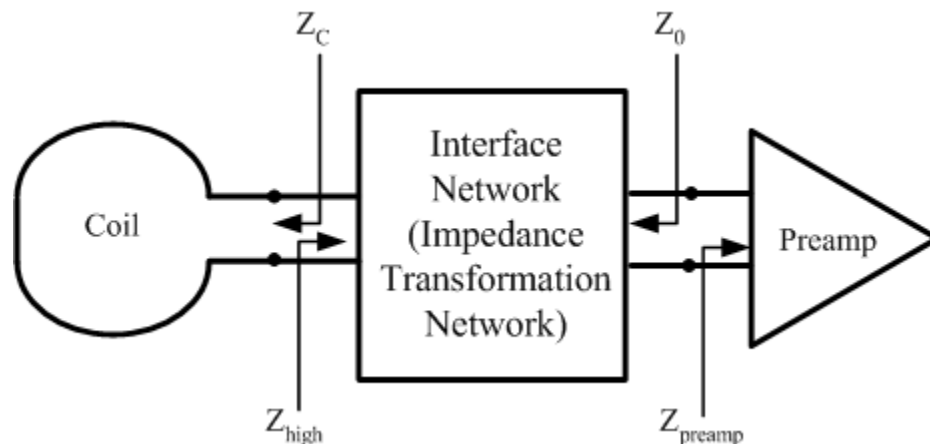
Figure 27. System diagram of coil connected to the preamplifier by an interface network.

The interface network is an impedance transformation network that transforms the coil series resistance Z_C to Z_0 as seen by the preamplifier (Z_0 is the characteristic impedance

of the cable that will be used to connect the coil and the interface network to the preamplifier). In the opposite direction it also transforms the preamplifier impedance Z_{preamp} into Z_{high}. Here again, Z_{high} is the impedance seen by the coil and its magnitude controls the current circulating in it. To further understand how the impedance transformation network affects the impedances of the coil and the preamplifier based on direction, one can separate the components in Figure 27 as shown in Figure 28 and Figure 29.
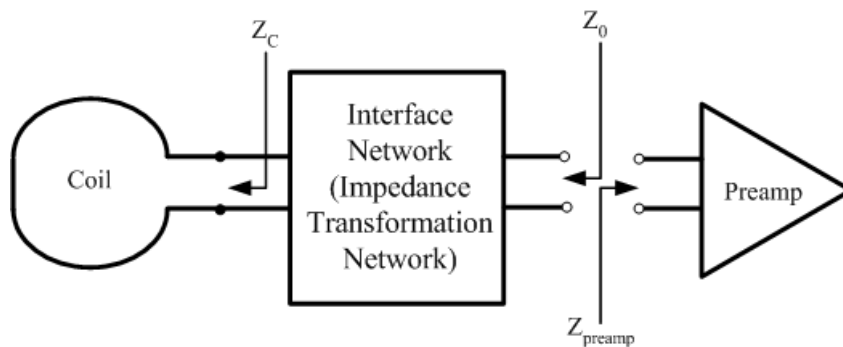
Figure 28. Diagram showing Z_C transformed to Z_0.

Figure 28 portrays the structure that is considered when measuring the impedance looking into the preamplifier (Z_{preamp}) and also measuring the impedance of the impedance transformation network looking towards the coil. Figure 29 represents the structure when measuring the coil resistance and the impedance of the impedance transformation network looking into the preamplifier (Z_{high}).
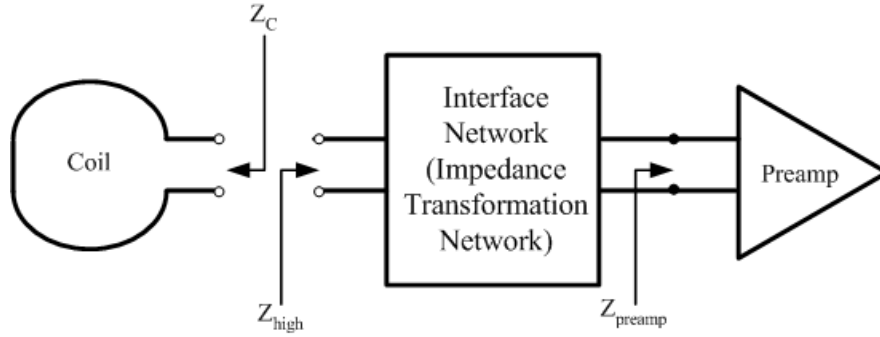
Figure 29. Diagram showing Z$_{preamp}$ transformed to Z$_{high}$.

In this research, a balun circuit shown in Figure 30 is employed as an interface. A balun in its simplest form is a transformer that converts a balanced signal to an unbalanced one and vice-versa. The details of the balun transformer involve capacitors C_{B1} and C_{B2} and inductors L_{B1} and L_{B2}. In Figure 30 (b), Z_{IN} denotes the input impedance to the coil and Z_{OUT} denotes the output impedance to the preamplifier.
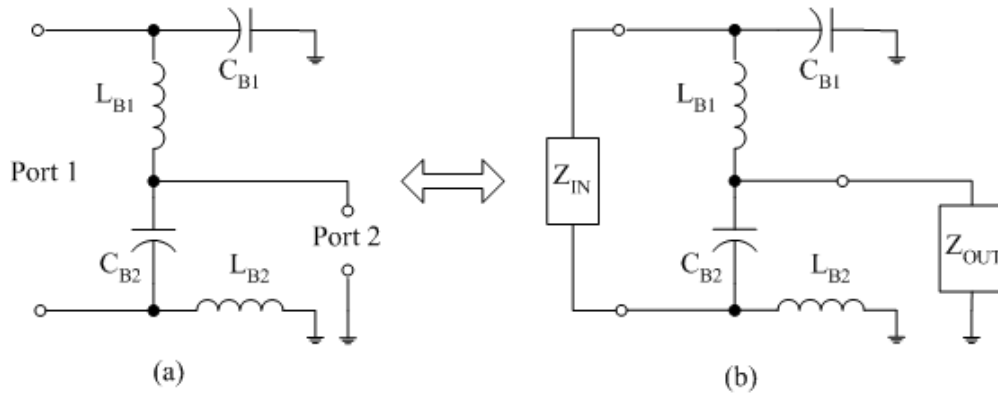
Figure 30. Generic balun circuit used for matching the coil to the receiver (a) port designation and (b) impedance designation.

The balun interface circuit transforms the input impedance to a different impedance at resonance. To show how this is achieved, let us start by applying the star-delta transformation technique to the circuit depicted in Figure 30 (b). The result of this transformation is show in Figure 31.

46
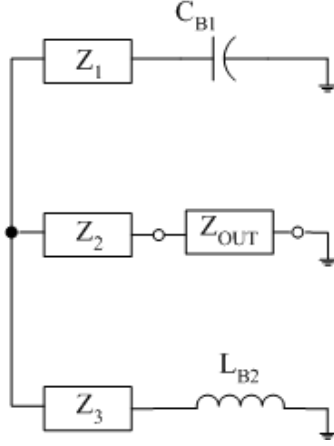
Figure 31. Transformed circuit representation of circuit depicted in Figure 30.

Here the impedances Z_1, Z_2 and Z_3 replace Z_{IN}, L_{B1}, and C_{B1}. To derive the expressions

for Z_1, Z_2 and Z_3, we adopt the following impedance notations:

$$Z_{LB1} = j\omega L_{B1},$$

$$Z_{LB2} = j\omega L_{B2},$$

$$Z_{CB1} = 1/j\omega C_{B1}, \text{ and}$$

$$Z_{CB2} = 1/j\omega C_{B2}.$$

From Figure 30 and Figure 31, the transformation equations can be derived as follows:

$$Z_1 = \frac{Z_{LB1}Z_{IN}}{Z_{LB1} + Z_{CB2} + Z_{IN}} \tag{33}$$

$$Z_2 = \frac{Z_{LB1}Z_{CB2}}{Z_{LB1} + Z_{CB2} + Z_{IN}} \tag{34}$$

$$Z_3 = \frac{Z_{CB2}Z_{IN}}{Z_{LB1} + Z_{CB2} + Z_{IN}} \tag{35}$$

Furthermore, setting $L_{B1} = L_{B2}$ and $C_{B1} = C_{B2}$, we have:

$$Z_{IN} = Z_{LB1} = Z_{LB2} \text{ and}$$

$$Z_{CB} = Z_{CB1} = Z_{CB2}$$

According to the above definitions, and under the condition of resonance, equations (33), (34) and (35) become:

$$Z_1 = Z_{LB1} \tag{36}$$

$$Z_2 = \frac{Z_{LB1}Z_{CB2}}{Z_{IN}} \tag{37}$$

$$Z_3 = Z_{CB2} \tag{38}$$

We can see from Figure 31, that series impedance Z_{CB1} cancels Z_1, and impedance Z_{LB2} cancels Z_3. Therefore:

$$\begin{aligned} Z_1 + Z_{CB1} &= 0 \\ Z_3 + Z_{LB2} &= 0 \end{aligned} \tag{39}$$

Hence,

$$Z_{OUT} = Z_2 \tag{40}$$

Upon substituting equation (37) into equation (40) becomes:

$$Z_{OUT} = \frac{Z_{LB1}Z_{CB2}}{Z_{IN}}$$
$$Z_{IN}Z_{OUT} = \frac{L}{C} \tag{41}$$

Equation (41) states the relationship between the balun components (the inductors and capacitors) and the input and output impedances. It describes the function of the balun interface circuit as an impedance transformer that transforms the input impedance to the output and vice-versa at a given resonant frequency.

As stated above, the balun interface circuit transforms Z_C, the coil series resistance, to Z_0 while simultaneously transforming the preamplifier impedance Z_{preamp} to Z_{high} as seen by the coil. To illustrate the impedance transformation properties of the balun, we consider a coil with $Z_C = 2\Omega$ resonating at 500MHz using a cable with Z_0 equal to 50Ω. First, we calculate the values for the balun components, which are dictated by the transformation of Z_C to 50Ω. The calculation to find the values of the inductors (L_{B1} and L_{B2}) and capacitors (C_{B1} and C_{B2}) is based on the relation $\omega = 1/\sqrt{LC}$ and equation (41). The numerically calculated values for the inductor and capacitor are 3.18nH and 31.83pF. To validate our calculation we substitute L and C as follows:

$$Z_{OUT} = \frac{L}{Z_C \cdot C} = \frac{3.18nH}{2\Omega \cdot 31.83pF} \approx 50\Omega \tag{42}$$

The balun also transforms Z_{preamp} to Z_{high} (the values for the inductors and the capacitors have already been set to transform Z_C to 50Ω). If the value of Z_{preamp} is equal to 1Ω, then the balun interface will transform it to 100Ω, as shown in equation (43):

$$Z_{high} = \frac{L}{Z_{preamp} \cdot C} = \frac{3.18nH}{1\Omega \cdot 31.83pF} \approx 100\Omega \tag{43}$$

The difference in the impedance transformations from the coil to preamplifier and preamplifier to coil is due to the fact that the input reflection coefficient of the active device approaches unity. This is discussed in detail in Chapter 7.

5.2 Interface Network Design

In the previous section we have described the balun interface circuit and its role as an impedance transformation network. In this section we shall implement the balun and design an interface network. The designed interface is given in Figure 32.
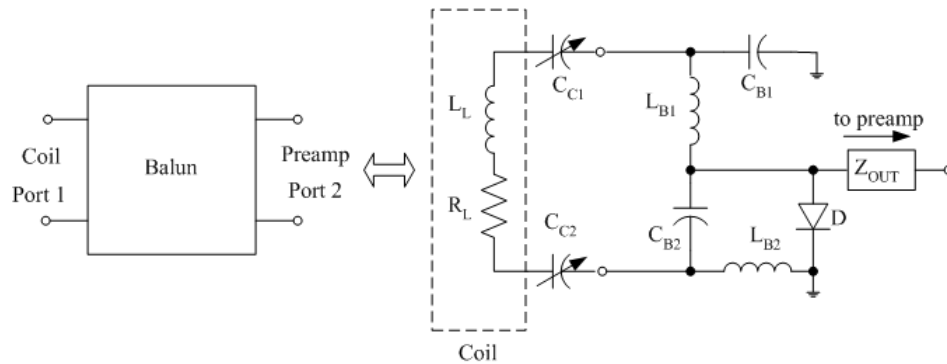
Figure 32. Interface network design.

The circuit shows a balun interface network connected to a surface coil modeled by an inductor L_L and resistor R_L. Capacitor C_{C1} and C_{C2} are variable capacitors that can be tuned to cancel the coils reactance at resonance. The diode D operates as a PIN-diode for detuning purposes. Detuning is the process of shifting the surface coil's resonance frequency when the volume coil is transmitting a signal. This is done to prevent the surface coil from interfering with the volume coil. The PIN-diode is reverse-biased when the coil is in normal receive mode and forward biased when the coil is in detuning mode. During detuning, the diode acts as low impedance. The balun transforms this into a high impedance, preventing current flow in the coil during a transmit pulse. We do not use the preamplifier for detuning because it behaves non-linearly at higher power level which is the case during a transmit pulse and the simple impedance relation no longer holds true.

50

5.3 Interface Network Simulation

The circuit in Figure 32 was simulated to confirm the proper operation of the interface circuit and also to investigate its performance. The S-parameter results of the simulations helped to establish the effectiveness of the balun interface as an impedance transformer. The simulations were conducted at 500MHz with a coil inductance of 42nH and with a 2Σ series resistance. These values were selected since they are typical of coils developed in our laboratory.   The balun inductors and capacitors values were calculated to be 3.18nH and 31.83pF, respectively.

The S-parameter simulation results are shown in Figure 33. Reactances of capacitors C_{C1} and C_{C2} cancel the coil's inductance. This leaves a purely resistive load across the coil. As a result, we do not have additional impedances that affect matching.   The input reflection coefficient, S_{11} simulation result is shown in Figure 33. Here we can see that S_{11} is minimum at the resonant frequency.   The forward voltage gain S_{21} response is shown in Figure 34. Here we can see that it is at its maximum at the resonant frequency.
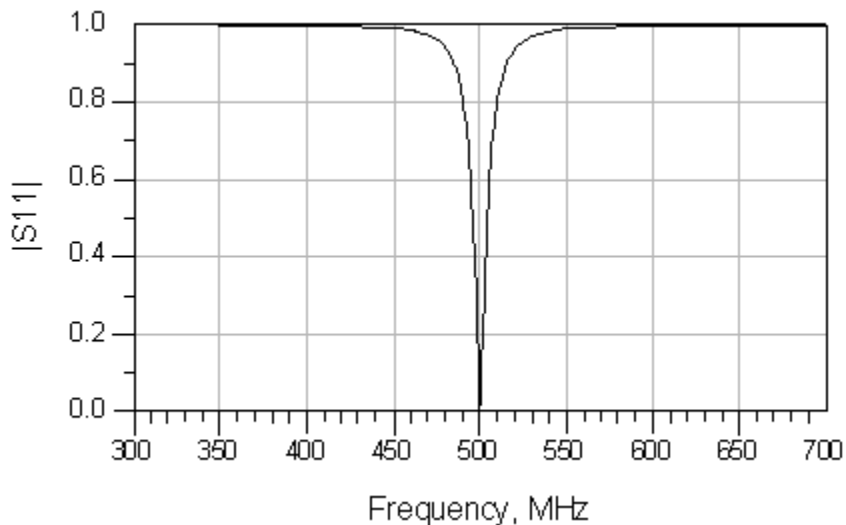
Figure 33. S-parameters simulation results: magnitude of S_{11}.
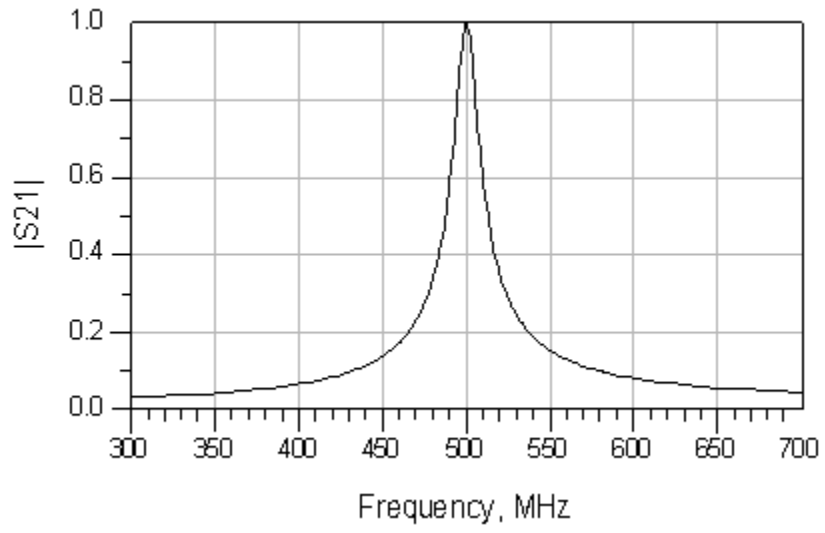
Figure 34. S-parameters simulation results: magnitude of S_{21}.

6 Surface Coil – Interface Construction and Testing

6.1 Interface Construction

The construction of the interface starts by determining the balun component values, which transforms the coil's resistance to 50Ω. This requires an estimate of the coil's resistance. The arrangement to measure the surface coil's resistance is illustrated in Figure 35.
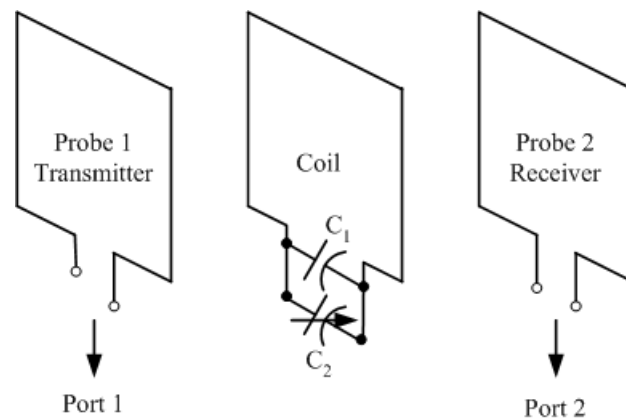
Figure 35. Arrangement to find the coil's resistance.

Figure 35 illustrates two probes attached to the network analyzer with the coil between them. The two probes are weakly coupled to the coil and probe 1, which is attached to port 1, operates as the transmitter while probe 2, which is attached to port 2, operates as

the receiver. The coil is made of copper and has two tuning capacitors C_1 and C_2 (variable) attached to it in parallel so as to create a resonant circuit. The quality factor Q of the coil can be determined from S_{21} by calculating the ratio of the resonant frequency to the 3dB bandwidth. The measurement of Q was conducted under loaded condition to emulate the impedance seen by the coil while receiving images during an actual MRI test. A biological sample (thumb) was used as the load. The sample was placed under the coil and the data was recorded. The coil resistance can then be calculated from the quality factor according to equation (44), where R_L is the coil's resistance and L_L is the coil's inductance (as measured with the impedance analyzer).

$$R_L = \frac{\omega L_L}{Q} \qquad (44)$$

The inductance was measured to be $L_L \approx 40nH$ and the quality factor was calculated to be $Q \approx 100$. According to equation (44), the resistance of the coil at resonant frequency of 200MHz is approximately 0.5Ω. The coil was constructed for 200MHz even though all the simulations were conducted for 500MHz, since a 4.7T system was available for testing purposes.

The balun component values (under resonant conditions) were calculated after determining the value of R_L. The inductors L_{B1} and L_{B2} were calculated to be 3.978nH and the capacitors C_{B1} and C_{B2} were calculated to be 159.2pF. The schematic of the constructed coil is shown Figure 36 (a). Capacitors C_{C1}, C_{C2} and C_{C21} (variable) are tuning capacitors for the coil while C_{B1}, C_{B11}, C_{B2}, and C_{B21} are the balun capacitors combined in parallel for proper matching at the resonant frequency.
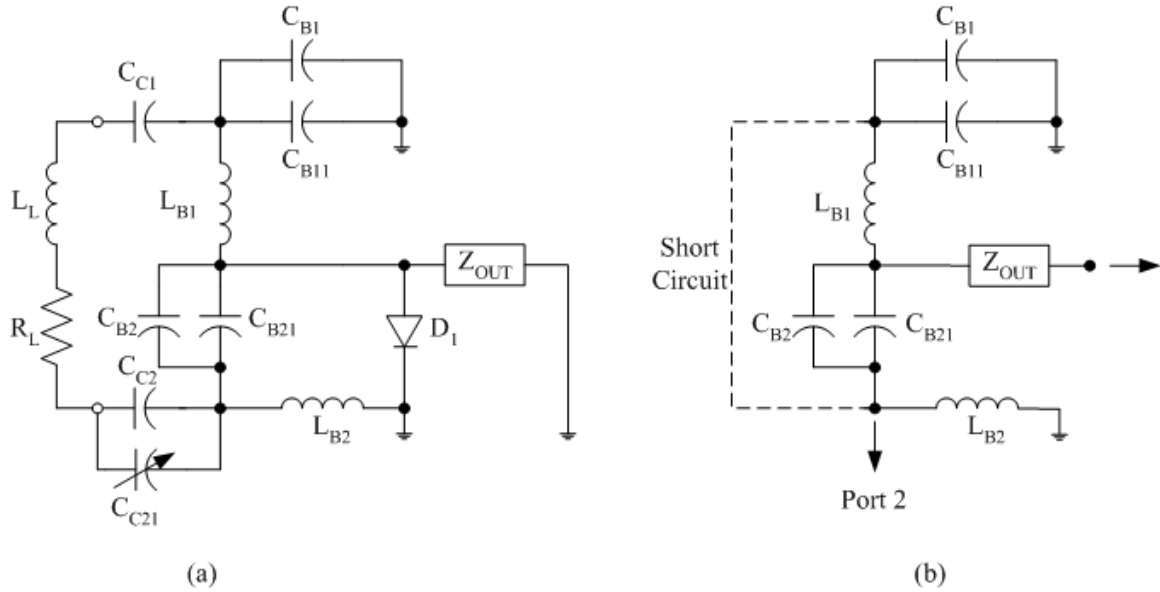
Figure 36. (a) Schematic of the constructed coil and (b) schematic of balun test circuit.

It was critical to ensure the proper operation of the balun at the resonant frequency. The balun was tested as shown in Figure 36 (b) upon completion of its construction. In this arrangement the nodes between inductor L_{B1}, capacitor C_{B1} and inductor L_{B2}, capacitor C_{B2} were shorted and connected to port 2 of the network analyzer. Network analyzer port 1 was connected to the node between L_{B1} and C_{B2}. When the circuit is setup in this way, the impedance of the circuit turns out to be very large during resonance. This would imply that S_{21} is very low as shown in Figure 37 because signal is not transferred from port 1 to port 2.
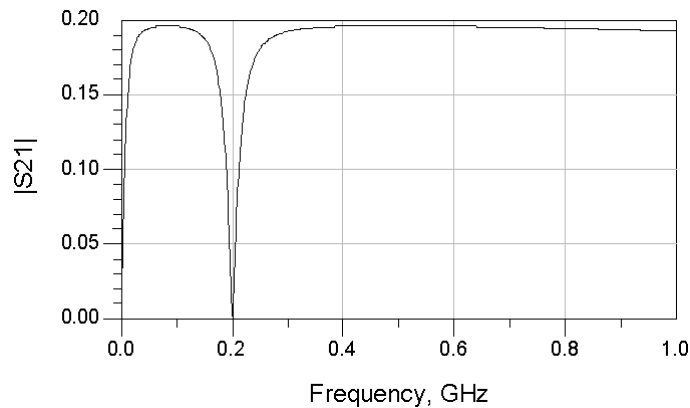
Figure 37. Simulation of S_{21} of balun test circuit.

55

After testing the balun in the network analyzer and confirming its proper operation, the PIN diode and the RF cable were soldered on the PCB to complete the coil construction. The constructed coil is shown in Figure 38 and Figure 39.
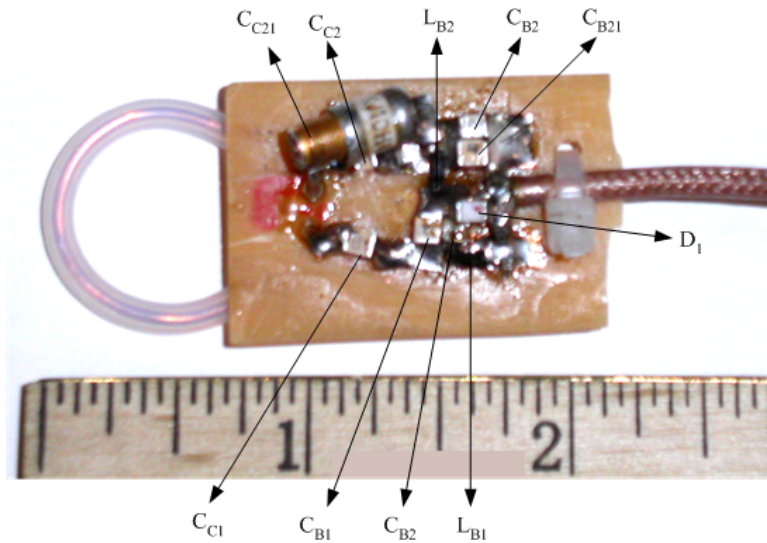
Figure 38. Coil - top layer view.

Figure 39. Coil - bottom layer view.

6.2 Magnet Test

After construction the coil tested in a 4.7T magnet system. The setup for this test is given

in Table 1. The image acquired during this test is displayed in Figure 40.

Table 1. Test setup parameters.

Phantom	Mineral oil
Pulse Sequence	Multi Slice Multi Echo (MSME)
Matrix Dimension	256
Recovery Time (TR)	250ms
Echo Time (TE)	8.4ms
Field of View (FOV)	4.28cm
Slice Thickness	1.93mm
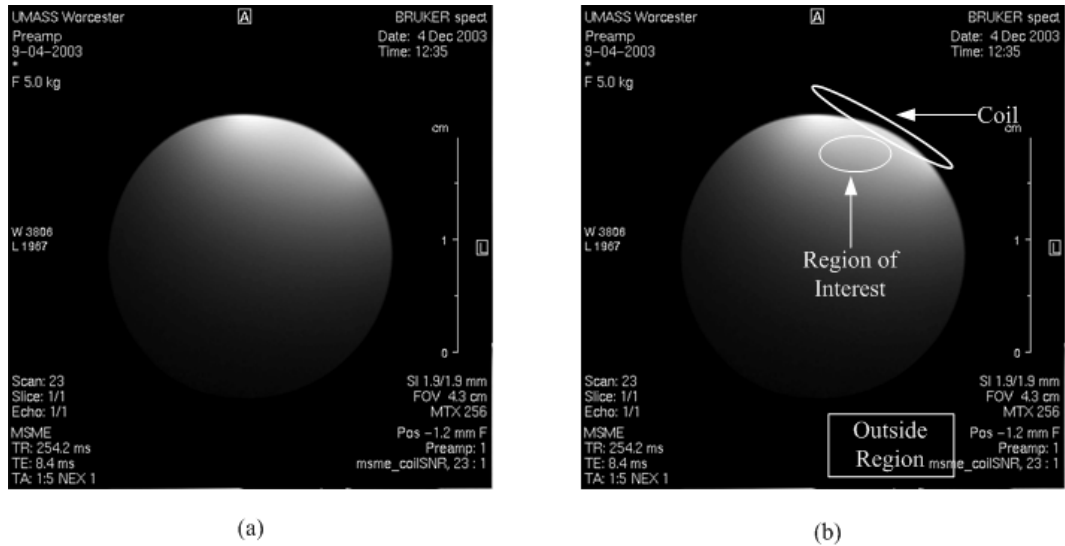
Figure 40. (a) Image acquired during test, (b) same image showing relative position of coil, region of interest and outside region.

The axial slice of the phantom is shown in Figure 40 (a) and (b). The coil was placed over the phantom as shown in Figure 40 (b). The image is slightly tilted due to a small inaccuracy in alignment of the coil in the magnet. The intensity is best in the region where the coil is closest to the phantom. This can be explained by the principle of reciprocity – if we consider a magnetic field generated by a loop of wire carrying an alternating current at Larmor frequency [14]. The magnetic field is stronger close to the loop and it weakens as we move further away from the coil. In a similar manner, if a voltage is induced in the same coil by the precessing nuclei, the induced voltage is stronger if the nuclei are closer to the coil. Therefore, in our case, the signal received by the coil decreases as the distance between the phantom and the coil increases. This causes the intensity of the image to decrease as the distance between the coil and the phantom increases.

Among MRI researchers, SNR generally indicates the quality of an image. SNR in MRI is measured by calculating the ratio of the signal intensity in a sub-region within the ROI to the background noise. The imaging software was used to obtain the signal intensity of

58

the ROI and the background noise indicated by the outside region in Figure 40. The SNR is then calculated as the ratio of the signal intensity of the region of interest to the signal intensity of the outside region. The SNR is given in the Table 2.

Table 2. SNR results of the surface coil for the phantom image in Figure 40.

Signal	Noise	SNR
1.07×10^6	5.9×10^3	181.3

The coil and the interface unit performed well. The quality of the image shown in Figure 40 is quite acceptable and the SNR of the coil is higher than the coils currently in use by CCNI, which yield a SNR of approximately 150

7 Preamplifier

7.1 Preamplifier in NMR Phased Array

Low noise preamplifiers (LNA) can be employed in NMR phased array system to eliminate the interference between coils. Coils using special preamplifiers behave independently, although they are all simultaneously operational when receiving NMR signals. Specially designed preamplifiers employ networks that present a high input reflection coefficient, while simultaneously maintaining a low noise match. Figure 41 is a block diagram to demonstrate the decoupling concept using a high input reflection coefficient preamplifier.
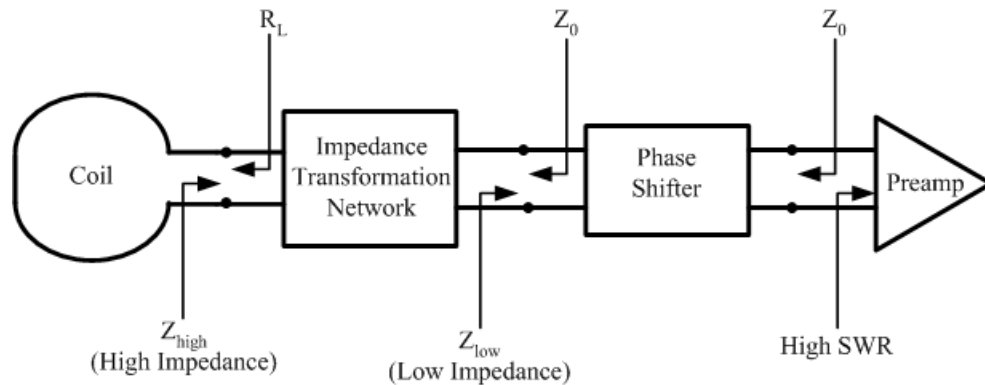
Figure 41. Diagram to demonstrate the high input reflection coefficient preamplifier decoupling concept.

The preamplifier in the system shown in Figure 41 is used for decoupling coils. The impedance transformation network in this system is needed to transform R_L into Z_0 to achieve a low noise match looking in the direction from the preamp to the coil and transform the preamplifier input impedance Z_{low} into a high impedance Z_{high} in the reverse direction to help minimize the current in the coils. A network is needed between the impedance transformation network and the preamplifier to transform the preamplifier input impedance into a low real impedance Z_{low} (the input impedance of the preamplifier as seen by the impedance transformation network) looking in the direction from the coil to the preamplifier, while not modifying the impedance seen by the preamplifier in the direction of the coil. This is addressed by employing a phase shifter. It is important to note that impedance Z_0 is the source impedance seen by the preamplifier and this is not equal to its input impedance. This is necessary for decoupling purposes, hence the need for a high input reflection coefficient.

Using a phase shifter network is also advantageous in designing the preamplifier. It relaxes the preamplifier design constraint by not imposing any low input impedance restriction and concerning us with only the high input reflection coefficient restriction. The phase shifter is generally a coaxial cable and its S-parameters are given in equation (45) where $\beta = \omega\sqrt{LC}$, where L is the inductance per unit length of the cable, C is the capacitance per unit length of the cable and l is the length of the cable [11].

$$S = \begin{pmatrix} e^{-j\beta l} & 0 \\ 0 & e^{-j\beta l} \end{pmatrix} \tag{45}$$

Therefore to summarize, a high input reflection coefficient can be utilized to reduce the current flow in the coil. This is done by using lossless impedance transformations to create a high impedance at the coil terminals while simultaneously maintaining a low noise figure for the preamplifier. To further understand this concept let us consider the block diagram given in Figure 41.

The amplifier in Figure 41 is assumed to be calibrated so that an optimal noise performance is achieved when connected to source with characteristic impedance Z_0, which is 50Ω in our case. The matching network transforms the coil impedance R_L to Z_0 (50Ω) under the condition of resonance. The phase shifter that follows the matching network will not change the 50Ω impedance seen by the preamplifier, but will change that phase. In the reverse direction, the phase shifter will transform the preamplifier input impedance to Z_{low} (low impedance). Finally, Z_{low} will be transformed to Z_{high} (high impedance) by the matching network at the coil terminals. This reduces the current flowing in the coil, thus decreasing coupling between the coils.

7.2 Design Considerations

7.2.1 Stability

Stability is of particular concern when dealing with RF circuits, which tend to oscillate depending on the operating frequency and termination [10]. Oscillation in the context of voltage reflection would mean that $|\Gamma_{IN}|>1$ or $|\Gamma_{OUT}|>1$ (where Γ_{IN} is the input reflection coefficient and Γ_{IN} is the output reflection coefficient). Both Γ_{IN} and Γ_{OUT} depend on the source and load matching networks. Therefore, the stability of the preamplifier depends on the source reflection coefficient Γ_S and the load reflection coefficient Γ_L as presented by the matching networks. A figure of merit used to define stability is the Rollett factor

k. A network is said to be unconditionally stable if k>1 and |)|<1. The stability factor [10] is defined as:

$$k = \frac{1 + |\Delta|^2 - |S_{11}|^2 - |S_{22}|^2}{2|S_{21}||S_{12}|} \tag{46}$$

with,

$$\Delta = S_{11}S_{22} - S_{12}S_{21} \tag{47}$$

7.2.2 *Bilateral Matching*

Matching networks are needed in RF amplifiers to reduce undesired reflections and thus improve the power flow conditions. This is usually accomplished by using additional passive networks between source and load. For many practical circuits, matching networks are also based on other constraints such as minimizing noise influence, maximizing power-handling capabilities and linearizing the frequency response. A generic single stage amplifier configuration is shown in Figure 42 [10]. Let us use this configuration as reference to discuss the approach employed in the preamplifier matching circuit.
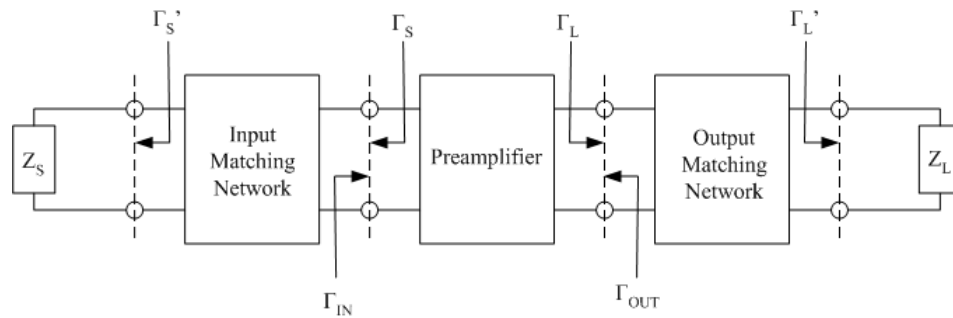
Figure 42. Generic amplifier system.

If the influence of the transistor feedback is neglected, i.e. $S_{12} = 0$, a network is matched by equating: $\Gamma^*_S = S_{11}$ and $\Gamma^*_L = S_{22}$ based on the unilateral design [10]. However, errors are committed by setting $S_{12} = 0$ and this results in an imprecise design. Therefore, for bilateral matching the feedback is taken into account and the input and output reflection coefficients are simultaneously found according to

$$\Gamma^*_{MS} = S_{11} + \frac{S_{12}S_{21}\Gamma_{ML}}{1 - S_{22}\Gamma_{ML}} \tag{48}$$

$$\Gamma^*_{ML} = S_{22} + \frac{S_{12}S_{21}\Gamma_{MS}}{1 - S_{11}\Gamma_{MS}} \tag{49}$$

where

$$\Gamma_{MS} = \frac{B_1}{2C_1} - \sqrt{\left(\frac{B_1}{C_1}\right)^2 - 4\frac{C^*_1}{C_1}} \tag{50}$$

$$\Gamma_{ML} = \frac{B_2}{2C_2} - \sqrt{\left(\frac{B_2}{C_2}\right)^2 - 4\frac{C^*_2}{C_2}} \tag{51}$$

here:

$$B_1 = 1 - |S_{22}|^2 - |\Delta|^2 + |S_{11}|^2 \tag{52}$$

$$B_2 = 1 - |S_{11}|^2 - |\Delta|^2 + |S_{22}|^2 \tag{53}$$

$$C_1 = S_{11} - S^*_{22}\Delta \tag{54}$$

$$C_2 = S_{22} - S^*_{11}\Delta \tag{55}$$

Finally, after finding the values, the matching circuits are used to match the input and output impedances to the conjugate input and output reflection coefficients; i.e. Z_S is matched to the impedance corresponding to Γ^*_{MS} and Z_L is matched to the impedance corresponding to Γ^*_{ML}.

7.2.3 Low Noise Matching

The need for signal amplification at a low noise level is an essential system requirement.

A design for a low noise level amplifier competes with factors such as stability and gain.

It is not possible to obtain a minimum noise performance at maximum gain.

A method to satisfy the requirement of minimum noise at an appropriate gain is to match

the source to the minimum noise figure. In this method Γ^*_S would be equal to the

minimum noise figure Γ_{IN} and Γ^*_L can be found from Γ^*_S, from the following

expression.

$$\Gamma^*_L = \frac{S_{11} - \Gamma^*_S}{\Delta - S_{22}\Gamma^*_S} \tag{56}$$

Equation (56) results in both noise match and a power match at the input, while

sacrificing matching at the output.

7.3 Transistor Selection

The low noise required of the preamplifier typically governs the choice of the topology

and the parameter values that can be employed in the design [12]. This usually means

that only one transistor can be the dominant noise contributor. Therefore, selection of the

appropriate transistor is critically important in designing a preamplifier. The transistor

has to have a small noise figure and it also has to be unconditionally stable. A variety of

transistors were considered for this preamplifier. Agilent Technologies' ATF54143 was

ultimately selected due to its low noise and high dynamic range.

7.4 Generic Preamplifier

There were several design strategies investigated for the preamplifier. Amongst them, a generic design for a low noise preamplifier was considered and eventually constructed. The generic preamplifier was designed with the goal to have a stable performance, a noise figure (NF) of less than 0.5dB, and a gain between 20 and 25dB at 200MHz (a separate preamplifier for 500MHz was also constructed using the same design). A depiction of the generic preamplifier and its test results are shown in Figure 43, Figure 44, and Figure 45. The preamplifier's design and construction are discussed in detail in Appendix B.
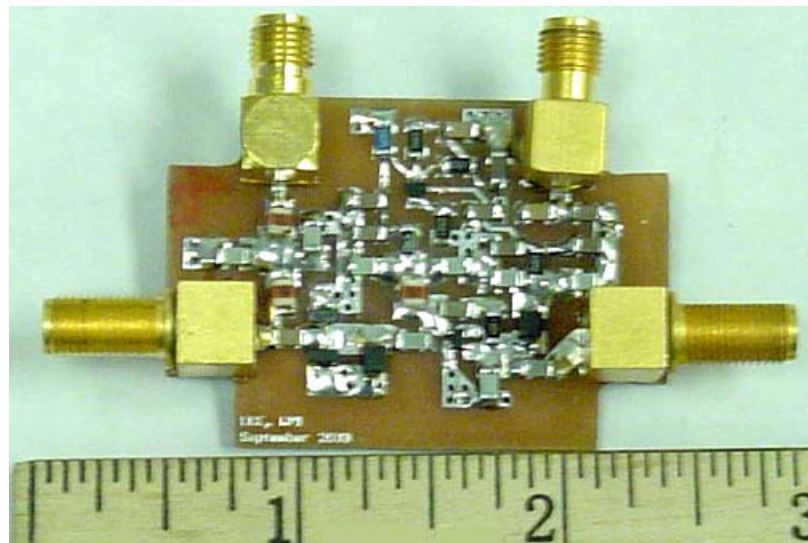
Figure 43. Constructed generic preamplifier.
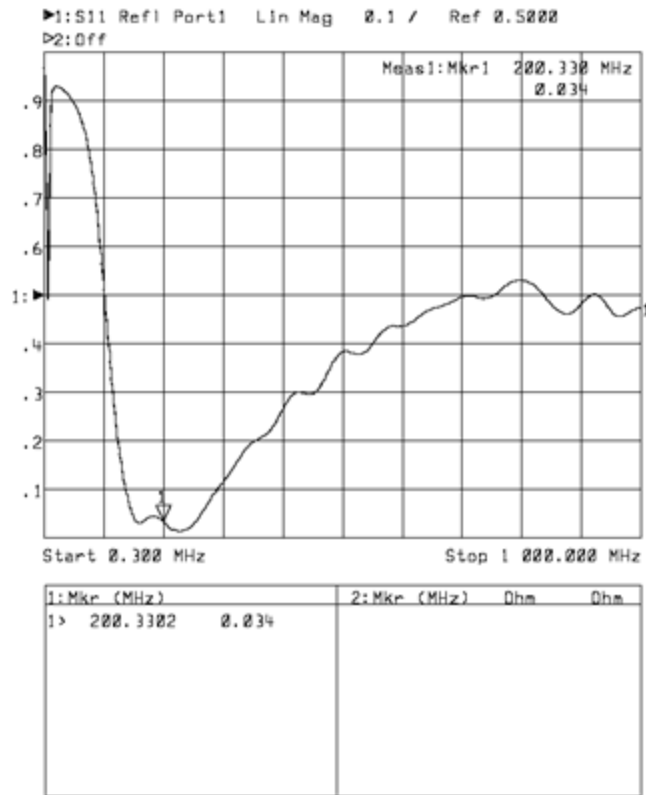
Figure 44. Generic preamplifier test result showing |S₁₁| over the range from 300kHz to 1GHz.
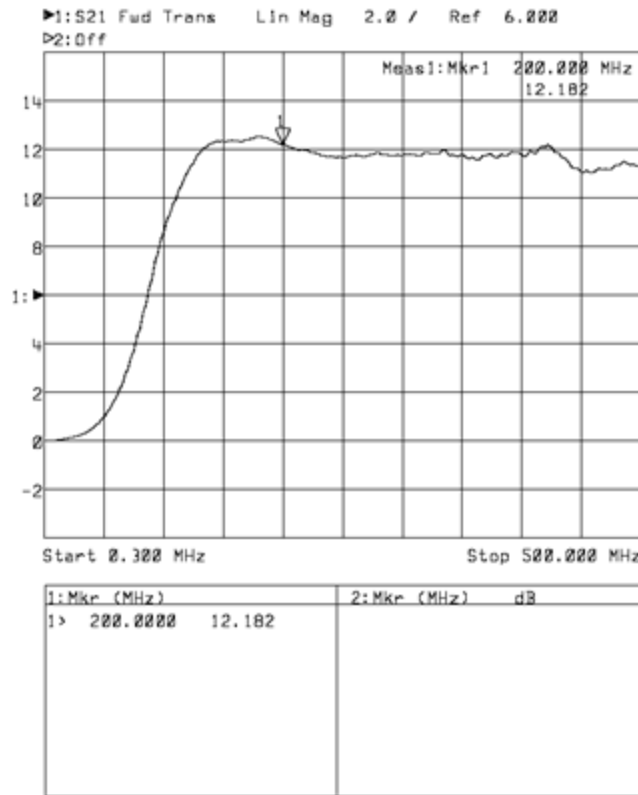
Figure 45. Generic preamplifier test result showing |S$_{21}$| over the range from 300kHz to 500MHz.

The preamplifier was tested and the results showed it performed well. It had an acceptable gain of approximately 2.182 or 22dB as shown in Figure 45. The preamplifier was also tested at CCNI and its performance was tested against an existing preamplifier currently employed at the center. There was about 15% improvement in SNR over the existing preamplifier. These results are discussed in detail in Appendix B.

The generic preamplifier was designed to have a small reflection coefficient to allow for maximum power transfer. In Figure 44, we can see that |S$_{11}$| is approximately 0.034. Clearly, this preamplifier will not be useful in decoupling phased array coils since we need a high reflection coefficient for this purpose. Therefore, another design was considered for the high input reflection coefficient preamplifier. The design and

simulation of the high input reflection coefficient preamplifier is discussed in the following sections.

7.5 High Input Reflection Coefficient Preamplifier Design and Simulation

In this section we will discuss the design for a high input reflection coefficient preamplifier tuned to 500MHz resonant frequency. This is due to the fact that it will eventually be used in an 11.7T MRI system.   The design specifications for this preamplifier were similar to the ones for the generic preamplifier.   The preamplifier would need to have a stable performance, a low noise figure and a gain greater than 20dB. It also has to have a high reflection coefficient.

Although, a number of the design procedures were the same as in the previous design, there were minor improvements that we made in areas such as the transistor biasing. In the previous preamplifier we had used a BJT in the biasing network. However, for this high reflection coefficient design operational amplifiers were used to replace them. This helped in reducing the number of components in the biasing circuit. Also, the stability network was redesigned and an additional stage was added to boost the preamplifier gain. In the generic preamplifier design, a feedback network depicted in Figure 46 was used to stabilize the transistor. However, this stabilization technique lowers the input reflection coefficient of the preamplifier. Therefore, another method was needed to stabilize the transistor.
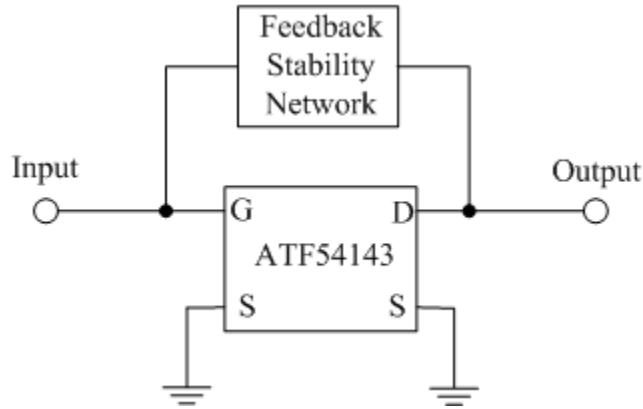
Figure 46. Feedback stability network.

A different method to achieve transistor stabilization is to add a series resistance or shunt conductance to a port. For this transistor, a Pi-network attenuator was employed as a stabilizing network that is shown in Figure 47. The Pi-network is designed to stabilize the network with minimum attenuation. The stabilizing network is placed on the output port of the transistor. The output port was selected, since adding a resistor at the input port causes additional noise to be amplified.
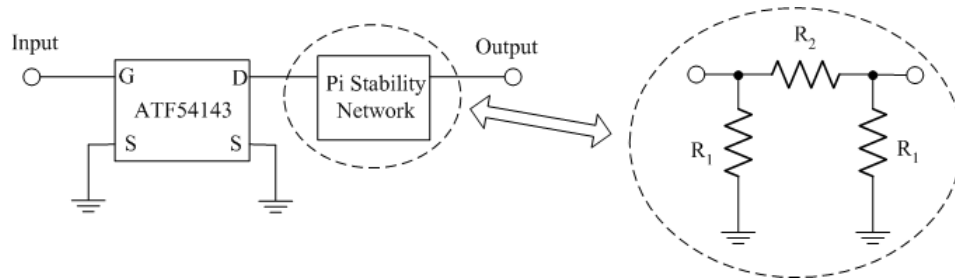
Figure 47. Pi attenuator deployment at the output port.

Resistors R_1 and R_2 are calculated from the following expressions:

$$R_1 = Z_0 \frac{k+1}{k-1} \qquad (57)$$

$$R_2 = \frac{Z_0}{2}\left(\frac{k^2-1}{k}\right) \qquad (58)$$

where k is the attenuation factor which is defined as :

70

$$k = \frac{1}{S_{21}} \qquad (59)$$

The Pi-network, shown in Figure 47, was designed after analyzing the stability circles of the transistor. A program was written in MATLAB to plot the output stability circle on a ZY Smith Chart by using the following expressions.

$$C_{out} = \frac{\left(S_{22} - S^*_{11}\Delta\right)^*}{\left|S_{22}\right|^2 - \left|\Delta\right|^2} \qquad (60)$$

$$r_{out} = \frac{\left(S_{12}S_{21}\right)}{\left|\left|S_{22}\right|^2 - \left|\Delta\right|^2\right|} \qquad (61)$$

where C_{out} is the center of the circle, and r_{out} is the circle radius.

The distance, d, between the origin of the Smith Chart and C_{out} was also calculated using the program. For minimum attenuation, the load reflection coefficient Γ_L was centered at the origin with the magnitude r_L (here $r_L = d - r_{out}$). The Pi-network components were calculated by using the relationship between k and r_L as shown in equation (62). The result of the program is presented in Figure 48.

$$r_L = \frac{1}{k^2} \qquad (62)$$
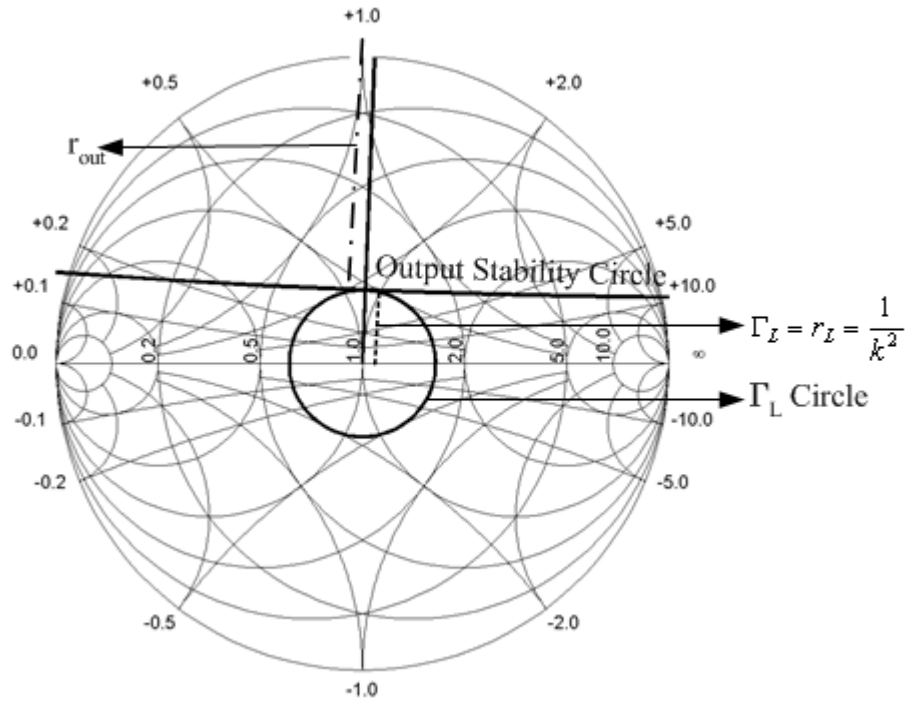
Figure 48. MATLAB program showing the stability results.

The next step in the procedure was the design of the input and output matching networks

that would result in a high input reflection coefficient at the resonant frequency. Figure

49 shows the reference configuration diagram used to design the matching networks.
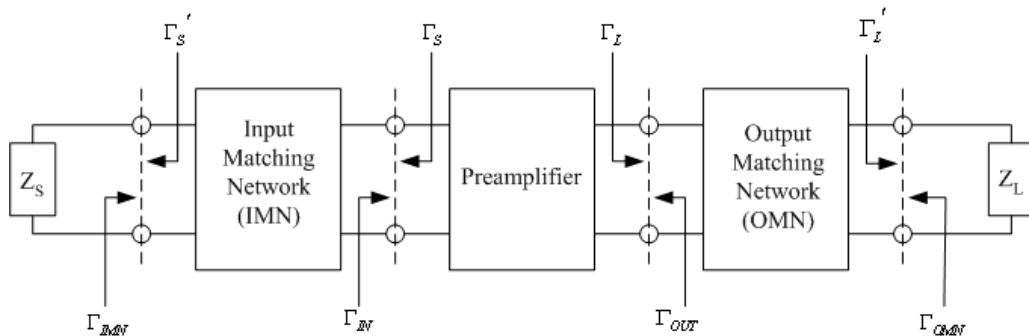
Figure 49. System configuration showing input, output, source, and load reflection coefficients.

In Figure 49, $\ni_S$ and $\ni_L$ are the source and load reflection coefficients. Both $\ni_{IN}$ and $\ni_{OUT}$

are the input and the output reflection coefficients of the preamplifier, while $\ni_{IMN}$ and

$\ni_{OMN}$ are the input and output reflection coefficients of the system. The input matching

72

network is needed to match $\ni_S$ to the source impedance. Clearly, $\ni_S$ can be computed from $\ni_{IMN}$ from equations (63) and (64). These equations convert Γ_{IMN} into a circle equation for Γ_S that is centered at C_{IMN} with radius r_{IMN}. Γ_{IN} is the input reflection coefficient of the preamplifier as shown in Figure 49.

$$c_{IMN} = \frac{\left(1 - |\Gamma_{IMN}|^2\right)\Gamma_{IN}^*}{1 - |\Gamma_{IMN}\Gamma_{IN}|^2} \tag{63}$$

$$r_{IMN} = \frac{\left(1 - |\Gamma_{IMN}|^2\right)|\Gamma_{IMN}|}{1 - |\Gamma_{IMN}\Gamma_{IN}|^2} \tag{64}$$

This stage of the design was started with the computation of Γ_{IMN}. Since we are designing a high input reflection coefficient preamplifier, the magnitude of Γ_{IMN} must be close to 1, while the impedance Z_{low} shown in Figure 50 is maintained relatively small.
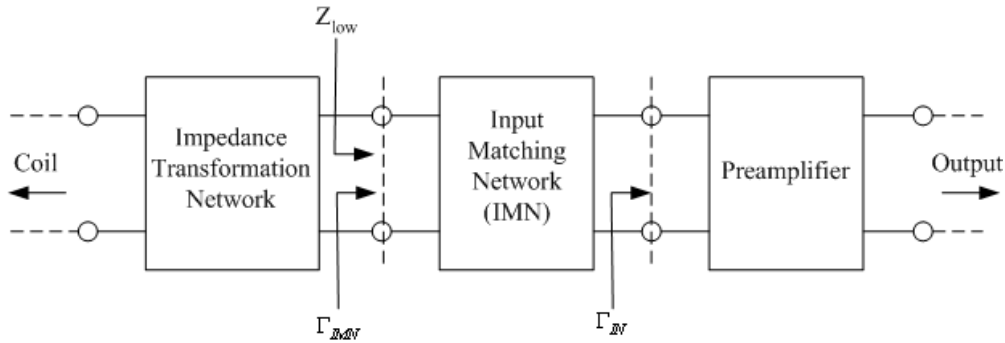
Figure 50. Depiction of Z_{low} and Γ_{IMN}.

The relation between Z_{low} and $|\Gamma_{IMN}|$ is given by equation (65), where $Z_0 = 50\Sigma$, the characteristic impedance of the system. For this design, $|\Gamma_{IMN}|$ was set to 0.96, so Z_{low} would be to equal 1Ω.

$$|\Gamma_{IMN}| = \left|\frac{Z_{low} - Z_0}{Z_{low} + Z_0}\right| \tag{65}$$

The computation of C_{IMN} and r_{IMN} is completed after determining Γ_{IN}. The input reflection coefficient Γ_{IN} is determined from Γ_L according:

$$\Gamma_{IN} = \frac{S_{11} - \Delta\Gamma_L}{1 - S_{22}\Gamma_L} \qquad (66)$$

In equation (66) the values for S_{11} and S_{22} are known from the manufacturers specifications or from the simulations. This leaves Γ_L as the unknown parameter. However, we know that Γ_L is the load reflection coefficient and its magnitude can range from 0 to 1 and its phase can range from 0 to 2B radians. Therefore, values for Γ_L ranging from $0\angle 0\ rad$ to $0.99\angle 2\pi\ rad$ were generated and substituted in equation (66) to determine Γ_{IN}. The computed values of Γ_{IN} were used in equations (63) and (64) to plot Γ_S points on a ZY Smith Chart. These procedures were accomplished by using a program written in MATLAB. An example of certain Γ_S and Γ_L values generated by the program are shown *Table 3*.

Table 3. Table showing sample of Γ_L and Γ_S generated by MATLAB program.

Γ_L	Γ_S	NF	Gain	Noise Measure
0	0.84π6.12°	1.097	25.254	0.101
0.05π-10.44°	0.85π6.10°	1.097	25.013	0.102
0.64π-174.59°	0.84π5.70°	1.098	24.651	0.102
0.07π-13.21°	0.86π10.59°	1.098	24.526	0.102
0.049π-4.78°	0.86π10.465°	1.098	24.037	0.103

The noise figure (NF), gain, and noise measure in Table 3 were parameters subsequently used to select Γ_S. The Γ_S value with the minimum noise figure, maximum gain, and

minimum noise measure was selected for matching. Noise measure NM is a defined as a combination of noise figure and gain as a basis of an overall noise performance comparison. It is given by [10]:

$$NM = \frac{(F-1)}{1-1/G} \tag{67}$$

where F is the noise figure and G is the amplifier gain.

In addition to the selection criteria, it is also advantageous to select Γ_S such that Γ_L is at the origin of the Smith Chart whenever possible. A load matching network is not required during such instances. The input matching network was then designed after selecting Γ_S. The selected Γ_S and Γ_L are $0.84\pi 6.12°$ and 0 respectively.
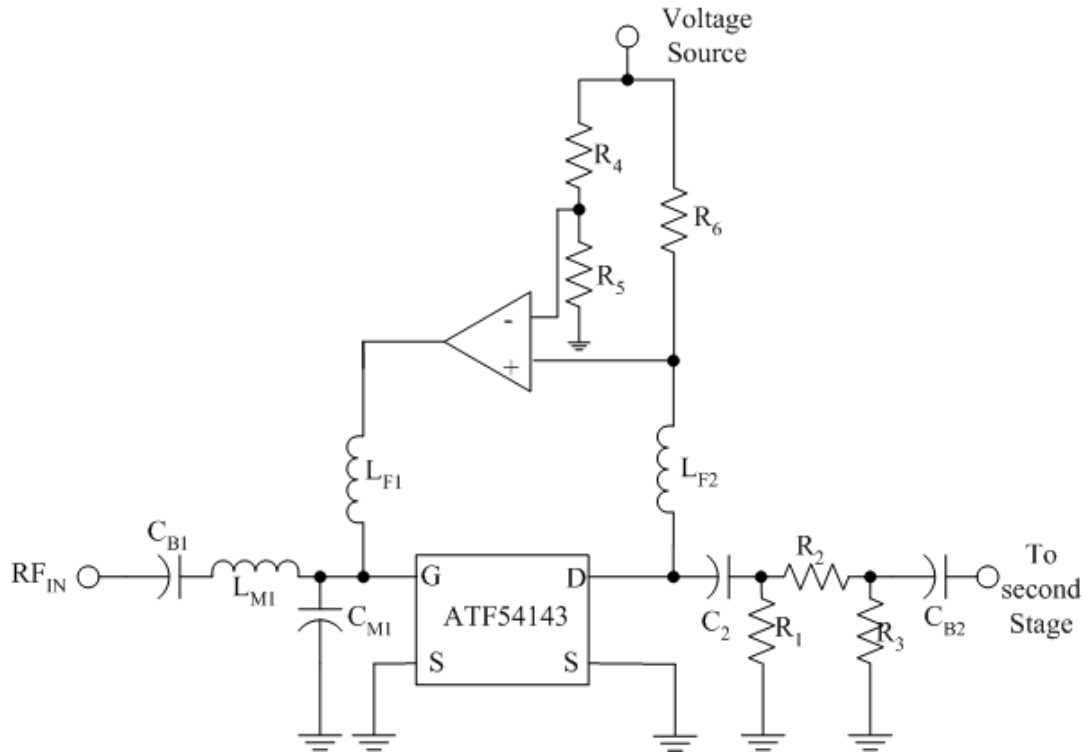
Figure 51. High reflection coefficient preamplifier first stage.

In Figure 51 the resistors R_4, R_5, and R_6 are part of the biasing network. The transistor biasing voltage and current were selecting by referring to the data sheets. A biasing drain

voltage of 3V and drain current of 10mA produced a high reflection coefficient. Resistors R_1, R_2 and R_3 are part of the Pi stabilizing network. Capacitor C_{M1} and inductor L_{M1} are the input matching network components. Capacitor C_{B1} and C_{B2} are DC blocking capacitor and inductors L_{F2} and L_{F2} are a DC feed inductors. This stage was simulated to investigate it performance. The component values used for the simulation are given in Table 4. The input reflection coefficient, gain and noise figure are shown in Figure 52.

Table 4. Component values used for simulation at 500MHz.

Components	Values		Components	Values
L_{M1}	51.97nH		R_3	146Ω
C_{M1}	1.44pF		R_4	2000Ω
R_1	146Ω		R_5	3000Ω
R_2	39Ω		R_6	200Ω
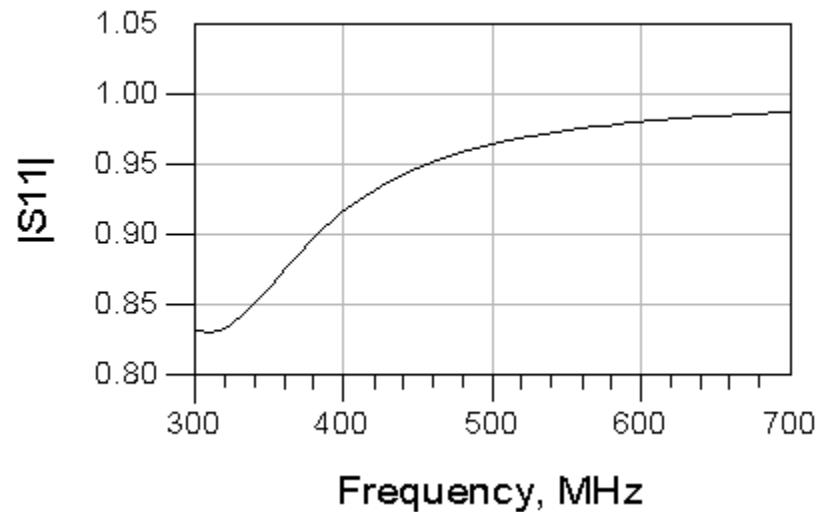
Figure 52. Magnitude response of S_{11} for high reflection coefficient preamplifier from 300MHz to 700MHz.
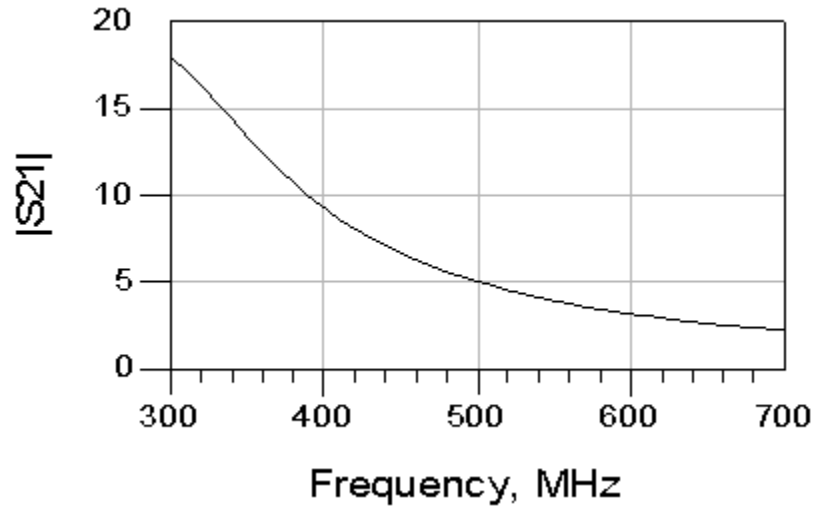
Figure 53. Magnitude response of S_{21} for high reflection coefficient preamplifier from 300MHz to 700MHz.

.
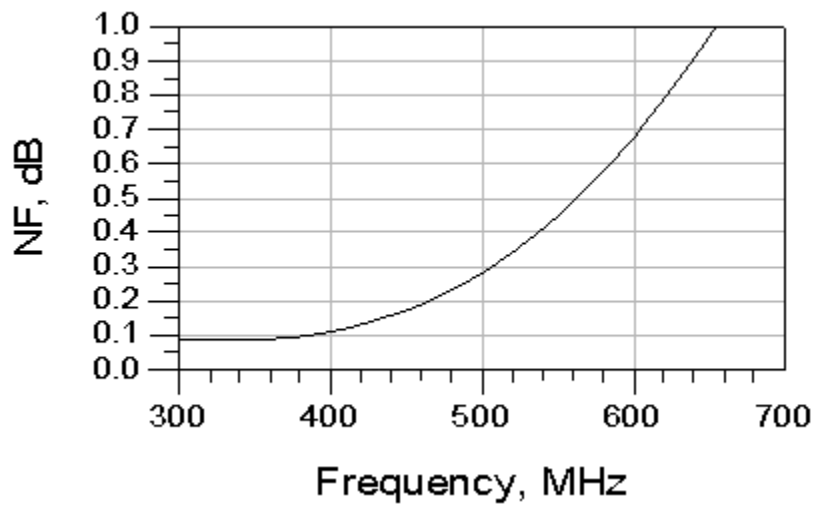
Figure 54. Noise figure for high reflection coefficient preamplifier from 300MHz to 700MHz.

From the simulation results in Figure 52, Figure 53, and Figure 54, we can see that the first stage design at 500MHz has a high reflection coefficient with a magnitude of 0.96 given in Figure 52. The gain and NF are given in Figure 53 and Figure 54. We obtain a gain with a magnitude of 5.03 (14dB) and a NF equal to 0.28dB.

With the completion of the first stage, let us now start the design process for the second stage. The second stage is needed to increase the overall gain of the preamplifier. To design a two-stage preamplifier, the stability of the individual stages and the overall stability must be checked. The configuration of a two-stage preamplifier is shown in Figure 55. Here Γ_{IN1} and Γ_{IN2} are the input reflection coefficients for the first and second stage, while Γ_{OUT1} and Γ_{OUT2} are the output reflection coefficients. And Γ_{ISMN} and Γ_{OSMN} are the input and output reflection coefficients for the intermediate matching network.
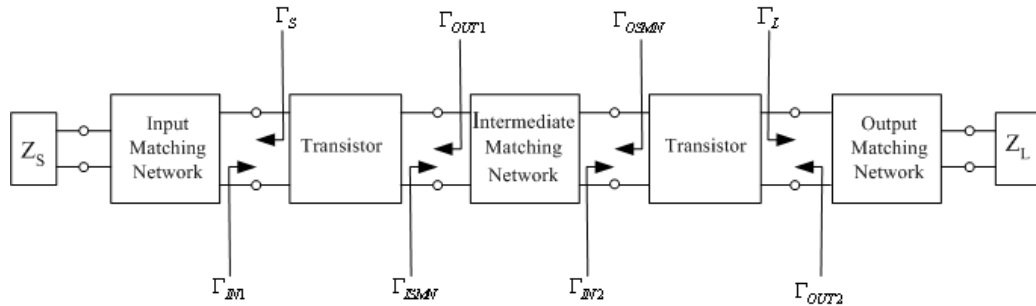
Figure 55. Two stage preamplifier configuration.

For the second stage of the preamplifier, the transistor was stabilized using the feedback network. The input and output matching networks were designed using the bilateral matching technique described in the previous section. The intermediate matching network was designed by matching the source reflection coefficient of the second stage, Γ_{OSMN}, to the output reflection coefficient of the first stage, Γ_{OUT1}. The output matching network was designed by matching the load reflection coefficient Γ_L to the load. One must remember that since we are using bilateral matching technique, Γ_{OUT1} and Γ_L are calculated from equations (48)-(55). The schematic for the second stage of the preamplifier is shown in Figure 56.
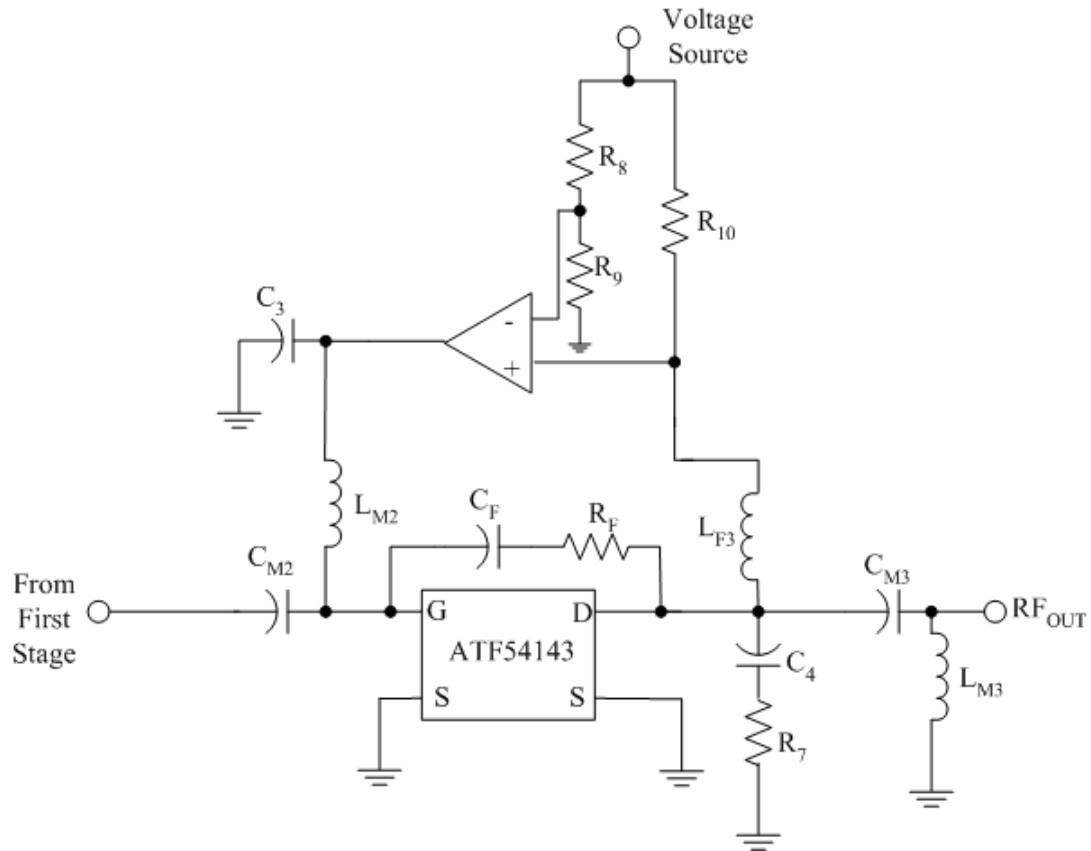
Figure 56. Preamplifier second stage schematic.

In Figure 56 resistor R_F and capacitor C_F make up the feedback network. Capacitor C_{M2} and inductor L_{M2} are the components of the inter-stage matching network. The output matching network is made up of capacitor C_{M3} and inductor L_{M3}.

The two stages were connected and the preamplifier was simulated at 500MHz to see how well it performed. The simulation values for second stage two components are given in Table 5 and the combined schematic for stage 1 and stage 2 are depicted in Figure 57. The simulation results for the two-stage high input reflection preamplifier are given in Figure 58, Figure 59, Figure 60, and Figure 61.

Table 5. Second stage component values used for simulation at 500MHz

Components	Values	Components	Values
L_{M2}	15.9nH	C_3	1000pF
L_{M3}	13.2nH	C_4	2pF
C_{M2}	4.89pF	R_7	70Ω
C_{M3}	31.8pF	R_8	2000Ω
C_F	1000pF	R_9	3000Ω
R_F	1000 Ω	R_{10}	100Ω
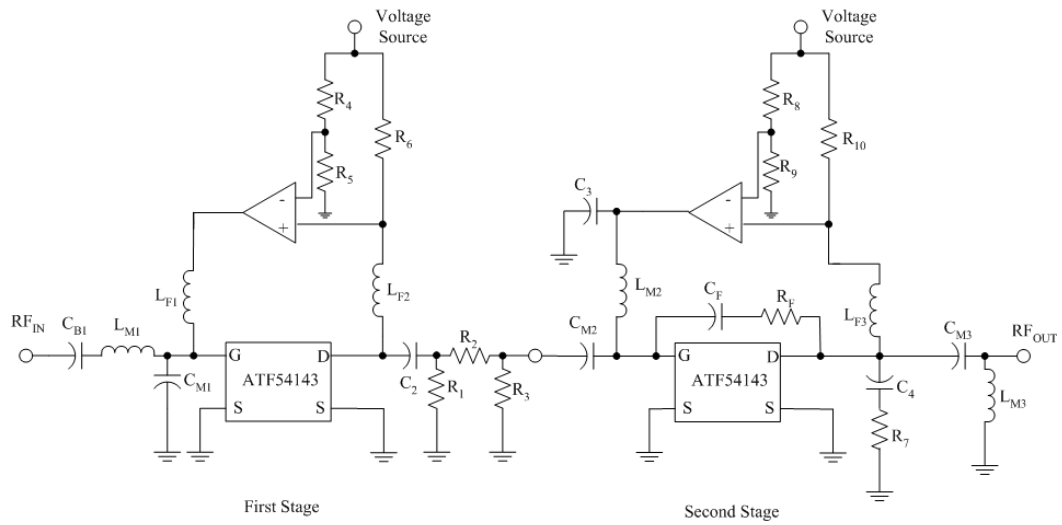
Figure 57. Preamplifier schematic with first and second stage.
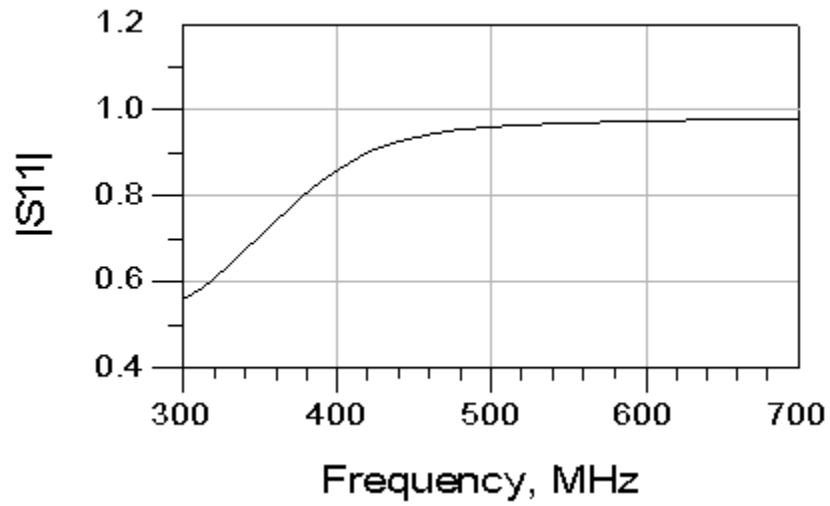
Figure 58. Magnitude response of S_{11} for the two-stage high input reflection coefficient preamplifier from 300MHz to 700MHz.

.
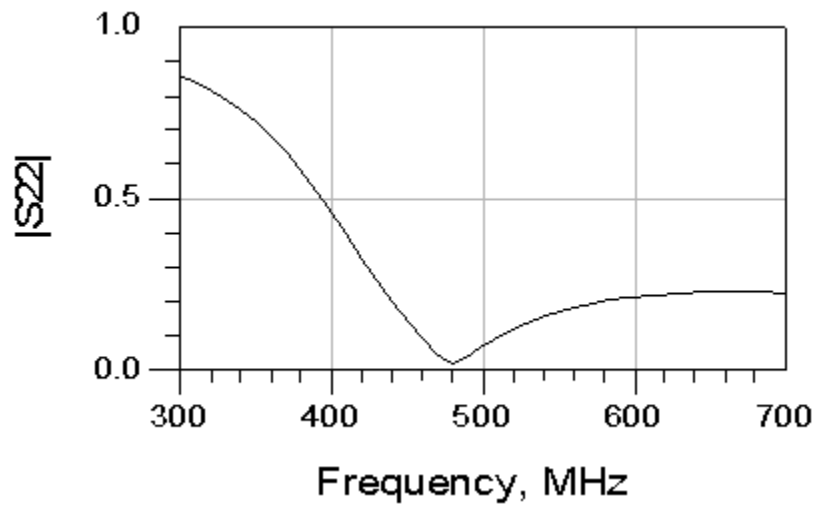
Figure 59. Magnitude response of S_{22} for the two-stage high input reflection coefficient preamplifier from 300MHz to 700MHz.
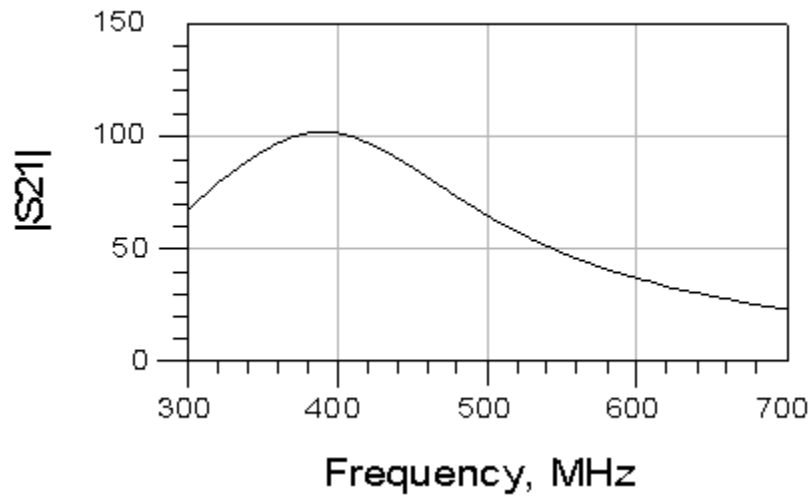
Figure 60. Magnitude response of S_{21} for the two-stage high input reflection coefficient preamplifier from 300MHz to 700MHz.
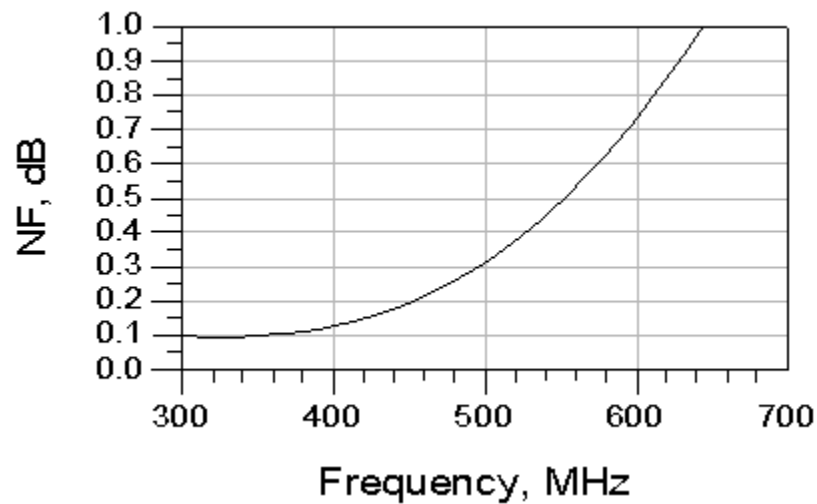
Figure 61. Noise figure for the two-stage high input reflection coefficient preamplifier from 300MHz to 700MHz.

From the simulation results above we can see that the two-stage high input reflection coefficient preamplifier successfully meets the design requirements of a high reflection coefficient (≥ 0.96) and low noise figure ($\leq 0.5\ dB$). At the resonant frequency, it has a high reflection coefficient with a magnitude of 0.961 shown in Figure 58 and a very low S_{22} with a magnitude of 0.069 as shown in Figure 59. The gain and the NF are shown in

Figure 60, and Figure 61. We obtain a gain with a magnitude of 64.731 or 36dB with a

NF 0.313dB.

To check the accuracy of the total NF of 0.313 dB according to the simulations, we

computed the total NF as developed in equation (68) and where the NF of the second

stage according to the simulation was recorded to be approximately 0.73dB.

$$NF = NF_1 + \frac{NF_2 - 1}{G_1} = 1.06 + \frac{1.18 - 1}{25.12} \approx 1.07 \qquad (68)$$

Here NF1 and NF2 are the noise figures of the first and second stage respectively and G_1

is the gain of the first stage. The result in equation (68) is approximately 1.07 or 0.29dB.

It is not exactly 0.313dB because of rounding of errors in the calculation. However, the

result in equation (68) shows that a NF of 0.313dB is correct.

8 Conclusion

8.1 *Summary*

A novel modeling and designing method for decoupling RF surface coils in a phased array coil has been studied. The decoupling process involves the use of an interface circuit and a preamplifier unit. In this thesis, we discuss the theory and the steps that led to the design and development of the interface circuit and the preamplifier unit. The result of this implementation is an interface circuit and a preamplifier unit that can be used in a phased array coil.

The design and the development of the interface circuit and the preamplifier were carried out individually. The development process of the interface circuit and the preamplifier comprised of simulating the design and creating a compact layout. The development was concluded with the successful testing of the coil (the SNR was improved by 20% as mentioned in Chapter 6) and the preamplifier in a 4.7T magnet system. Further research showed that the preamplifier needed to have a high input reflection coefficient. An improvement on the preamplifier led to the successful design simulation of a high input reflection coefficient preamplifier.

8.2 *Further Work*

The surface coil and the high input reflection coefficient preamplifier presented in this thesis are the basic building blocks in a phased array receiver system. Nevertheless, there are some considerations that need to be addressed to further develop these prototype systems. Specific items include:

- Surface coil and interface unit.

  The present impedance transformation network transforms a fixed load impedance to 50Σ. In reality, it is difficult to estimate the impedance of a biological sample. Therefore, future efforts would need to concentrate on adapting the impedance transformation network to varying load impedances.

- Preamplifier.

  The development of the dual stage high input reflection coefficient preamplifier requires further layout construction and testing. The construction process would need to concentrate on designing a highly efficient and compact layout and appropriate shielding.

References

1. Jin, Jianming. Electromagnetic Analysis and Design in Magnetic Resonance Imaging. Boca Raton, Fl: CRC Press LLC; 1989.
2. Hashemy, Ray H. Bradley, WilliamG. MRI-The Basics: Lippincott Williams & Wilkins. 1997.
3. Wehrli, Felix W. Shaw, Derek. Kneeland, J. Bruce. Biomedical Magnetic Resonance Imaging – Principles, Methodology and Applications. New York, VCH Publishers, Inc; 1988.
4. Haacke, Mark E, Brown, Robert W, Thompson Michael R, Venkatesan, Ramesh. Magnetic Resonance Imaging Physical Principles and Sequence Design. New York, NY: John Wiley & Sons; 1999.
5. Kuperman, Vadim. Magnetic Resonance Imaging: Physical Principles and Applications. San Diego: Academic Press, 2000.
6. R.C. Smith and R.C. Lange. Understanding Magnetic Resonance Imaging. New York: CRC Press, 1998.
7. Schempp, Walter J. Magnetic Resonance Imaging: Mathematical Foundations and Applications. New York, NY: Wiley-Liss, Inc; 1998.
8. Bendall, M.R. Surface Coil Technology in Magnetic Resonance Imaging. Ed C.L. Partain, R.R. Price, J.A. Patton, M.V. Kulkarni, A.E. James, Saunders. Philadelphia, 1988.
9. Vaughan, Thomas J. Haupt, David N. Noa Paul J. Vaughn Michael J. Pohost, Gerald M. "RF Front End for a 4.1 Tesla Clinical NMR Spectrometer', IEEE 1995; 42:1333-1337.
10. Ludwig, R. and Bretchko, P. RF Circuit Design: Theory and Applications. Upper Saddle River, NJ: Prentice-Hall, Inc: 2000.
11. Pozar, David M. Microwave Engineering. 2nd edition. John Wiley & Sons, 1998.
12. Razavi, Behad. RF Microelectronics. Upper Saddle River, NJ: Prentice-Hall, Inc: 1998.
13. Guanglong H, Evalappan SP, Hirte H, Deng Y, Petryakov S, Kuppusamy P, Zweier JL. "Mapping of the B_1 Field Distribution of a Surface Coil Resonator Using EPR Imaging", Magnetic Resonance in Medicine 2002; 48:1057-1062.
14. Chen, C.N. Hoult, D.I. Biomedical Magnetic Resonance Technology. New York, NY. Adam Hilger, 1989.
15. Hayes C E, Roemer P B., "Noise Correlations in Data Simultaneously Acquired from Multiple Surface Coil Arrays", Magnetic Resonance in Medicine 1990; 16:181-191.

16. Liao, Samuel Y. Microwave Circuit Analysis and Amplifier Design. Englewood Cliffs, NJ: Prentice-Hall, Inc: 1987.

17. Collin, Robert E. Foundations of Microwave. New York, NY: IEEE Press: 2000.

18. Gonzalez, Guillermo. Microwave Transistor Amplifiers: Analysis and Design. Englewood Cliffs, NJ: Prentice-Hall, Inc: 1984.

19. Vendelin, George D. Design of Amplifiers and Oscillators by the S-Parameter Method. Canada: John Wiley & Sons, Inc: 1982.

20. Reykowski, Arne. Wright, Steven M. Porter, Jay R. "Design of Matching Networks for Low Noise Preamplifiers", Magnetic Resonance in Medicine 1995; 33:848-852.

21. Lee R F, Giaquinto R O, Hardy C J, "Coupling and Decoupling Theory and Its Application to the MRI Phased Array", Magnetic Resonance in Medicine 2002; 48:203-213.

22. Roemer P B, Hayes C E, Souza S P, Mueller O M, "The NMR Phased Array', Magnetic Resonance in Medicine 1990; 16:192-225.

23. Makarov, Sergey V. Antenna and EM Modelling with Matlab. John Wiley and Sons, Inc: 2002.

24. Lee, Ray F. Giaquinto, Randy O. Hardy Christopher J. "Coupling and Decoupling Theory and Application to the MRI Phased Array", Magnetic Resonance in Medicine 2002; 48: 203-213.

25. Wright, Steven M. " Phased Array Coils in MRS". Department of Electrical Engineering, Texas A&M University.

26. Wright, Steven M. "RF Coil Arrays for Magnetic Resonance Imaging". Engineering in Medicine and Biology. IEEE 1990; 12: 47-48.

27. Hyde, J. Froncisz, W. Jesmanowicz, A. Kneeland, J. B. Grist, T. M. Parallel "Image Acquisition from Noninteracting Local Coils". Journal of Magnetic Resonance. 1986; 70:512.

28. Scott, H. Fusco, V. F. "Circular Wire Loop Antenna With Stepped Wire Diameter". Microwave and Optical Technology Letters. 2002; 34.

29. Black, R.D. Roemer, P.B. Mueller, O.M. " Electronic for a High Temperature Superconducting Receiver System for Magnetic Resonance Microimaging". IEEE Transactions on Biomedical Engineering. 1994. 41; 195-197.

30. Zwart J. A, Leden PJ, Kellman P, Gelderen PV, Duyn JH."Design of a SENSE-Optimized High-Sensitivity MRI Receive Coil for Brain Imaging". Magnetic Resonance in Medicine 2002; 47: 1218-1227.

31. Quick, Herald H. Ladd, Mark E. Zimmermann-Paul, Gesine G. Erhart, Peter. Hoffman, Eugen. Schulthess, Gustav V. Debatin, Jorg F. "Single Loop Coil Concepts for Intravascular Magnetic Resonance Imaging". Magnetic Resonance Imaging in Medicine. 1999; 41:751-758.

32. Zwart J. A., Ledden, P. J., Gelderen, P. Kellman, P. Pang, Y. Chu, R. Duyn J. H. "Optimization Of High Sensitivity MRI Receive Coil For Parallel Human Brain Imaging". IEEE. 2002; 966-969.

33. Greenhouse, H.M. "Design of Planar Rectangular Microelectronic Inductors". IEEE Transactions on Parts, Hybrids, and Packaging. 1974; 101-109.

34. Thompson, Marc T. "Inductance Calculation Techniques – Part II: Approximation and handbook Methods". Power Control and Intelligent Motion. 1999.

35. Dwight, H. B. Electrical Coils and Conductors. New York: McGraw-Hill Book Company, Inc; 1945.

36. Grover, F. W. Inductance Calculations – Working Formulas and Tables. New York: D. Van Nostrand Company, Inc.; 1946

37. Smythe, W. R. Static and Dynamic Electricity. New York: McGraw-Hill Book Company, Inc; 1939.

38. Chi, Chen-Yu. Rebeiz, Gabriel M. " Planar Microwave and Millimeter-Wave Lumped Elements and Coupled-Line Filters Using Micro-Machining Techniques". IEEE Transactions on Microwave Theory and Techniques. 1995. 43; 730-738.

39. Ulaby, Fawwaz T. Fundamentals of Applied Electromagnetics. Upper Saddle River, NJ: Prentice Hall; 1997.

40. Hirota, T. Murguchi, M. "K-Band Frequency Up-Converters Using Reduced-Size Couplers and Dividers". IEEE. 1991. 53-56.

41. Nillson, James W. Electric Circuits. Addison-Wesley Publishing Company, Inc. May 1990.

A - Appendix

A.1 Transistor Biasing

For biasing the ATF-54143, two PNP bipolar transistors are arranged in a current mirror configuration as shown in Figure 62. The transistor was actively biased. The advantage of active biasing is the ability to hold the drain current to source current constant over a wide range of temperature variations.
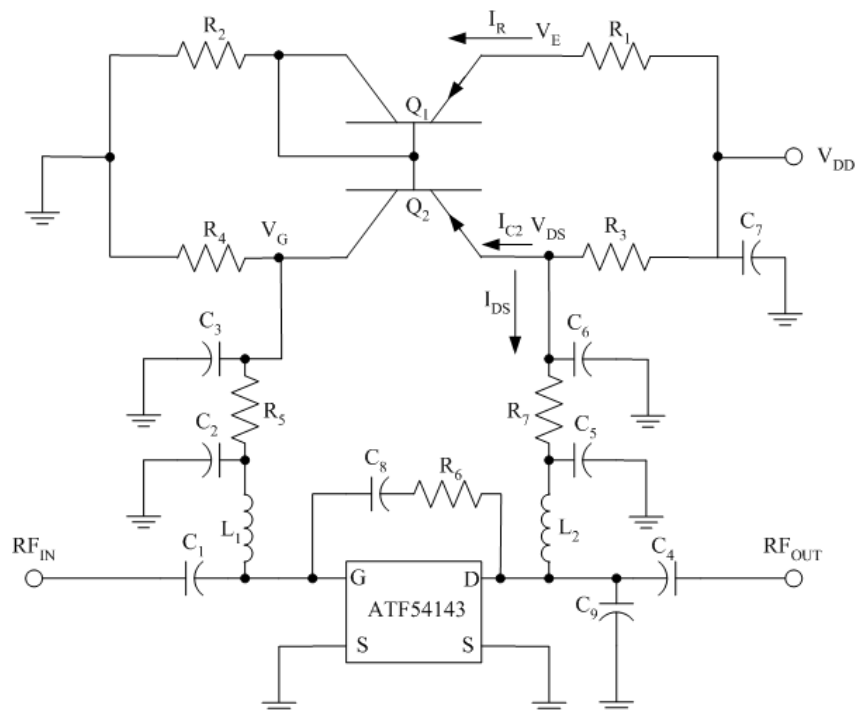
Figure 62. ATF54143 active bias circuit schematic.

Due to R_1 and R_3, the circuit does not act as a true current mirror. If the voltage drop across R_1, and R_3 are kept identical, the current through R_3 is stabilized. As a result I_{DS} and V_{DS} are also kept stable.

I_{DS}, I_R and V_{DD} are first selected to calculate R_1, R_2. R_3, and R_4. The resistors are calculated by the following expressions.

$$R_1 = \frac{V_{DD} - V_{DS}}{I_R} \tag{69}$$

$$R_2 = \frac{V_{DS} - V_{BE1}}{I_R} \tag{70}$$

$$R_3 = \frac{V_{DD} - V_{DS}}{I_{DS} + I_{C2}} \tag{71}$$

$$R_4 = \frac{V_G}{I_{C2}} \tag{72}$$

Capacitors C_2, C_3, C_5, and C_6 provide stability by minimizing the sudden voltage fluctuations and also act as high frequency traps, while resistors R_3 and R_5 provide low frequency stability by providing resistive termination. Capacitor C_9 is a high frequency trap and C_1, L_1, C_4, and L_2 are parts of the input and output impedance matching networks. R_6 and C_8 form a R-C feedback network that stabilizes the network below 2GHz.

A.2 Design

The preamplifier was designed for minimum noise with an input and output impedance of 50Ω. This section will discuss the design for a preamplifier tuned at 200MHz resonant frequency. The same design is used for 500MHz, but with different matching component values. The design schematic is given in Figure 63. The transistor drain current I_{DS}, the reference current I_R and the source voltage V_{DD}

were selected by referring to the data sheets. I_{DS} was selected to be 60mA since it allows for a low noise figure. V_{DD} was selected to be 5V, since commercial regulators are more readily available for this value and I_R was set to 1mA. The values for the biasing components were selected according to these values by using equations (69), (70), (71), and (72) given in Appendix B. Table 6 contains the values for these components for a resonant frequency of 200MHz. Component values for 500MHz resonant frequency are given in Appendix C.
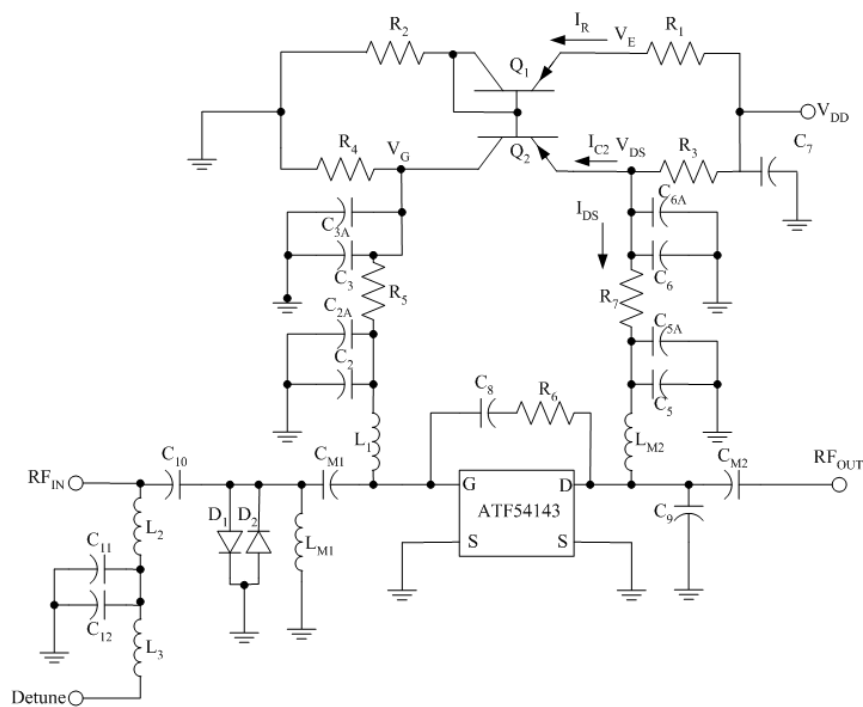
Figure 63. Preamplifier circuit schematic.

Table 6. Component values for preamplifier at 200MHz.

Components	Values	Components	Values
R_1	2000Ω	C_2, C_{2A}	270pF
R_2	2320Ω	C_3, C_{3A}	10nF
R_3	33Ω	C_5, C_{5A}	270pF
R_4	590Ω	C_6, C_{6A}	10nF
R_5	47Ω	C_7	1uF
R_6	1000Ω	C_9	1.8pF
R_7	10Ω	C_{10}, C_{11}, C_{12}	DC Block
		L_2, L_3, L_4	DC Feed

C_2, C_3, C_5, and C_6 are replaced by C_2, C_{2A}, C_3, C_{3A}, C_5, C_{5A}, C_6, and C_{6A}. This was done because by combining capacitors in parallel, their ESR decreases and hence improves the overall quality factor. C_{10}, C_{11}, and C_{12} are DC blocking capacitors, while L_2, L_3 and L_4 are DC feed inductors and D_1 and D_2 are surge protection diodes. The biasing procedure is followed by the matching circuit design and calculations. As stated in Chapter 7, for a low noise design, the input of the preamplifier is matched to the optimum noise. The optimum noise for the transistor was found by simulating the circuit without its matching network. The simulation result is shown in Figure 64.

(a)   (b)
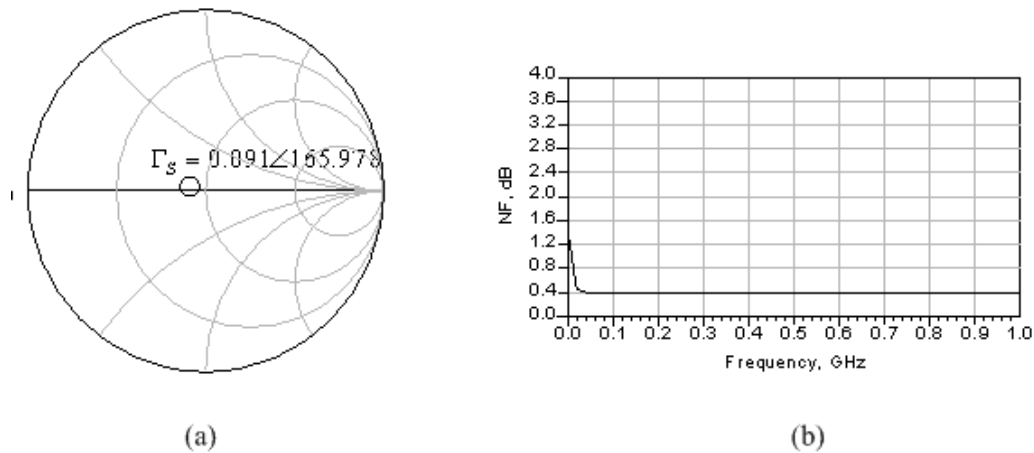
Figure 64. (a) Optimum Noise Figure displayed in the Smith Chart, (b) noise figure versus frequency.

The minimum noise figure was recorded to be 0.39dB at 200MHz with the conjugate minimum noise figure source impedance $Z^*_{\Gamma S} = (41.835 - j1.864)\Omega$ and the source reflection coefficient $\Gamma^*_s = 163\angle - 0.129$. Table 7 shows the S-parameters at 200MHz.

Table 7. S-parameters at 200MHz.

$S_{11} = 0.054 - j0.255$	$S_{21} = -14.202 + j6.57$
$S_{22} = -0.11 + j0.063$	$S_{12} = 0.039 - j5.427 \times 10^{-3}$

The load reflection coefficient was calculated from equation (56).

$$\Gamma_L = \frac{(0.054 - j0.255) - (-163 - j0.129)}{0.602 - (-0.11 + j0.063)(-163 - j0.129)} = 0.345 - j0.048 \qquad (73)$$

To design the matching network, we would also need to know the source impedance. Furthermore, the 50Ω input impedance combines in parallel with the capacitance of the surge protection diodes. Therefore the source impedance is the parallel combination of the diode capacitance and the input impedance. For optimum noise figure matching the noise figure was matched to this source impedance. The diode capacitance was taken from the data sheets to be approximately 4pF. Therefore, the source impedance is:

$$Z_S = \frac{1}{1/50\Omega + j\omega 4pF} = (47.029 - j11.82)\Omega \qquad (74)$$

A program was written in MATLAB to match $Z^*_{\Gamma S}$ to Z_S using the ZY Smith Chart. The result is given in Figure 65.
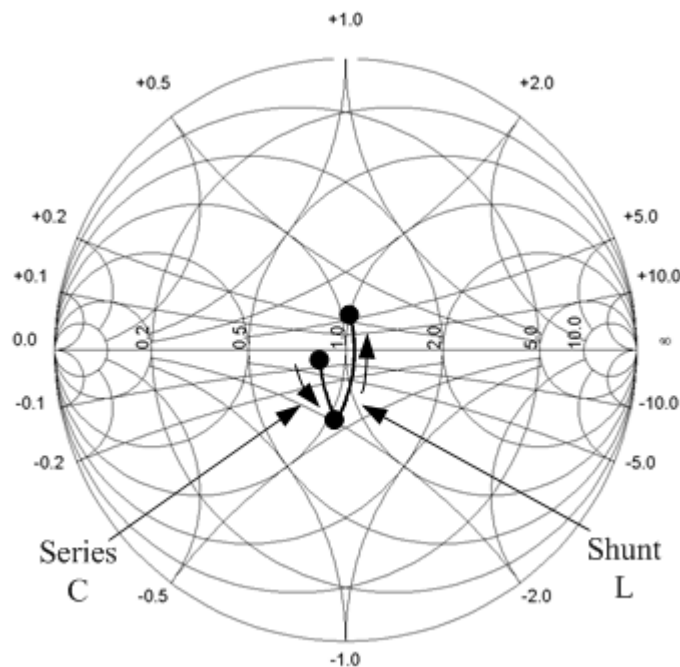
Figure 65. Source optimum noise figure matching displayed in the ZY Smith Chart.

Looking at the source from the transistor, a series C, shunt L topology was used. The values calculated were $C_{M1} = 39.97\,pF$ and $L_{M1} = 57.40nH$. However, we selected commercial component values of $C_{M1} = 47\,pF$.

For the load impedance matching circuit we first need to find $Z^{*}_{\Gamma L}$ and this is matched to a 50Ω impedance. The Smith Chart result is given in Figure 66.

$$Z^{*}_{\Gamma L} = Z_0 \frac{1+\Gamma^{*}_{L}}{1-\Gamma^{*}_{L}} = 50\Omega\frac{1+(0.345+j0.048)}{1-(0.345+j0.048)} = (101.836 - j11.075)\Omega \qquad (75)$$
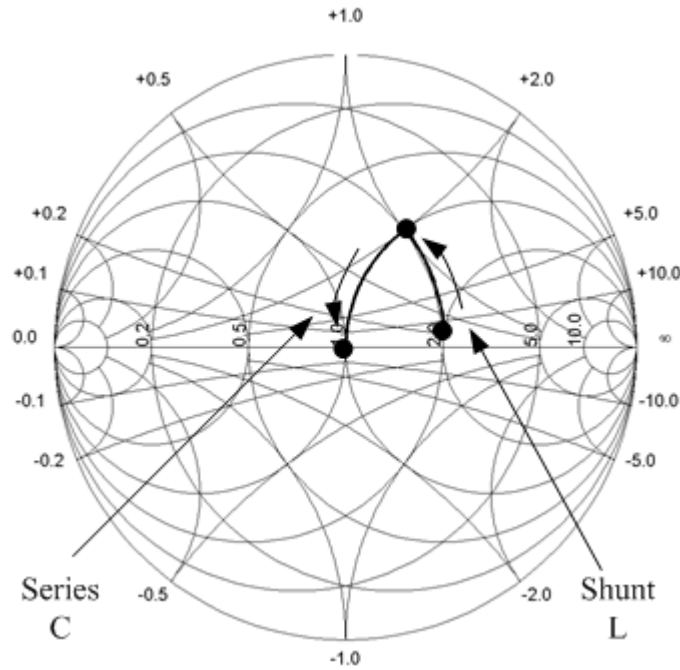
Figure 66. Source impedance matching displayed in the ZY Smith Chart.

Looking at the load from the transistor, a shunt L, series C topology was used. The values calculated were $C_{M2} = 89.10\,pF$ and $L_{M2} = 15.56nH$. Commercial vendor specified values of $C_{M2} = 82\,pF$ and $L_{M2} = 15nH$, were ultimately selected. In this preamplifier design, it is important to note that output is not matched. The input is both noise and impedance matched and we are able to do this because of the bilateral matching techniques and therefore the matching components on the output side of the preamplifier have to be present to this preamplifier to work properly.

A.3 Simulation

After the completion of the biasing and matching designs, the preamplifier design was simulated to see how well it performed. Figure 67 shows the simulation results.
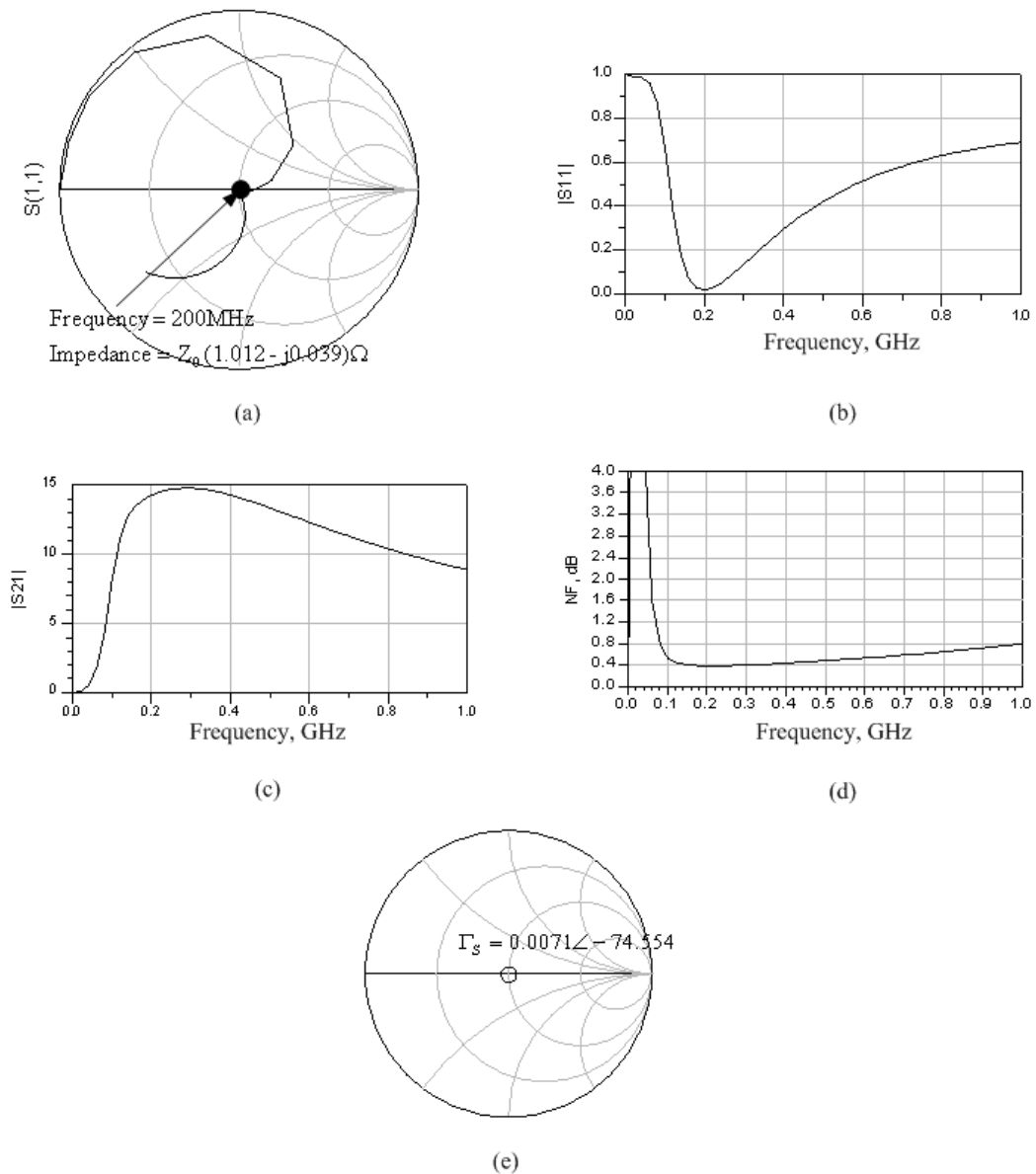
Figure 67. Simulation results - (a) Smith Chart display of S11, (b) magnitude of S11, (c) magnitude of S21, (d) noise figure versus frequency, and (e) noise figure circle.

Figure 67 (a) and (b) are S_{11} plots. From these figure we can see that it is best matched at the design frequency of 200MHz. The magnitude of S_{21} is plotted in Figure 67 (c). It is not maximum at 200MHz, because it is not directly possible to obtain a minimum noise performance at maximum gain. However, an acceptable

compromise was achieved. Figure 67 (d) and (e) show the optimum noise plots. These figures clearly show that the design is matched for minimum noise figure.

A.4 Layout and Construction

Since the preamplifier was designed to be small, it became important to choose components that were physically very small. As the primary component in the preamplifier, the layout was centered on the transistor. The ATF54143 was placed so that the incoming and outgoing RF signals would be lined up in a straight path. Ideally, one would want the input and output to be lined up, with the transistor acting like a bridge between them. This is done to minimize RF signals reflecting off the transmission path. Unfortunately, this was not possible for the layout of this preamplifier as shown in Figure 68 and Figure 69: The output transmission line could not be laid out in a straight path. However, the sharpness of the angle of the path leading to the output was kept to a minimum. The characteristic line impedance of the transmission line also depends on the thickness of the substrate and the width of the transmission line. Equations (76) and (77) are used to calculate the width of the transmission line with a thickness of 0.062 inches using a substrate made of FR-4.
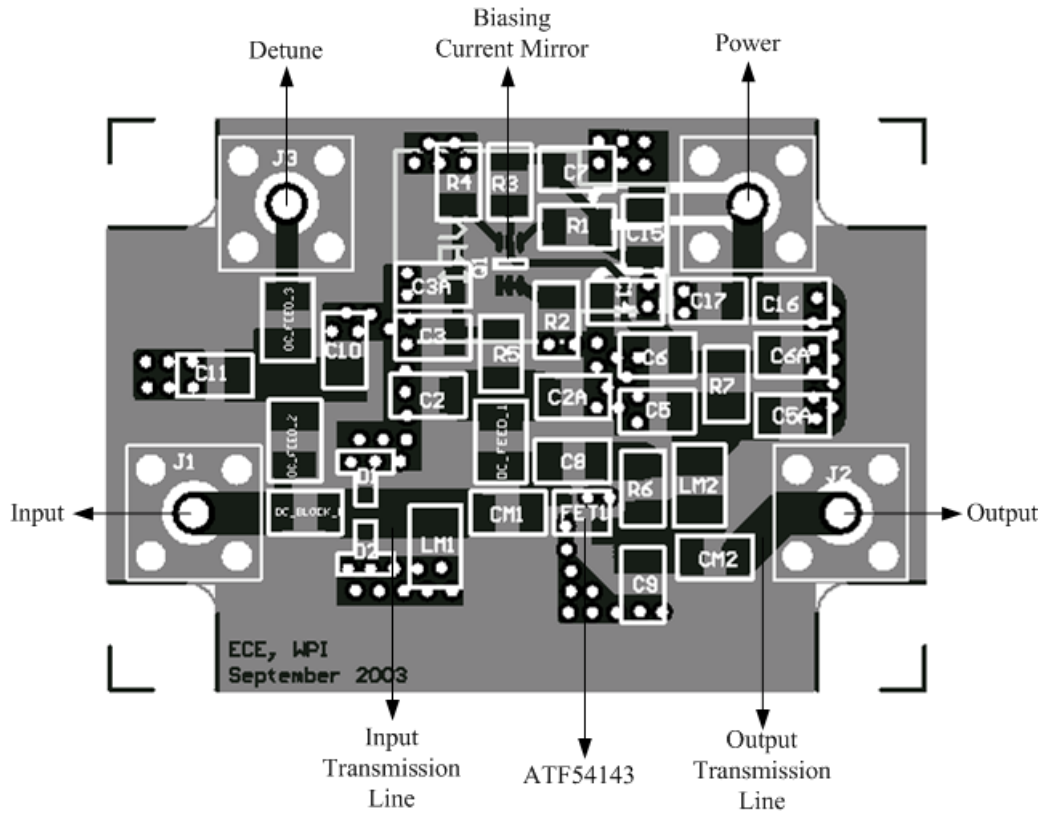
Figure 68. Preamplifier layout – top layer.
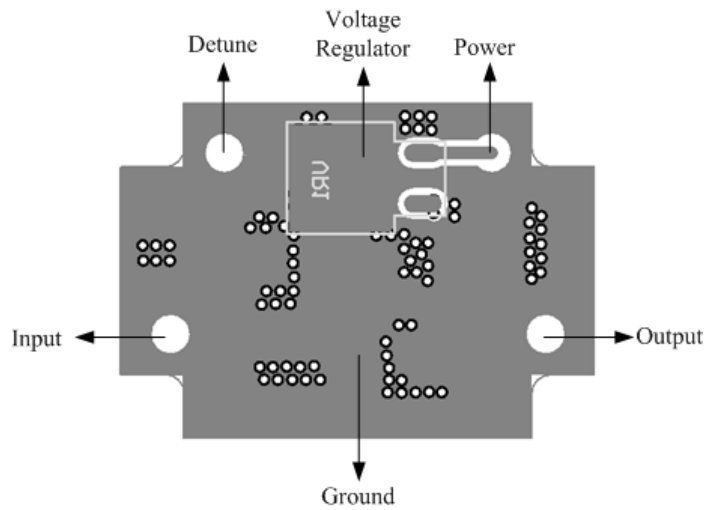
Figure 69. Preamplifier layout - bottom layer.

$$w = h \frac{8e^A}{e^{2A} - 2} \tag{76}$$

$$A = 2\pi \frac{Z_0}{Z_f} \sqrt{\frac{\varepsilon_r + 1}{2} + \frac{\varepsilon_r - 1}{\varepsilon_r + 1} \left(0.23 + \frac{0.11}{\varepsilon_r} \right)} \tag{77}$$

here: $\varepsilon_r = 4.6$ (for FR-4),

$Z_0 = 50\Omega$ and

97

$$Z_f = \sqrt{\mu_0/\varepsilon_0} = 376.8\Omega ,$$

and h is the substrate thickness and w, the width of the trace.

Therefore according to equation (76) and (77), the width of the transmission line is:

$$A = 2\pi \frac{50\Omega}{376.8\Omega} \sqrt{\frac{4.6+1}{2}} + \frac{4.6-1}{4.6+1}\left(0.23+\frac{0.11}{4.6}\right) = 1.558$$

$$w = 0.062in\frac{8e^{1.558}}{e^{2\bullet1.558}-2} = 0.114\,in \tag{78}$$

A transmission line width of 0.114 inches effectively sets the characteristic impedance to 50Ω. The components were placed as closely as possible in order to prevent the inductance of the connecting strips from affecting the total impedance of the circuit. Placing inductors in parallel to one another was also avoided. The voltage regulator and the RF ground were placed on the bottom layer. Placing the voltage regulator on the bottom layer helped in keeping the layout tight and small. The components were connected to the ground by vias. SMA connectors were used for the input, output, detuning, and the power ports.

The construction procedure was fairly straightforward. All the components were soldered to the substrate. Soldering the transistors, both ATF54143 and the current mirror, were difficult due to their small size. The finished products are shown in Figure 70 and Figure 71.
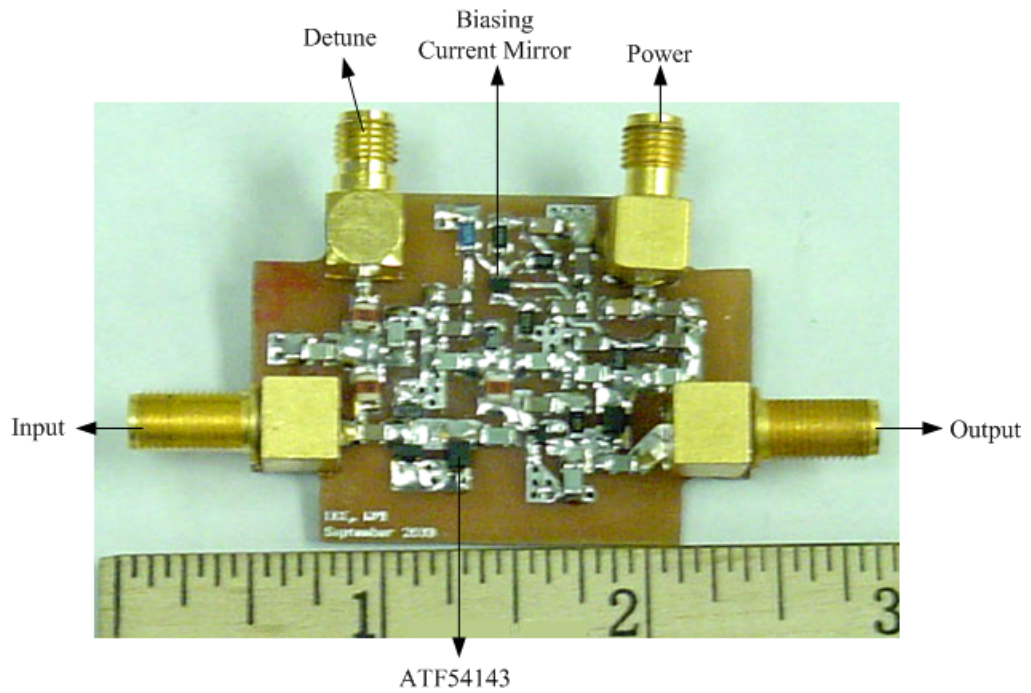
Figure 70. Preamplifier - top layer view.
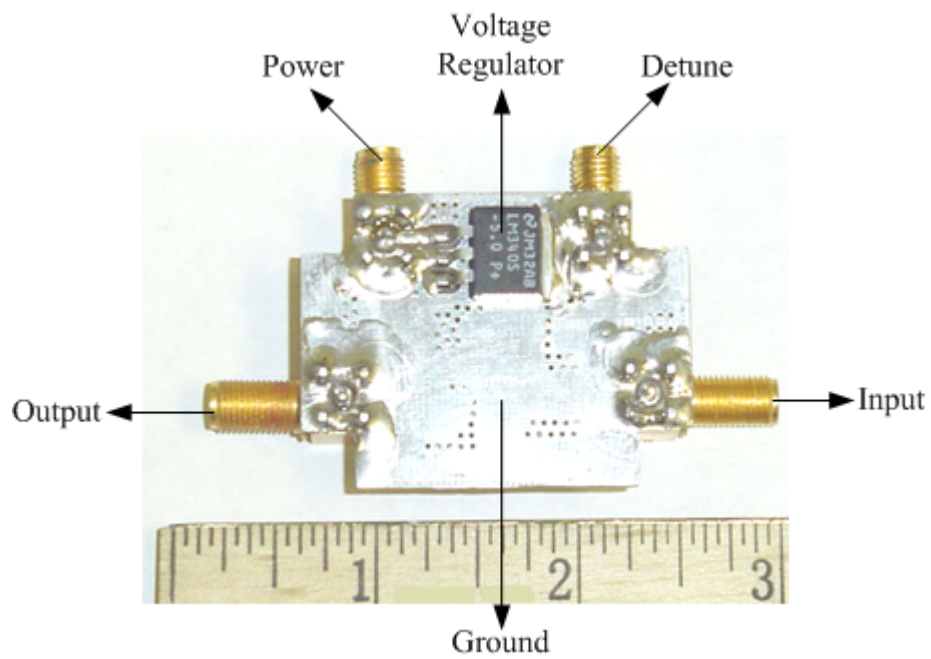
Figure 71. Preamplifier - bottom layer view.

A.5 Testing results

After construction, the preamplifier was tested with a network analyzer. The results are shown in Figure 72 and Figure 73.
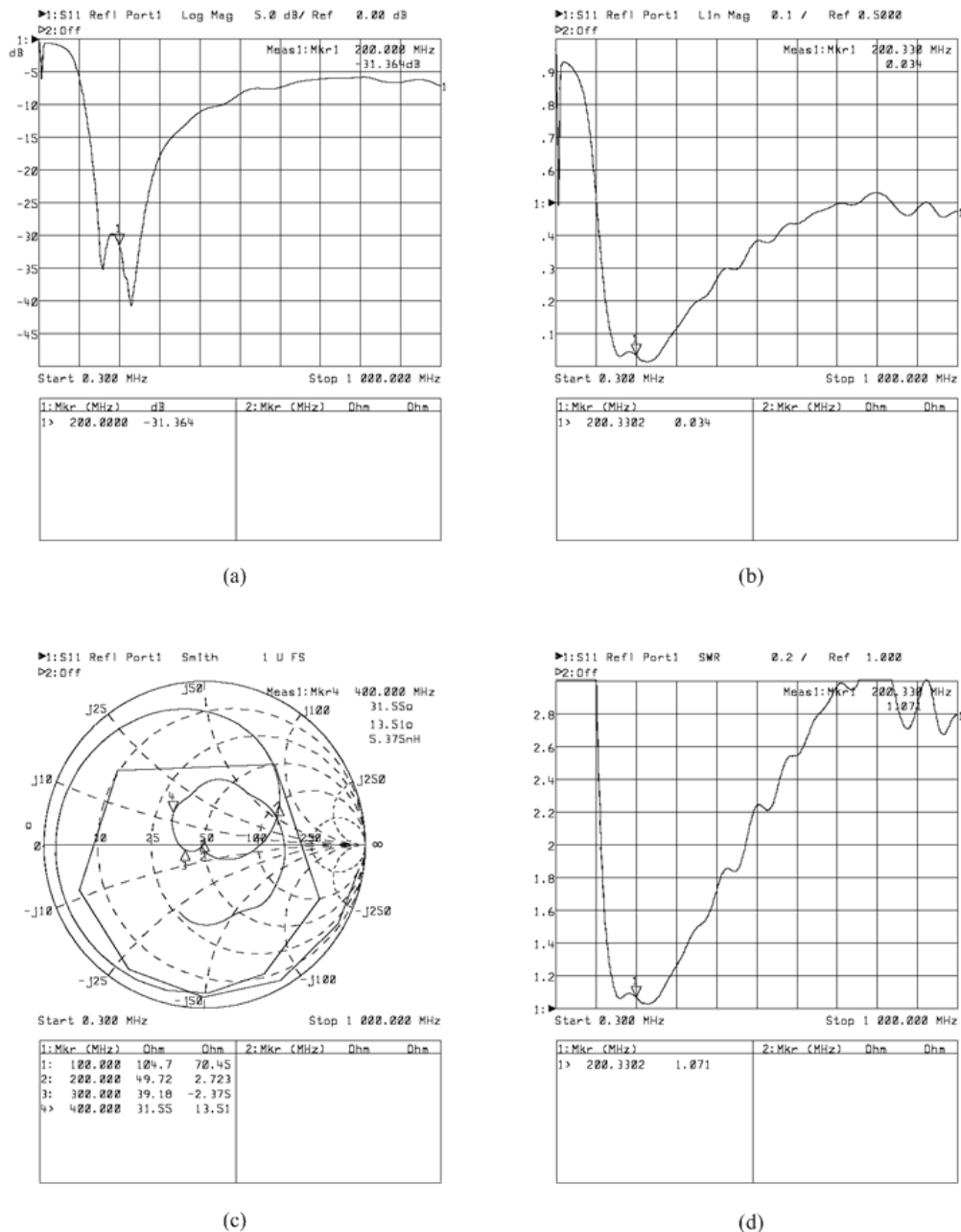
Figure 72. S11 network analyzer results - (a) S11 in dB scale, (b) S11 in linear magnitude scale, (c) S11 displayed in the Smith Chart, and (d) S11 Standing wave ratio.
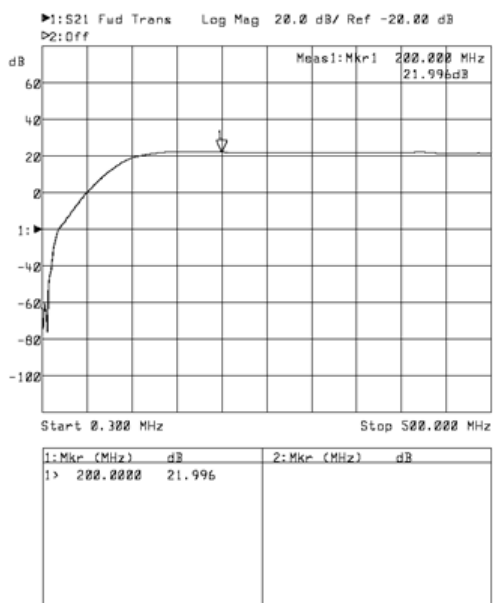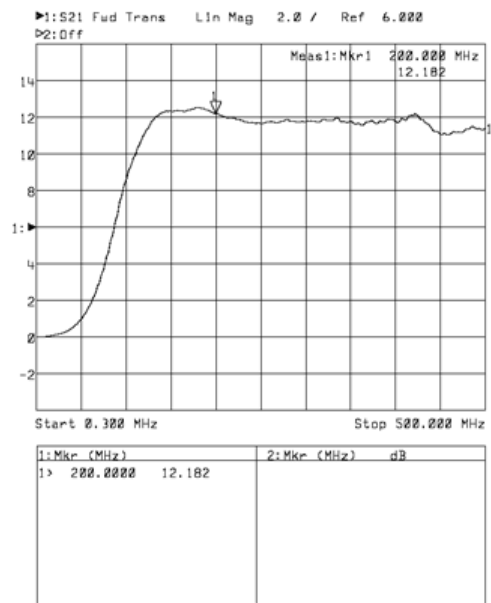
Figure 73. S21 network analyzer results (a) S21 in dB scale and (b) S21 in linear magnitude scale.

According to Figure 72 (a) and (b), $S_{11} = -36.7198dB$ at 200MHz. It is not a perfect resonance point, but still acceptable. This is expected since it is not possible to duplicate theoretical results in real life. Figure 72 (c) shows the S_{21} value, which is about 21dB and meets the design requirement.

The preamplifier was also tested at CCNI. The goal of this experiment was to compare how well it performed against the existing preamplifier by comparing the SNR of the coils. A traditional designed surface coil was used to acquire images of a phantom of mineral oil. This was first done with the existing preamplifier and the procedure was repeated with this preamplifier without changing the setup. The setup for this test is identical to the setup given in Table 1. Table 8 contains the results of the test and it shows that there is a slight improvement in SNR.

Table 8. Preamplifier comparison test.

	CCNI Preamplifier	Preamplifier
Signal	5.07×10^5	5.41×10^5
Noise	4.48×10^3	4.05×10^3
SNR	113.17	133.6

The following are the codes used to compute the stabilizing network and matching network parameters.

A.6 *Stabilizing Network Code*

```
% Sonam Tobgay
% ECE, WPI
% Spring 2004


global Z0;
global ZL;

set_Z0(50);                 % setting characteristic impedance

close all;              % close all opened graphs
%clear all;               % clear all variables


S11=0.358952-0.80815j;
S21=-12.27574+11.97952j;
S12=0.01412+0.02232j;
S22=0.42092-0.286580j;



delta=S11*S22-S12*S21;

% radius and center of output stability circle
r_out_numer=abs(S12*S21);
r_out_denom=abs(abs(S22)^2-abs(delta)^2);
r_out=r_out_numer/r_out_denom;

c_out_numer=conj(S22-(conj(S11)*delta));
c_out_denom=abs(S22)^2-abs(delta)^2;
c_out=c_out_numer/c_out_denom;

ang=0:0.01:2.5*pi;

 % plotting point on smith chart
 color_smith

% plotting output stability circle

hold on;
plot(real(c_out)+r_out.*cos(ang),
imag(c_out)+r_out.*sin(ang),'linewidth',2, 'color', 'black');


dist_points=sqrt(real(c_out)^2+imag(c_out)^2);  % distance between
points
r_new=dist_points - r_out;                      % radius of new
circle

% plotting new circle
hold on;
plot(r_new*cos(ang), r_new*sin(ang),'linewidth',2, 'color', 'black');

% plotting line between circle centers
line([0 real(c_out)],[0 imag(c_out)], 'Color','black',
'Linewidth',2);


% pi attenuator network calculations
k=sqrt(1/r_new);
```

```
R1=Z0*((k+1)/(k-1));
R2=(Z0/2)*(k^2-1)/k;
```

```
global rf_Network; % define a global variable to store the network
description
```

A.7 Code to find Γ_S

```
% Sonam Tobgay
% ECE, WPI
% Spring 2004


global Z0;
global ZL;

set_Z0(50);                    % setting characteristic impedance

close all;            % close all opened graphs
%clear all;             % clear all variables

%feedback stabilization
% Fmin=10^(0.61936/10);
% Rn=4.054;
% Gamma_imn=0.96;
% Fk=10^(0.9/10);
% Gamma_opt=0.11028+0.05458j;
% Gamma_s1=0;
%
% S11=0.51128-0.19421j;
% S21=-6.54535+3.20775j;
% S12=0.06022-0.00492j;
% S22=0.21512-0.24143j;


% %for no feedback stabilization
% Fmin=10^(0.256/10);
% Rn=2.271;
% Gamma_imn=0.96;
% Fk=10^(0.9/10);
% Gamma_opt=0.36787+0.31053j;
% Gamma_s1=0;
%
% S11=0.06409-0.81596j;
% S21=-3.199959+4.55845j;
% S12=0.00399+0.00522j;
% S22=-0.48708-0.02187j;

%for stabilization using op amp
Fmin=10^(0.232/10);
Rn=2.2320;
Gamma_imn=0.96;
Fk=10^(0.9/10);
Gamma_opt=0.48866+0.27767j;
Gamma_s1=0;

S11=0.35850-0.80810j;
S21=-5.99837+5.86394j;
S12=0.00691+0.01091j;
S22=0.10143-0.06897j;

delta=S11*S22-S12*S21;

Fnumer1=4*Rn*abs(Gamma_s1-Gamma_opt)^2;
Fdenom1=Z0*(1-abs(Gamma_s1)^2)*(abs(1+Gamma_opt)^2);
F1=Fmin+Fnumer1/Fdenom1;

nf_min=9999;
```

```matlab
ang=0:0.1:2*pi;
% plotting point on smith chart
color_smith

% plotting NF
qk_first=abs(1+Gamma_opt)^2;
qk_second=(Fk-Fmin)/(4*Rn/Z0);
qk=qk_first*qk_second;
c_nf=Gamma_opt/(1+qk);   %center noise figure
r_nf_numer=(1-(abs(Gamma_opt)^2))*qk+(qk^2); %radius noise figure
r_nf=sqrt(r_nf_numer)/(1+qk);

% hold on;
% plot(real(c_nf)+r_nf.*cos(ang),
imag(c_nf)+r_nf.*sin(ang),'linewidth',2, 'color', 'black');


%plotting VSWR circle - source side

% for Gamma_l_mag=0:0.1:1;
%     for Gamma_l_ang=0:0.1:2*pi;
%         Gamma_l=Gamma_l_mag*cos(Gamma_l_ang) +
Gamma_l_mag*sin(Gamma_l_ang)*j;
%
%
%             fprintf('%f,%f\n',real(Gamma_in),imag(Gamma_in));
%             Gamma_in=(S11-delta*Gamma_l)/(1-S22*Gamma_l);
%             c_vswr_source_numer=(1-
abs(Gamma_imn)^2)*conj(Gamma_in);
%             c_vswr_source_denom=1-abs(Gamma_imn*Gamma_in)^2;
%             c_vswr_source=c_vswr_source_numer/c_vswr_source_denom;
%             r_vswr_source_numer=(1-abs(Gamma_in)^2)*abs(Gamma_imn);
%             r_vswr_source_denom=1-abs(Gamma_imn*Gamma_in)^2;
%             r_vswr_source=r_vswr_source_numer/r_vswr_source_denom;
%
%             hold on;
%             plot(real(c_vswr_source)+r_vswr_source.*cos(ang),
imag(c_vswr_source)+r_vswr_source.*sin(ang),'linewidth',2, 'color',
'red');
%
%             end
%             end

FileName=strcat('D:MatlabData\PreampData.txt');
FID=fopen (FileName,'w');
fprintf(FID,'\tGamma_l\t\t  Gamma_s\t      \tNF         Gain\t  NM\n');

FileName2=strcat('D:MatlabData\MinNF.txt');
FID2=fopen (FileName2,'w');
fprintf(FID2,'\tmn\t\t  Gamma_l\t\t  Gamma_s\t      NF         Gain\t
NM\n');

FileName3=strcat('D:MatlabData\Gain.txt');
FID3=fopen (FileName3,'w');
fprintf(FID3,'\tmn\t\t  Gamma_l\t\t  Gamma_s\t      NF         Gain\t
NM\n');

% Gamma_l_mag=0:0.05:0.95;
% Gamma_l_ang=0:0.1:2*pi;
% Gamma_s_ang=0:0.1:2*pi;
Gamma_l_mag=0.95;
Gamma_l_ang=0:0.1:2*pi;
Gamma_s_ang=0:0.1:2*pi;
for m=1:length(Gamma_l_mag)
    for n=1:length(Gamma_l_ang)

        Gamma_l(m,n)=Gamma_l_mag(m)*exp(1j*Gamma_l_ang(n));
        z_l(m,n)=(1+Gamma_l(m,n))/(1-Gamma_l(m,n));
```

106

```
        Gamma_in=(S11-delta*Gamma_l(m,n))/(1-S22*Gamma_l(m,n));
        c_vswr_source_numer=(1-abs(Gamma_imn)^2)*conj(Gamma_in);
        c_vswr_source_denom=1-abs(Gamma_imn*Gamma_in)^2;
        c_vswr_source=c_vswr_source_numer/c_vswr_source_denom;
        r_vswr_source_numer=(1-abs(Gamma_in)^2)*abs(Gamma_imn);
        r_vswr_source_denom=1-abs(Gamma_imn*Gamma_in)^2;
        r_vswr_source=r_vswr_source_numer/r_vswr_source_denom;


        %Gamma_s_ang=0:0.1:2*pi;

Gamma_s(m,n)=c_vswr_source+r_vswr_source*exp(1j*Gamma_s_ang(n));

        z_s(m,n)=(1+Gamma_s(m,n))/(1-Gamma_s(m,n));



        hold on;
        plot(Gamma_s(m,n), 'blacko');




        Fnumer=4*Rn*abs(Gamma_s(m,n)-Gamma_opt).^2;
        Fdenom=Z0*(1-abs(Gamma_s(m,n)).^2)*(abs(1+Gamma_opt)^2);
        nf(m,n)=Fmin+Fnumer/Fdenom;



        gt_numer=(1-abs(Gamma_l(m,n))^2)*(abs(S21)^2)*(1-
abs(Gamma_s(m,n)).^2);
        gt_denom=(abs(1-(Gamma_s(m,n)*Gamma_in)).^2)*(abs(1-
(S22*Gamma_l(m,n)))^2);
        gt(m,n)=gt_numer/gt_denom;



        nm(m,n)=(nf(m,n)-1)/(1-1/gt(m,n));
        %nm=(nf-1)/(1-1/gt);
        %end



        if (nf(m,n)<nf_min)
            nf_min=nf(m,n);
            m_min=m;
            n_min=n;
            fprintf(FID2, '  %g,%g\t',m_min,n_min);
            %fprintf(FID2, '
%f,%f\t',real(Gamma_l(m,n)),imag(Gamma_l(m,n)));
            fprintf(FID2, '  %f,%f\t',real(z_l(m,n)),imag(z_l(m,n)));
            %fprintf(FID2, '
%f,%f\t',real(Gamma_s(m,n)),imag(Gamma_s(m,n)));
            fprintf(FID2, '  %f,%f\t',real(z_s(m,n)),imag(z_s(m,n)));

            fprintf(FID2, '  %f\t',nf(m,n));
            fprintf(FID2, '  %f\t',gt(m,n));
            fprintf(FID2, '  %f\n',nm(m,n));
        end


        if ((gt(m,n)>=2) && (nf(m,n)<=1.2))
            fprintf(FID3, '  %g,%g\t',m_min,n_min);
            %fprintf(FID2, '
%f,%f\t',real(Gamma_l(m,n)),imag(Gamma_l(m,n)));
            fprintf(FID2, '  %f,%f\t',real(z_l(m,n)),imag(z_l(m,n)));
            %fprintf(FID2, '
%f,%f\t',real(Gamma_s(m,n)),imag(Gamma_s(m,n)));
            fprintf(FID2, '  %f,%f\t',real(z_s(m,n)),imag(z_s(m,n)));
```

```matlab
                        fprintf(FID3, '  %f\t',nf(m,n));
                        fprintf(FID3, '  %f\t',gt(m,n));
                        fprintf(FID3, '  %f\n',nm(m,n));
                end



                %Write data to file

                %fprintf(FID2, '
%f,%f\t',real(Gamma_l(m,n)),imag(Gamma_l(m,n)));
                fprintf(FID2, '  %f,%f\t',real(z_l(m,n)),imag(z_l(m,n)));
                %fprintf(FID2, '
%f,%f\t',real(Gamma_s(m,n)),imag(Gamma_s(m,n)));
                fprintf(FID2, '  %f,%f\t',real(z_s(m,n)),imag(z_s(m,n)));
                fprintf(FID, '  %f',nf(m,n));
                fprintf(FID, '  %f',gt(m,n));
                fprintf(FID, '  %f\n',nm(m,n));

                %hold on;
                %plot(real(c_vswr_source)+r_vswr_source.*cos(ang),
imag(c_vswr_source)+r_vswr_source.*sin(ang),'linewidth',2, 'color',
'red');

        end

end



fclose(FID3);
fclose (FID2);
fclose (FID);


FileName4=strcat('D:MatlabData\Descrete.txt');
FID4=fopen (FileName4,'w');
fprintf(FID4,'s\t\t  Gamma_l\t\t  Gamma_in\t      NF          Gain\t
NM\n');

for s=1:length(Gamma_l_mag)
    nf_min_des(s)=9999;
    for t=1:length(Gamma_l_ang)
        if (nf(s,t)<nf_min_des(s))
            nf_min_des(s)=nf(s,t);
            n_min_des(s)=t;
        end
    end
%     Gamma_s_des(s)=Gamma_s(s,n_min_des(s));
%     Gamma_l_des(s)=Gamma_l(s,n_min_des(s));
%     Gamma_l_ang_des(s)=Gamma_l_ang(n_min_des(s));


%     fprintf(FID4, '  %f\t',s);
%     fprintf(FID4, '
%f,%f\t',real(Gamma_l_des(s)),imag(Gamma_l_des(s)));
%     fprintf(FID4, '
%f,%f\t',real(Gamma_s_des(s)),imag(Gamma_s_des(s)));

    fprintf(FID4, '  %d\t',s);
    fprintf(FID4, '
%f,%f\t',real(z_l(s,n_min_des(s))),imag(z_l(s,n_min_des(s))));
    fprintf(FID4, '
%f,%f\t',real(z_s(s,n_min_des(s))),imag(z_s(s,n_min_des(s))));

    fprintf(FID4, '  %f\t',nf_min_des(s));
    fprintf(FID4, '  %f\t',gt(s,n_min_des(s)));
    fprintf(FID4, '  %f\n',nm(s,n_min_des(s)));
end
```

108

```
fclose(FID4);

global rf_Network; % define a global variable to store the network
description
```

B - Appendix

B.1 Inductance Calculation

A magnetic field in the form of magnetic flux is generated, if a current is passed through a wire. The magnetic flux and the current are related by the inductance. Inductance plays an important part in the design and analysis of surface coils. It is related to magnetic energy E_m by:

$$E_m = \iiint_V \mathbf{B} \cdot \mathbf{H} dV = \frac{1}{2}LI^2 \tag{79}$$

Here L is the inductance of the wire and I is the current in the wire. The magnetic flux density $\mathbf{B}$ and the magnetic field intensity $\mathbf{H}$ are produced by the electric current density $\mathbf{J}$, as given by following equations.

$$\begin{aligned} \mathbf{B} \cdot \mathbf{H} &= (\nabla \times \mathbf{A}) \cdot \mathbf{H} \\ &= \mathbf{A} \cdot (\nabla \times \mathbf{H}) + \nabla \cdot (\mathbf{A} \times \mathbf{H}) \\ &= \mathbf{A} \cdot \mathbf{J} + \nabla(\mathbf{A} \cdot \mathbf{H}) \end{aligned} \tag{80}$$

In the above equations, $\mathbf{A}$ denotes the magnetic vector potential generated by $\mathbf{J}$. $\mathbf{A}$ is related to $\mathbf{J}$ by the following expression:

$$\mathbf{A(r)} = \frac{\mu_0}{4\pi} \iiint_V \frac{\mathbf{J(r')}}{R} dV' \tag{81}$$

where: μ_0: permeability of free space and

110

$$R: \text{distance between the two points.}$$

Using the relation in equation (80), equation (79) becomes:

$$E_m = \frac{1}{2}\iiint_V \mathbf{A} \cdot \mathbf{J} dV + \frac{1}{2}\oiint_S (\mathbf{A} \times \mathbf{H}) dS \tag{82}$$

The field produced by $\mathbf{J}$ extends to infinity and S in equation (82) is a spherical surface whose radius extends to infinity. As a result the surface integral vanishes and equation (82) becomes:

$$E_m = \frac{1}{2}\iiint_V \mathbf{A} \cdot \mathbf{J} dV \tag{83}$$

Since self-inductance L, is related to E_m by:

$$E_m = \frac{1}{2}LI^2 \tag{84}$$

We obtain the expression for L, from equation (83) and (84):

$$L = \frac{1}{I^2}\iiint_V \mathbf{A} \cdot \mathbf{J} dV \tag{85}$$

Substituting equation (81) in equation (85):

$$L = \frac{\mu_0}{4\pi I^2}\iiint_V \iiint_{V'} \frac{\mathbf{J}(\mathbf{r}) \cdot \mathbf{J}(\mathbf{r}')}{R} dV' dV \tag{86}$$

where, $R = |\mathbf{r} - \mathbf{r}'|$.

The skin depth of a medium, δ_s, characterizes how well an electromagnetic wave can penetrate into a conducting medium [11].

$$\delta_s = \frac{1}{\alpha} \tag{87}$$

The attenuation constant α is zero, if the medium is a perfect dielectric. It is infinite if the medium is a perfect conductor. According to equation (87), δ_s can also be defined as:

$$\delta_s = \sqrt{\frac{2}{\omega\mu\sigma}} \tag{88}$$

In equation (88): ω: angular frequency,

μ: permeability of the medium, and

σ: conductivity of the medium.

According to equation (88), a copper wire coil of 12mm radius and 0.6mm wire radius the current mainly flows on the surface of the coil. Therefore, equation (86) becomes:

$$L = \frac{\mu_0}{4\pi I^2} \iint\limits_{S} \int\limits_{S'} \frac{\mathbf{J(r)} \cdot \mathbf{J(r')}}{R} dS' dS \tag{89}$$

Assumptions have been made to find the inductance of the coil. Equation (89) is therefore an approximation of the inductance. It is laborious to try to solve equation (89) analytically. A numerical approach was therefore used to solve the equation. In this approach a program was written in MATLAB. Assuming $I = 1A$, the coil was broken into discrete sections as shown in Figure 74 and Figure 75, and a summation of the electric current density $\mathbf{J}$ was made throughout the coil. A brief introductory explanation is given in the following sections.

In this method equation (89) becomes:

$$L = \frac{\mu_0}{4\pi I^2} \sum_{k} \sum_{k'} \frac{\mathbf{J(r_k)} \cdot \mathbf{J(r_{k'})}}{|\mathbf{r_k} - \mathbf{r_{k'}}|} \tag{90}$$

where $I = 1A$ and $\mathbf{J} = \frac{I}{2\pi R_W} \mathbf{a}$. Here R_W is the radius of the wire and $\mathbf{a}$ is a unit vector pointing in the direction of current flow.
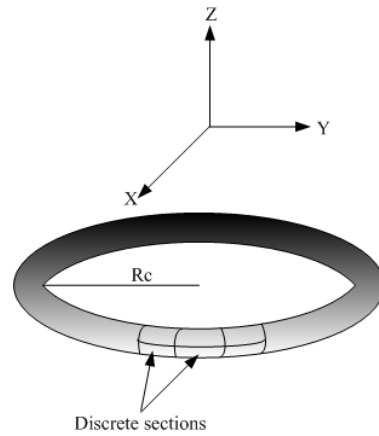
Figure 74. Coil divided into discrete sections.
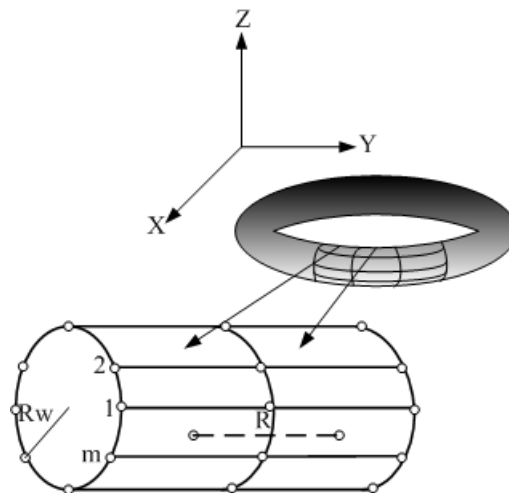
Figure 75. Cross sectional view of nodal points.

Dividing the coil into discrete sections enables one to find **J**, flowing through each section. In order to do that, one needs to know the number of sections that the coil is divided into and also the number of nodes that are produced as a result of dividing it into discrete sections. The algorithm to find the total number of nodes is described by the following equation

$$\begin{pmatrix} p(k,\mathbf{x}) \\ p(k,\mathbf{y}) \\ p(k,\mathbf{z}) \end{pmatrix} = \begin{pmatrix} \cos\dfrac{2\pi}{N}(n-1) & \sin\dfrac{2\pi}{N}(n-1) & 0 \\ -\sin\dfrac{2\pi}{N}(n-1) & \cos\dfrac{2\pi}{N}(n-1) & 0 \\ 0 & 0 & 1 \end{pmatrix} \begin{pmatrix} R_W + R_C \cos\dfrac{2\pi}{M}(m-1) \\ 0 \\ R_C \sin\dfrac{2\pi}{M}(m-1) \end{pmatrix} \qquad (91)$$

Here: N: total number of discrete sections,

                M: total number of nodes, and

                k: node increment.

$$\begin{aligned} n &= 1:N \\ m &= 1:M \\ k &= m+(n-1)M \end{aligned} \qquad (92)$$

Each section in the coil has four nodes and a single node may be shared by one or more sections. It is therefore important to come up with equations that describe the corners of a section that does not neglect or add a node. The following equations describe a section according to its nodes.

$$\begin{aligned} t(k,C_1) &= m+(n-1)M \\ t(k,C_2) &= m+1+(n-1)M \\ t(k,C_3) &= m+1+M+(n-1)M \end{aligned} \Bigg\} m < M$$

$$\begin{aligned} t(k,C_2) &= m+1+(n-1)M-M \\ t(k,C_3) &= m+1+(n-1)M \end{aligned} \Bigg\} m = M \qquad (93)$$

$$t(k,C_4) = m+M+(n-1)M$$

Here: C_1: corner 1,

                C_2: corner 2,

                C_3: corner 3, and

                C_4: corner 4.

The relations shown in equation (93) work under the condition $n \neq N$. Different relations are needed when $n = N$. In addition to the above calculations, one needs to calculate the current vector that lets one know the magnitude and direction of current flow. And one also needs to calculate the section center points, which enables one to

calculate the distance R. These procedures are given in the source code in Section B.3. The program in Section B.3 was executed with the following values:

$$R_C = 12\text{mm},$$

$$R_W = 0.6\text{mm},$$

$$M = 20, \text{ and}$$

$$N = 40.$$

The inductance calculated by the program: $L = 52.65nH$. As stated earlier this is not an exact value. It is only an approximation. The mesh generated by the program is given in Figure 76.
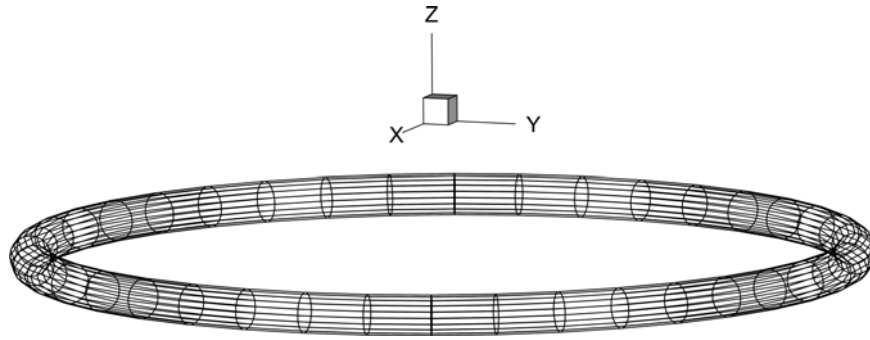
Figure 76. Plot of mesh generated by program.

B.2 *Magnetic Field Calculation*

The coil produces a magnetic field when a current is flowing through it. In addition to the current, the magnetic field produced by the coil varies according to the geometry and the relative position of the coil with respect to the point in consideration. It is desirable to analyze the magnetic field.

As stated in the previous section, the magnetic field **B**, is given by:

$$\mathbf{B(r)} = \nabla \times \mathbf{A(r)} \tag{94}$$

Substituting equation (81) into equation (94) gives:

$$\mathbf{B}(\mathbf{r}) = \frac{\mu_0}{4\pi} \nabla \times \iiint_{V'} \frac{\mathbf{J}(\mathbf{r}')}{|\mathbf{r} - \mathbf{r}'|} dV' \tag{95}$$

According to the vector identity:

$$\nabla \times (U\mathbf{A}) = U\nabla \times \mathbf{A} + \nabla U \times \mathbf{A} \tag{96}$$

Using equation (96) in equation (95) gives:

$$\mathbf{B}(\mathbf{r}) = \frac{\mu_0}{4\pi} \iiint_{V'} \left(\frac{1}{|\mathbf{r} - \mathbf{r}'|} \nabla \times \mathbf{J}(\mathbf{r}') + \nabla \frac{1}{|\mathbf{r} - \mathbf{r}'|} \times \mathbf{J}(\mathbf{r}') \right) dV' \tag{97}$$

In equation (97) $\nabla \times \mathbf{J}(\mathbf{r}')$ is equal to zero, since the ∇ operator in this situation differentiates with respect to $\mathbf{r}$ and not $\mathbf{r}'$. Therefore, equation (97) becomes:

$$\mathbf{B}(\mathbf{r}) = \frac{\mu_0}{4\pi} \iiint_{V'} \nabla \frac{1}{|\mathbf{r} - \mathbf{r}'|} \times \mathbf{J}(\mathbf{r}') dV' \tag{98}$$

Since $R = |\mathbf{r} - \mathbf{r}'|$ is the magnitude of the distance between the points, equation (98) becomes:

$$\mathbf{B}(\mathbf{r}) = \frac{\mu_0}{4\pi} \iiint_{V'} \nabla \frac{1}{\sqrt{(x-x')^2 + (y-y')^2 + (z-z')^2}} \times \mathbf{J}(\mathbf{r}') dV' \tag{99}$$

Expanding using the ∇ operator, equation (99) becomes:

$$\mathbf{B}(\mathbf{r}) = \frac{\mu_0}{4\pi} \iiint_{V'} \mathbf{J}(\mathbf{r}') \times \begin{pmatrix} \dfrac{x-x'}{\left(\sqrt{(x-x')^2 + (y-y')^2 + (z-z')^2}\right)^3} \\ \dfrac{y-y'}{\left(\sqrt{(x-x')^2 + (y-y')^2 + (z-z')^2}\right)^3} \\ \dfrac{z-z'}{\left(\sqrt{(x-x')^2 + (y-y')^2 + (z-z')^2}\right)^3} \end{pmatrix} dV' \tag{100}$$

As in the case of the inductance calculation, it is laborious to solve equation (100). The program written to calculate the inductance was modified and used to calculate the magnetic field. The modified code for the magnetic field calculation is also given

116

in Section B.4. The magnetic field calculated by the program is, $\mathbf{B} = 5.15 \times 10^{-5}\,T$.

The data generated is plotted in Figure 77.
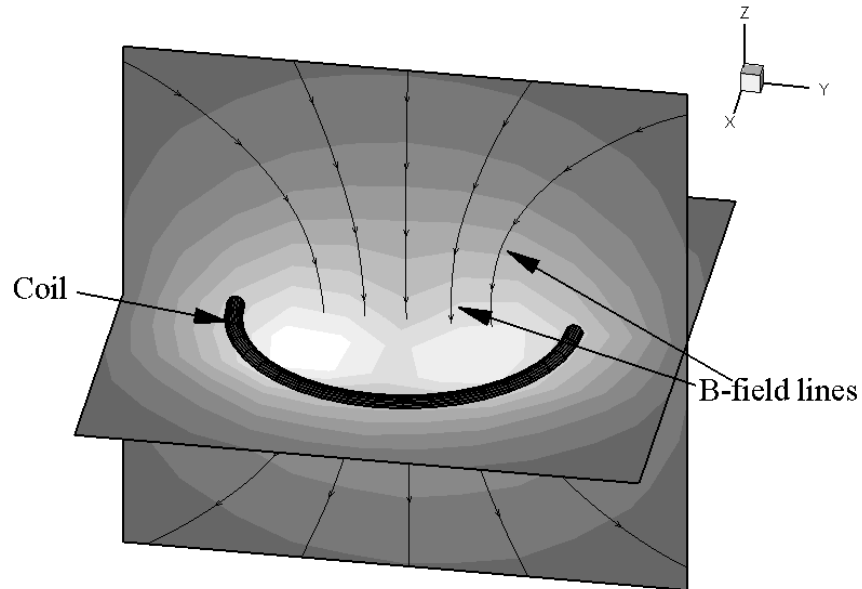
Figure 77. Magnetic field distribution of surface coil.

The following are the codes used to compute the inductance and the magnetic field.

B.3 Inductance Calculation Code

```
% Sonam Tobgay
% ECE, WPI
% Fall 2003

% this code calculates the coil inductance

% calculating the points on a circle

% P(m,x) = point on cylinder section
% m is the node, x is the direction or vector
% k = increment for point on the cylinder section
% M = total number of points in a cylinder section
% R = radius of the cylinder
% N = total number of cylinder sections
% t = point for a patch
% A = Area
% r = center point
% RR = radius of coil

clear all;

RR=0.012;
R=0.0006;
M=20;
N=40;
P=zeros(M*N,3);
t=zeros(M*N,4);
V=zeros(M*N,3);
A=zeros(M*N,1);
J=zeros(M*N,3);
JP=zeros(M*N,3);
r=zeros(M*N,3);
u=4*pi*1e-7; % permeability of free space

% procedure for all the nodes in the cylinder
for n=1:N
    for m=1:M
        k=m+(n-1)*M;
        P(k,1)=cos(2*pi*(n-1)/N)*(RR+R*cos(2*pi*(m-1)/M)); %P(k,1): 1
represents the x-direction
        P(k,2)=-sin(2*pi*(n-1)/N)*(RR+R*cos(2*pi*(m-1)/M));
%P(k,2): 2 represents the y-direction
        P(k,3)=R*sin(2*pi*(m-1)/M);                    %P(k,3): 3
represents the z-direction
    end
end


% procedure for calculating the number of sections from n to N-1
k=0;
for n=1:N-1
    for m=1:M
        k=k+1;
        t(k,1)=m+(n-1)*M;
        if(m<M)
            t(k,2)=m+1+(n-1)*M;
            t(k,3)=m+1+M+(n-1)*M;
        end
```

```
            if(m==M)
                t(k,2)=m+1+(n-1)*M-M;
                %t(k,3)=m+1+M+(n-1)*M-M;
                t(k,3)=m+1+(n-1)*M;
            end
            t(k,4)=m+M+(n-1)*M;

            % calculating the current vectors
            V(k,1)=0.5*P(t(k,3),1)+0.5*P(t(k,4),1)-0.5*P(t(k,1),1)-
0.5*P(t(k,2),1);
            V(k,2)=0.5*P(t(k,3),2)+0.5*P(t(k,4),2)-0.5*P(t(k,1),2)-
0.5*P(t(k,2),2);
            V(k,3)=0.5*P(t(k,3),3)+0.5*P(t(k,4),3)-0.5*P(t(k,1),3)-
0.5*P(t(k,2),3);

            % calculating area
            A(k)=norm(V(k,:))*2*pi*R/M;

            % calculating the norm
            tempV=norm(V(k,:));              % temporary buffer
            V(k,1)=V(k,1)/tempV;
            V(k,2)=V(k,2)/tempV;
            V(k,3)=V(k,3)/tempV;

            % current J
            J(k,1)=V(k,1)/(2*pi*R);
            J(k,2)=V(k,2)/(2*pi*R);
            J(k,3)=V(k,3)/(2*pi*R);

            % center points

r(k,1)=0.25*(P(t(k,1),1)+P(t(k,2),1)+P(t(k,3),1)+P(t(k,4),1));

r(k,2)=0.25*(P(t(k,1),2)+P(t(k,2),2)+P(t(k,3),2)+P(t(k,4),2));

r(k,3)=0.25*(P(t(k,3),1)+P(t(k,2),3)+P(t(k,3),3)+P(t(k,4),3));

    end
end

% procedure for calculating the section when n=N
for n=N
    for m=1:M
        k=k+1;
        t(k,1)=m+(n-1)*M;
        if(m<M)
            t(k,2)=m+1+(n-1)*M;
            t(k,3)=m+1;
        end
        if(m==M)
            t(k,2)=m+1+(n-1)*M-M;
            t(k,3)=m+1-M;
        end
        t(k,4)=m;

        % calculating the current vectors
        V(k,1)=0.5*P(t(k,3),1)+0.5*P(t(k,4),1)-0.5*P(t(k,1),1)-
0.5*P(t(k,2),1);
        V(k,2)=0.5*P(t(k,3),2)+0.5*P(t(k,4),2)-0.5*P(t(k,1),2)-
0.5*P(t(k,2),2);
        V(k,3)=0.5*P(t(k,3),3)+0.5*P(t(k,4),3)-0.5*P(t(k,1),3)-
0.5*P(t(k,2),3);

        % calculating area
        A(k)=norm(V(k,:))*2*pi*R/M;

        % calculating the norm
        tempV=norm(V(k,:));              % temporary buffer
        V(k,1)=V(k,1)/tempV;
        V(k,2)=V(k,2)/tempV;
        V(k,3)=V(k,3)/tempV;
```

```matlab
        % current J
        J(k,1)=V(k,1)/(2*pi*R);
        J(k,2)=V(k,2)/(2*pi*R);
        J(k,3)=V(k,3)/(2*pi*R);

        % center nodes

r(k,1)=0.25*(P(t(k,1),1)+P(t(k,2),1)+P(t(k,3),1)+P(t(k,4),1));

r(k,2)=0.25*(P(t(k,1),2)+P(t(k,2),2)+P(t(k,3),2)+P(t(k,4),2));

r(k,3)=0.25*(P(t(k,1),3)+P(t(k,2),3)+P(t(k,3),3)+P(t(k,4),3));

    end
end

% current at the nodes
for k=1:N*M
    JP(t(k,1),:)=JP(t(k,1),:)+J(k,:);
    JP(t(k,2),:)=JP(t(k,2),:)+J(k,:);
    JP(t(k,3),:)=JP(t(k,3),:)+J(k,:);
    JP(t(k,4),:)=JP(t(k,4),:)+J(k,:);
end
JP=JP/4;

% procedure to save data
  FileName=strcat('coilmesh.data');
  FID=fopen (FileName,'w');
  fprintf(FID, ' %s\n','TITLE = "MESH"');
  fprintf(FID, ' %s\n','VARIABLES="X", "Y", "Z", "Jpx", "Jpy",
"Jpz"');
  fprintf(FID, ' %s','ZONE T="Current"   I=');
  fprintf(FID, ' %5.0f',N*M);
  fprintf(FID, ' %s\n','F=FEPOINT,  ET=QUADRILATERAL');

   for nn=1:N*M
       fprintf(FID, ' %f',P(nn,1));
       fprintf(FID, ' %f',P(nn,2));
       fprintf(FID, ' %f',P(nn,3));
       fprintf(FID, ' %f',JP(nn,1));
       fprintf(FID, ' %f',JP(nn,2));
       fprintf(FID, ' %f\n',JP(nn,3));
   end

   for kk=1:N*M
       fprintf(FID, ' %4.0f',t(kk,1));
       fprintf(FID, ' %4.0f',t(kk,2));
       fprintf(FID, ' %4.0f',t(kk,3));
       fprintf(FID, ' %4.0f\n',t(kk,4));
   end
   fclose (FID);


L=0;
for m=1:M*N
    disp(strcat('Node ',sprintf('    %g',m)))
    for n=1:M*N
        if(m~=n)
            L=L+dot(J(m,:),J(n,:))/norm(r(m,:)-r(n,:))*A(m)*A(n);
        end
    end
end
L=L*u/(4*pi);
```

B.4 Magnetic Field Calculation Code

```
% Sonam Tobgay
% ECE, WPI
% Fall 2003

% this code calculates the magnetic field produced by the coil

% calculating the points on a circle

% P(m,x) = point on cylinder section
% m is the node, x is the direction or vector
% k = increment for point on the cylinder section
% M = total number of points in a cylinder section
% R = radius of the cylinder
% N = total number of cylinder sections
% t = point for a patch
% A = Area
% r = center point
% RR = radius of coil

clear all;

RR=0.012;
R=0.0006;
M=20;
N=20;
P=zeros(M*N,3);
t=zeros(M*N,4);
V=zeros(M*N,3);
A=zeros(M*N,1);
J=zeros(M*N,3);
JP=zeros(M*N,3);
r=zeros(M*N,3);
u=4*pi*1e-7; % permeability of free space

% procedure for all the nodes in the cylinder
for n=1:N
    for m=1:M
        k=m+(n-1)*M;
        P(k,1)=cos(2*pi*(n-1)/N)*(RR+R*cos(2*pi*(m-1)/M));
%P(k,1): 1 represents the x-direction
        P(k,2)=-sin(2*pi*(n-1)/N)*(RR+R*cos(2*pi*(m-1)/M));
%P(k,2): 2 represents the y-direction
        P(k,3)=R*sin(2*pi*(m-1)/M);
%P(k,3): 3 represents the z-direction
    end
end


% procedure for calculating the number of sections from n to N-1
k=0;
for n=1:N-1
    for m=1:M
        k=k+1;
        t(k,1)=m+(n-1)*M;
        if(m<M)
            t(k,2)=m+1+(n-1)*M;
            t(k,3)=m+1+M+(n-1)*M;
        end
        if(m==M)
            t(k,2)=m+1+(n-1)*M-M;
            t(k,3)=m+1+(n-1)*M;
        end
        t(k,4)=m+M+(n-1)*M;

        % calculating the current vectors
```

```
        V(k,1)=0.5*P(t(k,3),1)+0.5*P(t(k,4),1)-0.5*P(t(k,1),1)-
0.5*P(t(k,2),1);
        V(k,2)=0.5*P(t(k,3),2)+0.5*P(t(k,4),2)-0.5*P(t(k,1),2)-
0.5*P(t(k,2),2);
        V(k,3)=0.5*P(t(k,3),3)+0.5*P(t(k,4),3)-0.5*P(t(k,1),3)-
0.5*P(t(k,2),3);

        % calculating area
        A(k)=norm(V(k,:))*2*pi*R/M;

        % calculating the norm
        tempV=norm(V(k,:));              % temporary buffer
        V(k,1)=V(k,1)/tempV;
        V(k,2)=V(k,2)/tempV;
        V(k,3)=V(k,3)/tempV;

        % current J
        J(k,1)=V(k,1)/(2*pi*R);
        J(k,2)=V(k,2)/(2*pi*R);
        J(k,3)=V(k,3)/(2*pi*R);

        % center points

r(k,1)=0.25*(P(t(k,1),1)+P(t(k,2),1)+P(t(k,3),1)+P(t(k,4),1));

r(k,2)=0.25*(P(t(k,1),2)+P(t(k,2),2)+P(t(k,3),2)+P(t(k,4),2));

r(k,3)=0.25*(P(t(k,3),1)+P(t(k,2),3)+P(t(k,3),3)+P(t(k,4),3));

    end
end

% procedure for calculating the section when n=N
for n=N
    for m=1:M
        k=k+1;
        t(k,1)=m+(n-1)*M;
        if(m<M)
            t(k,2)=m+1+(n-1)*M;
            t(k,3)=m+1;
        end
        if(m==M)
            t(k,2)=m+1+(n-1)*M-M;
            t(k,3)=m+1-M;
        end
        t(k,4)=m;

        % calculating the current vectors
        V(k,1)=0.5*P(t(k,3),1)+0.5*P(t(k,4),1)-0.5*P(t(k,1),1)-
0.5*P(t(k,2),1);
        V(k,2)=0.5*P(t(k,3),2)+0.5*P(t(k,4),2)-0.5*P(t(k,1),2)-
0.5*P(t(k,2),2);
        V(k,3)=0.5*P(t(k,3),3)+0.5*P(t(k,4),3)-0.5*P(t(k,1),3)-
0.5*P(t(k,2),3);

        % calculating area
        A(k)=norm(V(k,:))*2*pi*R/M;

        % calculating the norm
        tempV=norm(V(k,:));              % temporary buffer
        V(k,1)=V(k,1)/tempV;
        V(k,2)=V(k,2)/tempV;
        V(k,3)=V(k,3)/tempV;

        % current J
        J(k,1)=V(k,1)/(2*pi*R);
        J(k,2)=V(k,2)/(2*pi*R);
        J(k,3)=V(k,3)/(2*pi*R);

        % center nodes
```

```
r(k,1)=0.25*(P(t(k,1),1)+P(t(k,2),1)+P(t(k,3),1)+P(t(k,4),1));

r(k,2)=0.25*(P(t(k,1),2)+P(t(k,2),2)+P(t(k,3),2)+P(t(k,4),2));

r(k,3)=0.25*(P(t(k,1),3)+P(t(k,2),3)+P(t(k,3),3)+P(t(k,4),3));

    end
end

% current at the nodes
for k=1:N*M
    JP(t(k,1),:)=JP(t(k,1),:)+J(k,:);
    JP(t(k,2),:)=JP(t(k,2),:)+J(k,:);
    JP(t(k,3),:)=JP(t(k,3),:)+J(k,:);
    JP(t(k,4),:)=JP(t(k,4),:)+J(k,:);
end
JP=JP/4;


% boundaries for plotting B in a 3-D space
xmin=-0.02; ymin=-0.02; zmin=-0.02;
xmax=0.02; ymax=0.02; zmax=0.02;
pk=0; % position counter
N1=7;
B=zeros(N1^3,3);

for xc=1:N1              % xc = counter for vector x
    xc
    for yc=1:N1          % yc = counter for vector y
        for zc=1:N1      % zc = counter for vector z
            x(xc)=xmin+(xmax-xmin)*(xc-1)/(N1-1);
            y(yc)=ymin+(ymax-ymin)*(yc-1)/(N1-1);
            z(zc)=zmin+(zmax-zmin)*(zc-1)/(N1-1);

            pk=pk+1;
            B(pk)=0;
            for bn=1:M*N
                rm=[x(xc)-r(bn,1), y(yc)-r(bn,2), z(zc)-r(bn,3)];
                jm=[J(bn,1),J(bn,2),J(bn,3)];
                B(pk,:)=B(pk,:)+cross(jm,rm)*A(bn)/norm(rm)^3
            end
        end
    end
end
B=u/(4*pi)*B;

% procedure to save data
FileName=strcat('magfield.data');
FID=fopen (FileName,'w');
fprintf(FID, ' %s\n','TITLE = "MAGNETICFIELD"');
fprintf(FID, ' %s\n','VARIABLES="X", "Y", "Z", "AbsB", "Bx", "By",
"Bz"');
fprintf(FID, ' %s','ZONE T="MagField"   I=');
fprintf(FID, ' %5.0f',N1^3);
fprintf(FID, ' %s\n','F=POINT');

pk=0;
```

```matlab
for xc=1:N1               % xc = counter for vector x
    for yc=1:N1           % yc = counter for vector y
        for zc=1:N1       % zc = counter for vector z
            pk=pk+1;
            fprintf(FID, '  %f',x(xc));
            fprintf(FID, '  %f',y(yc));
            fprintf(FID, '  %f',z(zc));
            fprintf(FID, '  %g',norm(B(pk,:)));
            fprintf(FID, '  %g',B(pk,1));
            fprintf(FID, '  %g',B(pk,2));
            fprintf(FID, '  %g\n',B(pk,3));
        end
    end
end
```

C - Appendix

Surface Coil Components Parts List.

Reference	Component	Manufacturer	Part No.	Description	Digikey No.
C1, C2, C4	Capacitor	Sprague-Goodman	SG2009	VARIABLE CAP, 1.4pF-3pF	SG2000CT-ND
C1, C2, C4	Capacitor	Sprague-Goodman	SG2009	VARIABLE CAP, 3.0pF-10pF	SG2002CT-ND
C1, C2, C4	Capacitor	Sprague-Goodman	SG2009	VARIABLE CAP, 4.5pF-20pF	SG2003CT-ND
C3 (200 MHz)	Capacitor	Voltronics (Used in place of the ATC-B capacitors.)	11-240-F-500	CAP FIXED, 24pF	
L1, L2 (200 MHz)	Inductor	JW Miller	PM1008	0.10uH +/- 10% Inductor	M1188CT-ND
L3 (200 MHz)	Inductor	JW Miller	PM1008	18nH +/- 20% Inductor	M1179CT-ND
L1, L2 (500 MHz)	Inductor	JW Miller	PM1008	39nH +/- 20% Inductor	M1183CT-ND
L3 (500 MHz)	Inductor	JW Miller	PM0805	6.8nH +/- 20% Inductor	M1152CT-ND
C3 (500 MHz)	Capacitor	Voltronics (Used in place of ATC-B capacitors)	11-8R2-B-500	CAP FIXED, 8.2pF	
D1	Pin-Diode	Temex	DH80050-40	PIN-Diode, 500V, 0.7Ohm R-ON	

Preamplifier Components Parts List.

Reference	Component	Manufacturer	Part No.	Description	Digikey No.
V1	Voltage Regulator	National Semiconductor	LM340A-T0263	5V-Ouptput	LM340S-5.0-ND
BJT	Transistor Matched	Discrete Semiconductor	DMMT3906W-7	PNP Mathced, -40V, -200mA	DMMT3906WDICT-ND
J1, J2, J3, J4	SMA	Johnson Components	142-0701-501	SMA Connector	J569-ND
Enclosure	Enclosure	Hammond Manufacturing	1590H	Box	HM365-ND
R7	Resistor	Yageo America	9C12063A10R0FKHFT	10	311-10.0FCT-ND
R3	Resistor	Yageo America	9C12063A33R0FKHFT	33	311-33.0RCT-ND
R5	Resistor	Yageo America	9C12063A47R0FKHFT	47	311-47.0FCT-ND
R4	Resistor	Yageo America	9C12063A5900FKHFT	590	311-590FCT-ND
R6	Resistor	Yageo America	9C12063A1001FKHFT	1K	311-1.00KFCT-ND
R1	Resistor	Yageo America	9C12063A2001FKHFT	2K	311-2.00KFCT-ND
R2	Resistor	Yageo America	9C12063A2321FKHFT	2.32K	311-2.32KFCT-ND
C9	Capacitor	Kemet	C1206C189C5GACTU	1.8pF	399-1180-1-ND
C2, C2A, C5,C5A, C10, C11	Capacitor	Kemet	C1206C271K5GACTU	270pF	399-1209-1-ND
C8	Capacitor	Yageo America	1206CG102J9B200	1000pF	311-1163-1-ND
C3, C3A, C6, C6A C14, C16	Capacitor	Panasonic-ECG	ECJ-3FC1H103J	10000pF	PCC2167CT-ND
C15, C17	Capacitor	AVX Corporation	12065C104KAT2A	0.1uF	478-1556-1-ND
C7	Capacitor	Panasonic-ECG	ECJ-3YB1E105K	1.0uF	PCC1893CT-ND
CM1	Capacitor (500 MHz)	Yageo America	1206CG220J9B200	22pF	311-1154-1-ND
CM2	Capacitor (500 MHz)	Kemet	1206CG689D9B200	6.8pF	311-1220-1-ND
CM1	Capacitor (200 MHz)	Yageo America	1206CG470J9B200M	47pF	311-1158-1-ND
CM2	Capacitor (200 MHz)	Yageo America	C1206C150J5GACTU	15pF	399-1194-1-ND
LM1	Inductor 500 MHz	API Delevan	1008-150K	0.015uH	DN08150CT-ND

LM2	Inductor 500 MHz	API Delevan	1008-470K	0.047uH	DN08470CT-ND
LM1	Inductor 200 MHz	API Delevan	1008-560K	0.056nH	DN08560CT-ND
LM2	Inductor 200 MHz	API Delevan	1008-820K	0.082uH	DN08820CT-ND
DC_FEED_1, DC_FEED_2, DC_FEED_3	RF Choke 500 MHz	API Delevan	1008-391K	0.39uH	DN08391CT-ND
D1, D2	Diode	Fairchild Semiconductor	BAV99		BAV99FSCT-ND